Transport Theory and Inelastic Nuclear Scattering for Proton Radiotherapy

by

Ryan Michael Brosch

A Dissertation Presented in Partial Fulfillment
of the Requirements for the Degree
Doctor of Philosophy

Approved July 2022 by the
Graduate Supervisory Committee:

Peter Rez, Co-Chair
Ricardo Alarcón, Co-Chair
Michael Treacy
Tanmay Vachaspati

ARIZONA STATE UNIVERSITY

August 2022

ABSTRACT

Proton radiotherapy has recently become a popular form of cancer treatment. For maximum effectiveness, accurate models are needed to calculate proton angular scattering and energy loss. Scattering events are statistically independent and may be calculated from the effective number of events per reciprocal multiple scattering angle or energy loss. It is shown that multiple scattering distributions from Molière's scattering law can be convolved by depth for accurate numerical calculation of angular distributions in several example materials. This obviates the need for correction factors to the analytic solution and its approximations. It is also shown that numerically solving Molière's scattering law in terms of the complete (non-small angle) differential cross section and large angle approximations extends the validity of Molière theory to large angles. To calculate probability energy loss distributions, Landau-Vavilov theory is adapted to Fourier transforms and extended to very thick targets through convolution over the probability energy loss distributions in each depth interval. When the depth is expressed in terms of the continuous slowing down approximation (CSDA) the resulting probability energy loss distributions rely on the mean excitation energy as the sole material dependent parameter. Through numerical calculation of the CSDA over the desired energy loss, this allows the energy loss cross section to vary across the distribution and accurately accounts for broadening and skewness for thick targets in a compact manner. An analytic, Fourier transform solution to Vavilov's integral is shown. A single scattering nuclear model that calculates large angle dose distributions that have a similar functional form to FLUKA (FLUktuierende KAskade) Monte Carlo, is also introduced. For incorporation into Monte Carlo or a treatment planning system, lookup tables of the

number of scattering events or cross sections for different clinical energies may be used to determine angular or energy loss distributions.

DEDICATION

To Jane

ACKNOWLEDGMENTS

My sincerest thanks go to my committee co-chairs Professors Peter Rez and Ricardo Alarcón and my committee members Michael Treacy and Tanmay Vachaspati. At Mayo Clinic my thanks go to Martin Bues, Wei Liu, Jiajian Shen and Xiaoning Ding.

TABLE OF CONTENTS

Page

CHAPTER

Page

CHAPTER

LIST OF FIGURES

Figure Page

Figure Page

CHAPTER 1

INTRODUCTION

Radiation Therapy Modalities

In radiation therapy, the goal is to deposit energy to a tumor site while avoiding healthy tissue. To do this, the dose (energy deposited per unit mass), must conform to the shape of the tumor and avoid dose to surrounding areas. This is called "conformal" dose[1]. Various types of radiation have been used for this purpose, among them photons, electrons and protons.

Photons have been used for cancer treatment since shortly after the discovery of x-rays by Roentgen in 1895. [2] Just two months after their discovery, x-rays were applied to treat several types of disease, most successfully against cutaneous epithelioma. The invention of the electron tube in 1914 overcame the early limitations of x-ray tubes, the anodes of which were prone to melting under high currents.[3] Further advancements came in 1928 with the invention of the linear accelerator[4]. In a "linac", electrons are accelerated down a waveguide by an electric field before optionally striking a tungsten target to produce photons. The resulting electrons or photons are then collimated with high density materials to a narrow beam for therapeutic purposes. In 1959 the multi-leaf collimator was invented, allowing irregular beam shapes to better conform radiation to a tumor site.[5]

In photon therapy, x-rays interact with the patient's cells primarily through Compton scattering as described by the Klein Nishina cross section[6, 7]. An incoming photon produces secondary electrons in a generally forward direction as can be seen from Figure 1.1. A secondary photon with reduced momentum then proceeds through the

patient and the secondary electron generates an ionizing path deeper into the patient.[8] This is the source of the skin-sparing build-up peak visible in Figure 1.2. It is a principal benefit of photon therapy. The forward peaked scattering results in sharp lateral cutoffs (Figure 1.2.) that allow excellent conforming of the beam to tumor sites to avoid critical organs. Equation (1.1 to 1.2) is the Klein Nishina cross section where E_y is the incident photon energy, $m_e c^2$ is the electron rest mass, θ is the scattering angle and r_e is the classical electron radius.

$$\frac{d\sigma}{d\Omega} = \frac{1}{2} r_e^2 P\left(E_\gamma, \theta\right)^2 \left(P\left(E_\gamma, \theta\right) + \frac{1}{P\left(E_\gamma, \theta\right)} - 1 + \cos^2\theta \right) \quad 1.1$$

$$P\left(E_y, \theta\right) = \frac{1}{\left(1 + \left(\frac{E_\gamma}{m_e c^2}\right)(1 - cos\theta)\right)} \quad 1.2$$

It can be seen in Figure 1.1 that higher energies deliver a more forward peaked lateral dose distribution. Therefore, higher energies are generally used for therapy purposes, with the best results around 6 MeV since this energy is below the neutron production threshold for beam components.[9] Figure 1.2 shows photon depth dose vs depth and lateral dose in water. Note the buildup peak and tight lateral distributions, as well as the slow exponential decrease in dose after the buildup peak. [10]

Photons do not stop after the tumor site and deliver dose to sites beyond (Figure 1.2). The intensity falls off as

$$I = I_0 \exp(-\mu z) \quad 1.3$$

where μ is the linear attenuation coefficient for that material and $\lambda = \mu^{-1}$ is the mean free path as visible in Figure 1.3.[1] In photon therapy, tissues beyond the tumor always

receive unwanted dose. Clinically, photon therapy is well established however and is inexpensive compared with protons. A linear accelerator is cheaper for a hospital to operate than a cyclotron or synchrotron and it remains a popular treatment modality.

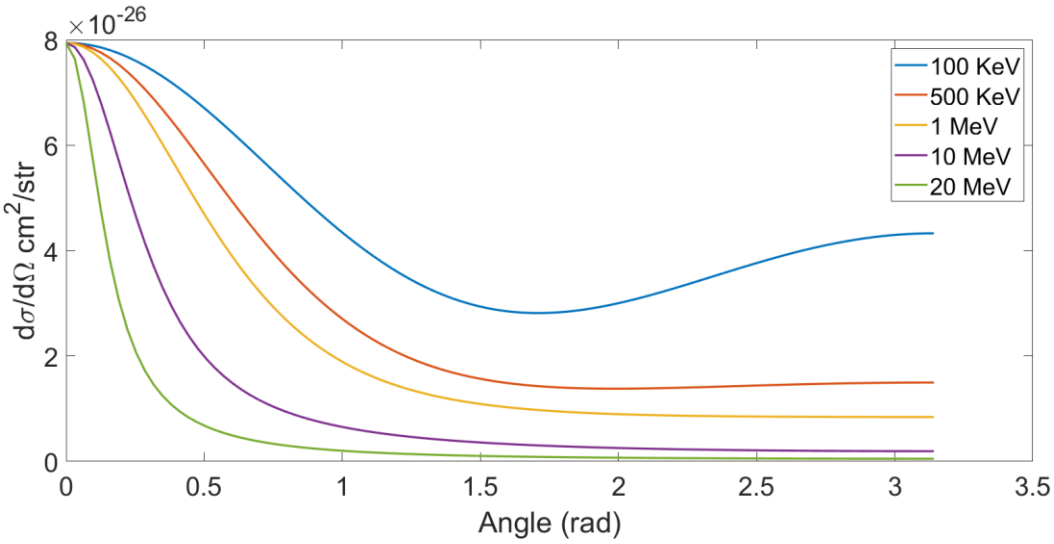

Figure 1.1. Klein Nishina scattering cross section in water.

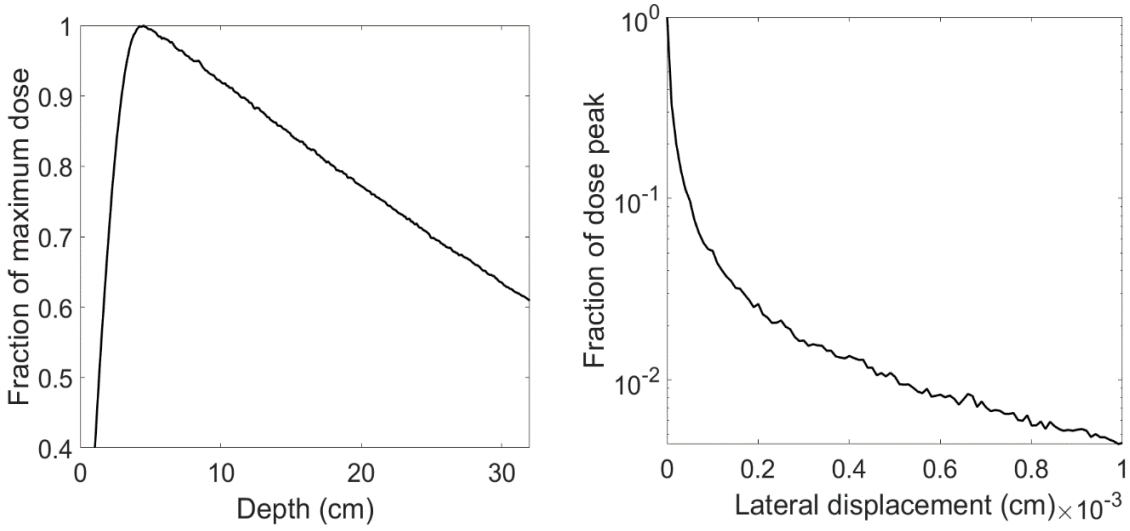

Figure 1.2. Photon depth dose and lateral dose curve. Pristine 6 MeV photon beam at 4cm depth calculated with FLUKA.

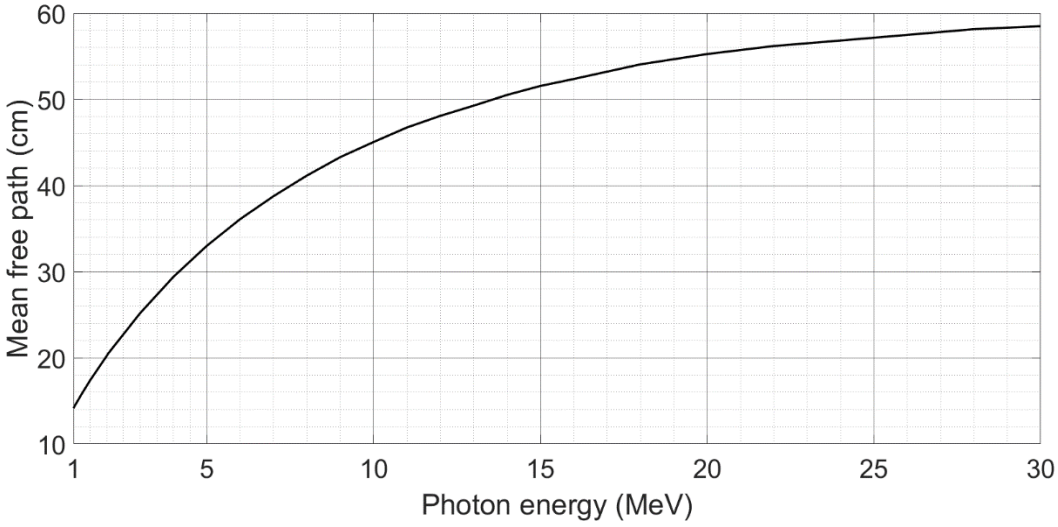

Figure 1.3. The photon mean free path in water. This is the inverse of the attenuation coefficient μ in equation 1.3. [11-13]

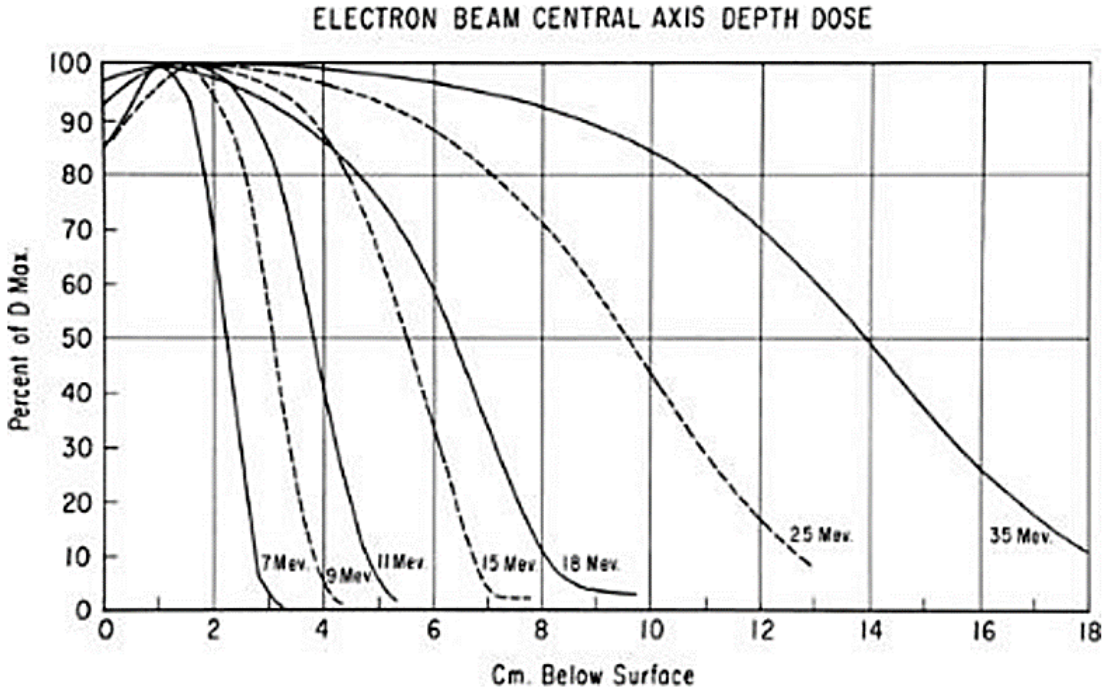

Figure 1.4. Electron beam central axis depth dose. (Taken from Tapley[14]).

In electron beam therapy, electrons ionize other, atomic electrons in their path and emit bremsstrahlung as they pass through atomic electric fields[15, 16]. There is a buildup region due to electron scattering in the absorber, a peak dose, and then gradual fall off due to angular scattering, Bremsstrahlung and electron capture by atoms. Near the end of the range, a previously mono-energetic electron beam is composed of many energies. This leaves electrons without a well-defined Bragg peak. [8, 17] (Figure 1.4). Electrons are well suited to shallow tumors since unwanted dose beyond the treatment region is less significant than for photon therapy. At higher energies, angular scattering and x-rays smear out the dose falloff.[1]

Protons were discovered experimentally by Ernest Rutherford in 1919 [18] and were used in the first linear accelerator, built by Cockcroft and Watson in 1930. In 1932 the first cyclotron was invented by Ernest Lawrence. This machine allows the acceleration of ions held in a magnetic field using a weak EM field.[19]. The largest cyclotron could accelerate protons to 730 MeV. [20]. In 1946, Wilson[21] suggested that protons be used to treat tumors. The synchrotron was invented in 1947 and allows frequency adjustment of the electric field as the particles approach the speed of light.[22] In 1954 Lawrence Berkeley National Laboratory began the first treatments of humans. The synchrotron group in Uppsala, Sweden soon followed that year.[23] The Harvard cyclotron began treatments in 1961 and Loma Linda University Medical Center began treatments in 1990.[24] Today, synchrotrons-cyclotrons, cyclotrons and linear accelerators are all used for treatment in a clinical setting. [25]

Protons have some important advantages for therapy purposes over other forms of radiation. Firstly, proton elastic scattering is very forward peaked. This is visible in

Figure 1.9. They also have the advantage of a well-defined dose (or "Bragg) peak visible in Figures 1.5 and 1.10a. Clinical energy protons are sub-relativistic and so unlike electrons, they do not experience Bremsstrahlung. [16] These characteristics allow conformity of dose to the tumor site that is superior to either photons or electrons.

Clinical evidence is mounting that proton therapy delivers improved patient outcomes compared with photons and electrons. Emerging studies of pediatric salivary gland tumors treated with protons indicate less dysphagia and weight loss, lower dose to surrounding tissues and lower total body dose. [26] Other studies report "excellent" median survival times.[27] Treatment with protons achieved "significant dose reductions" compared to photon stereotactic body radiation therapy in non-small lung cancers. [28] Researchers have found that protons reduce the risk of radiation pneumonitis in lung tumor patients compared to photons when combined with a chemotherapy regime,[29]. Thirty-eight percent (38%) lower dose to bone marrow has been reported for cervical cancer patients.[30] Six pediatric medulloblastoma patients treated with passively scattered proton therapy had a lower risk of secondary radiogenic cancers and lower cardiac mortality than with field-in-field photon therapy. [31]. A broad study of photon vs proton therapy found similar patient survival rates outcomes with fewer side effects.[32] Clinical research comparing proton therapy with other treatment modalities is ongoing.

In the clinical setting, inverse treatment planning is used to minimize dose to organs while maintaining the prescribed dose to the target volume. This requires simulating many configurations of fields, energies, angles and intensities.[33] It is therefore critical to calculate the dose for each configuration quickly and accurately. To do this, one needs to model beam scattering and energy loss.

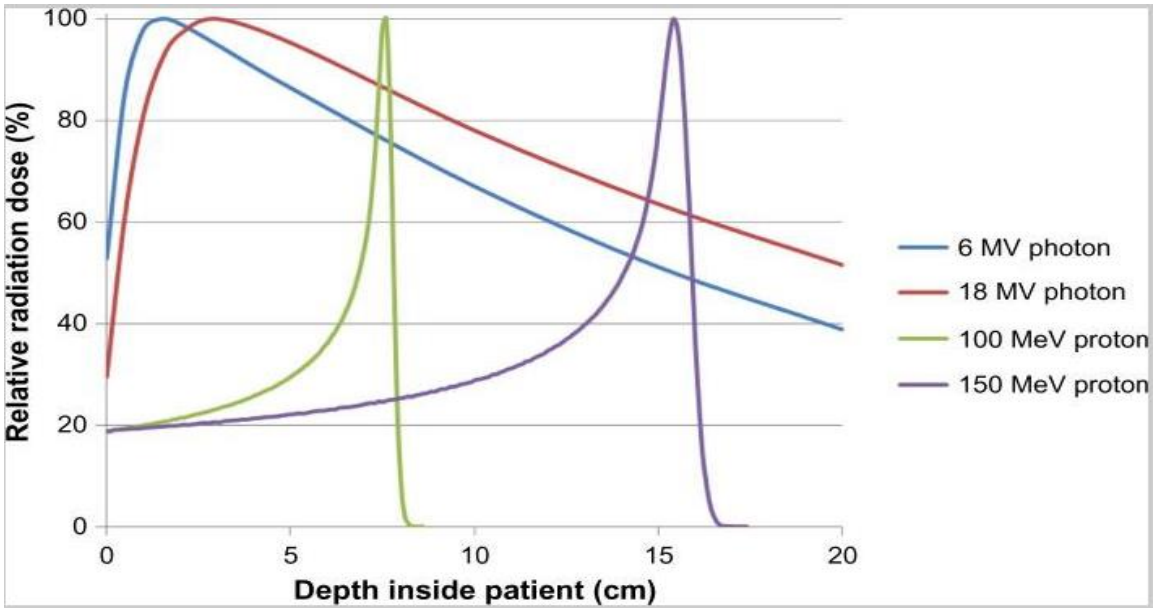

Figure 1.5. Proton beam "Bragg Peak." (Taken from Wang[34])

The human body is 60% water. Therefore, to first order, the human body may be treated as a "water phantom" which is a tank of liquid water. Clinically, water tanks are used to calibrate accelerators and non-water materials in the human body are scaled to water by the ratio of the stopping power in units of g/cm^2 [35]. For this reason, scattering and energy loss calculation will be for protons in water or beamline components such as graphite, iron or tungsten.

The clinically relevant scale for dose calculations is no smaller than a Computed Tomography (CT) voxel, or about 1mm.[36] Imaging ambiguity at scales below this provides a lower limit for calculation precision. This size also sets a lower limit for the energies of the beam. A range in water of 1mm corresponds to a residual energy of 350 keV for electrons and 9.5 MeV for protons[10]. Energies less than this are deposited within a CT voxel. The upper limit is set by maximum patient size. Ranges of 33cm,

corresponding to 230 MeV for protons and 20 MeV for electrons include all tumor depths.

The total elastic cross section, and its reciprocal the elastic mean free path, may be found by integrating the single elastic scattering differential cross section $\sigma(\Omega)$ over the solid angle Ω, composed of the polar angle χ and azimuthal angle φ. Since radiotherapy beams are necessarily unpolarized due to scattering in beamline components and scattering centers of the target are randomly oriented, the differential cross section has azimuthal symmetry.

$$\sigma_{el} = \int \sigma(\Omega) d\Omega = \int_0^{2\pi} \int_0^{\pi} \sigma(\theta, \varphi) \sin\chi d\chi d\phi = -2\pi \int_1^{-1} \sigma(\chi) dcos\ \chi \qquad 1.4$$

The elastic mean free path is then

$$\frac{1}{\lambda_{el}} = N\sigma_{el} \qquad 1.5$$

Where $N = \rho N_A/A$ is the number of scattering centers per unit volume, N_A is Avogadro's number and A is the atomic weight. From Figure 1.7 we can see that the longest mean free path of elastic scattering for clinical energy protons in water is about 400nm, corresponding to approximately 2500 elastic mean free paths in a 1 mm depth slice. At a 1 mm length scale then, elastic coulomb scattering is a stochastic process involving many interactions. Each interaction is mutually independent and described by the single scattering cross section $\sigma(\Omega)$. While it is possible to calculate the trajectory of each interaction directly from the single scattering cross section, at the 1 mm scale and above that is relevant for clinical purposes the many single scattering events can be described by a probability distribution function in terms of a multiple scattering angle. The evolution of the phase space of the proton beam, including the probability angle distribution is

described by the Boltzmann transport equation in terms of the single scattering cross section. In the next section, we will review proton kinematics and then transport methods for elastic coulomb scattering. In subsequent chapters, we will discuss Molière's theory of coulomb elastic scattering and transport methods for inelastic coulomb scattering. Lastly, we will cover nuclear scattering. The transport methods apply most specifically to protons of clinical energy though occasionally some physics may apply to electrons or protons outside the clinical energy regime. MathWorks MATLAB™ R2021b (Update 3) was used to perform numerical calculations and create most plots. These methods may be generalized for inclusion in a Monte Carlo code or physics engine in a treatment planning system (TPS). Comparisons are made with FLUKA Monte Carlo, which has been shown to provide an adequate description of proton physics for therapy purposes.[37-40]

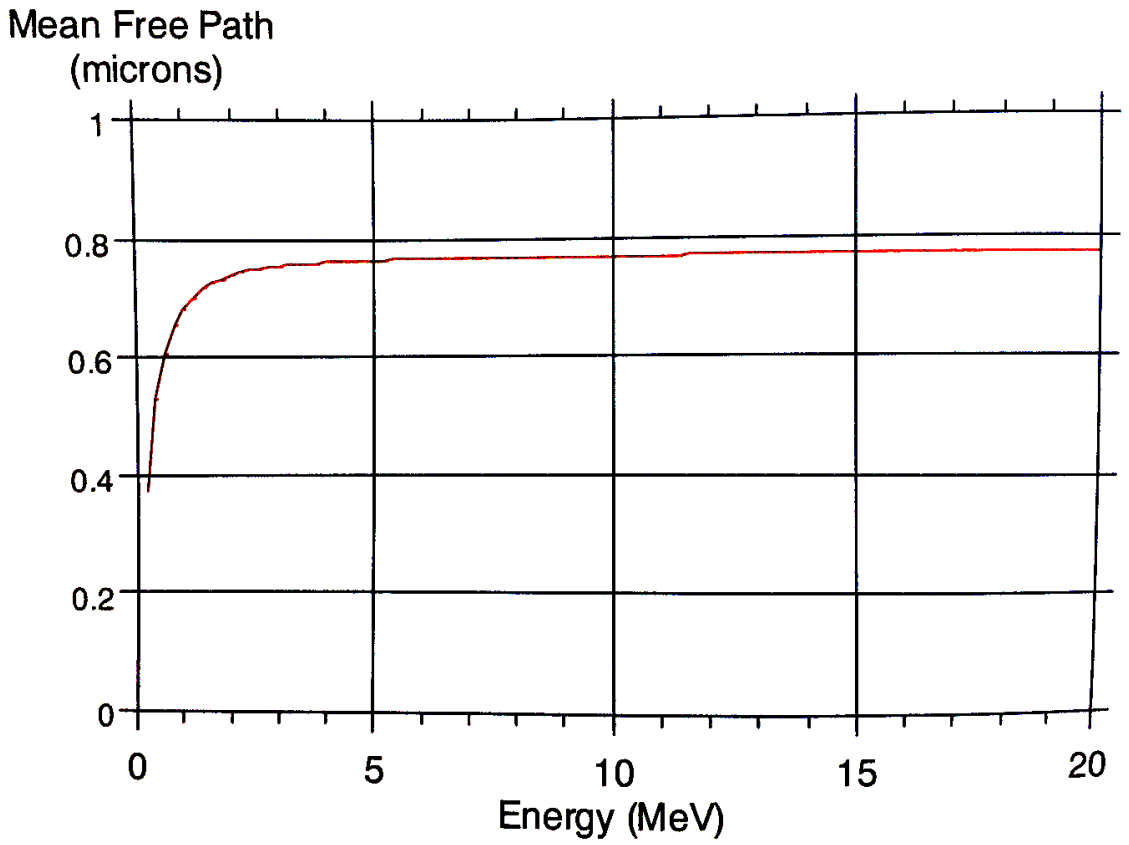

Figure 1.6. The elastic coulomb scattering mean free path of electrons in water. This is smaller than a human cell (1 micron) or a 1 mm CT voxel.[41] (Taken from P. Rez)

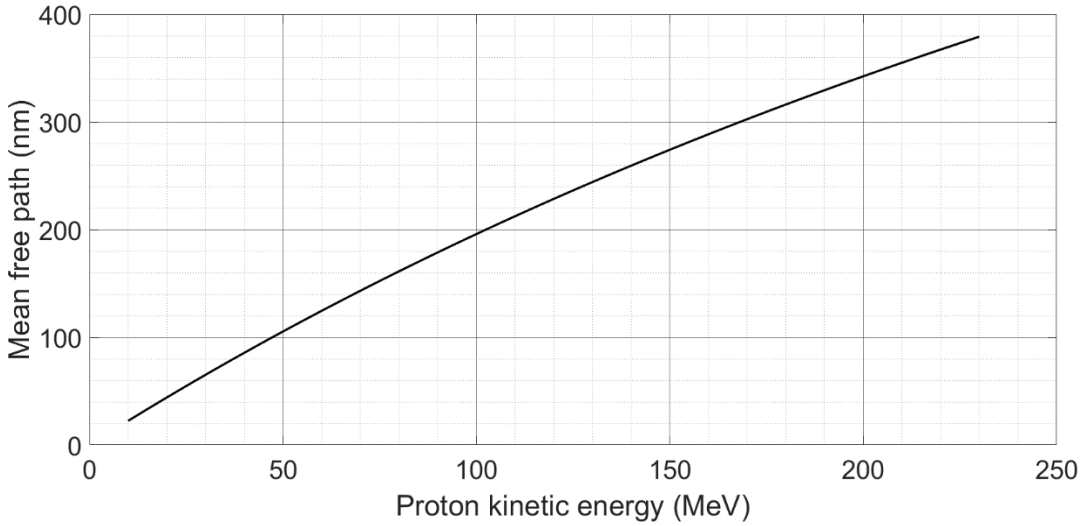

Figure 1.7. Elastic mean free path vs energy of proton coulomb scattering in water. [41]

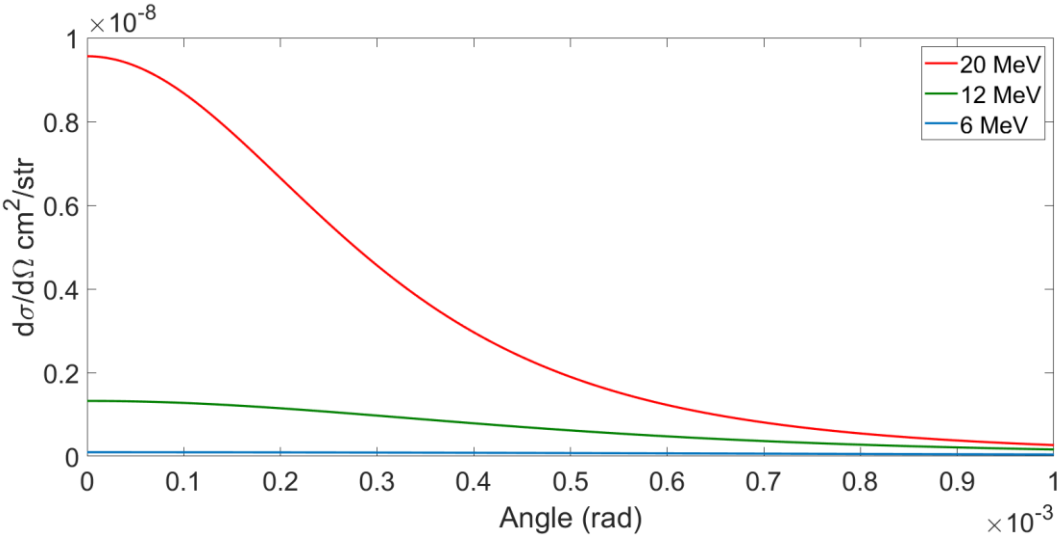

Figure 1.8. Differential cross section of electron elastic coulomb scattering in water.

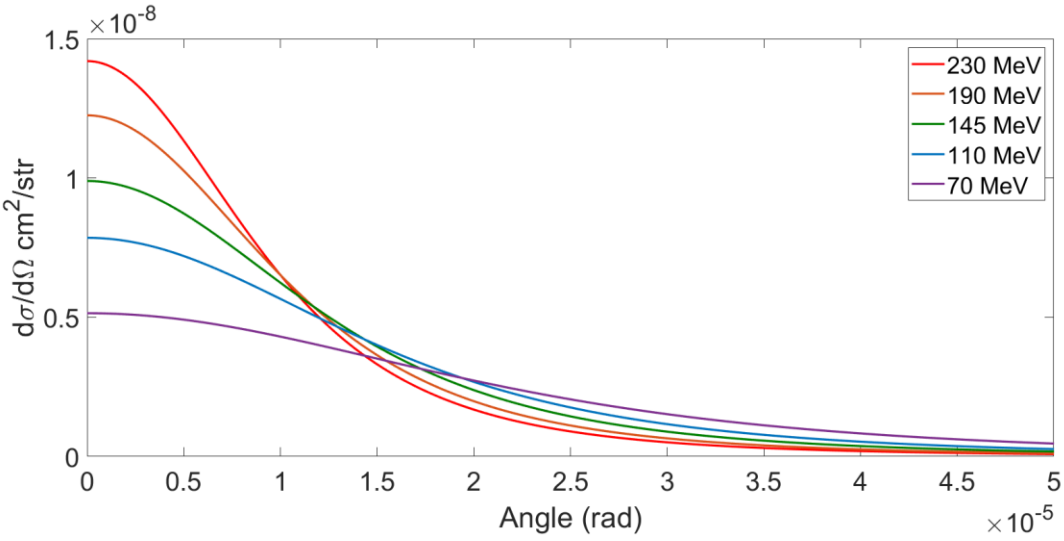

Figure 1.9. Differential cross section of proton elastic coulomb scattering in water.

Proton Kinematics

The relevant length and energy scales for proton radiotherapy are centimeters (cm) and million electron volts (MeV). Cross sections are described in terms of cm^2 or millibarns. Proton single scattering probabilities depend on the momentum p and velocity v because the kinematics of the elastic cross section are determined by momentum

transfer of the coulomb interactions with atoms. Electron single scattering probabilities depend on the velocity as a fraction of the speed of light, β. This is due to a cancellation of the electron rest mass $m_e c^2$ with the coulomb potential $r_e(m_e c^2)$ in $\sigma(\Omega)$ where r_e is the classical electron radius. pv and β can be expressed in terms of the kinetic energy E and rest energy of the particle[42] As given by Gottschalk:

$$\tau = \frac{E}{mc^2} \tag{1.6}$$

$$pv = \frac{\tau + 2}{\tau + 1} E \tag{1.7}$$

$$\beta^2 = \frac{\tau + 2}{(\tau + 1)^2} \tau \tag{1.8}$$

Protons undergoing inelastic scattering in the clinical energy regime have an average energy loss given by the Bethe formula

$$\frac{\bar{\Delta}}{z} = 0.3068 \frac{1}{\beta^2} \frac{Z\rho}{A} \ln\left(\frac{2m_e c^2 \beta^2}{(1-\beta^2)I} - \beta^2\right) MeV \tag{1.9}$$

Electron mean energy loss is generally not equivalent to proton mean energy loss for projectiles of the same velocity due to exchange terms in the stopping power[43] and bremsstrahlung at higher energies[44]. Since the proton energy loss per unit length is inversely proportional to β^2, the energy losses are parabolic as $\beta^2 \to 0$, presenting a well defined energy peak. The Bragg peak would be even more sharply defined if not for energy straggling, which causes a more rounded peak. Note the slightly rounded Bragg peak in figure 1.10.a. The energy loss Δ in terms of the average energy loss $\bar{\Delta}$ in a length z is

$$\left(\frac{\bar{\Delta}}{z}(E)\right) z = \Delta \tag{1.10}$$

With the continuous slowing down approximation, energy loss along the particle path is assumed to be equal to the total stopping power[10]

$$R = \int_0^{E_0} \left(\frac{\bar{\Delta}}{z}(E)\right)^{-1} dE \qquad 1.11$$

Where E_0 is the initial energy of the proton beam. In practice, finding the energy loss using Equation 1.9 requires extremely small depth intervals dz.

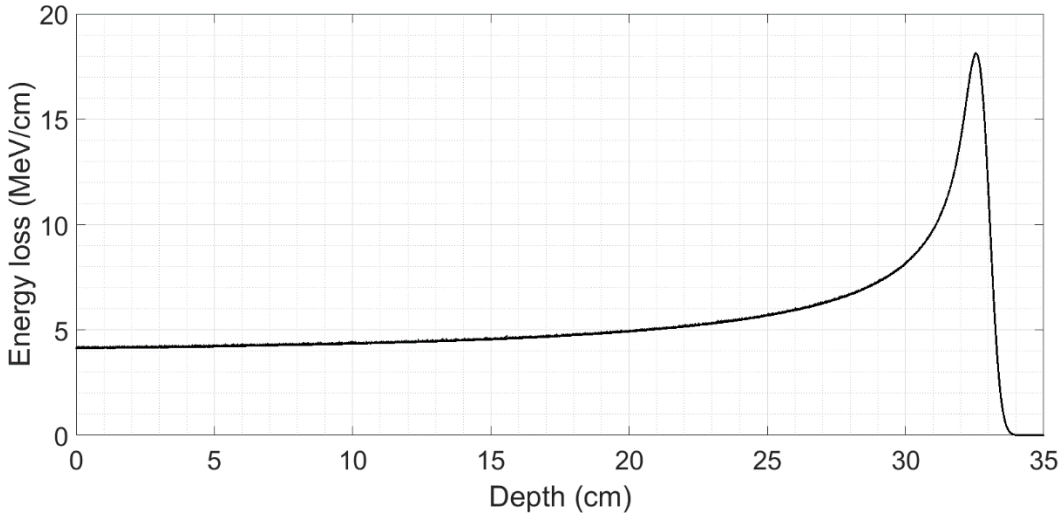

Figure 1.10a. Energy loss of primary protons vs depth for 230 MeV proton beam. Simulated with FLUKA Monte Carlo.[37, 39, 45-47]

If we assume the continuous slowing down approximation, the range of a proton in a material can be described using the Bragg-Kleeman rule as

$$R = aE_0^b \qquad 1.12$$

Where a and b are fitting parameters.[48] For water, $a = 0.002532$ and $b = 1.742$ from fitting to PSTAR[10] range tables.

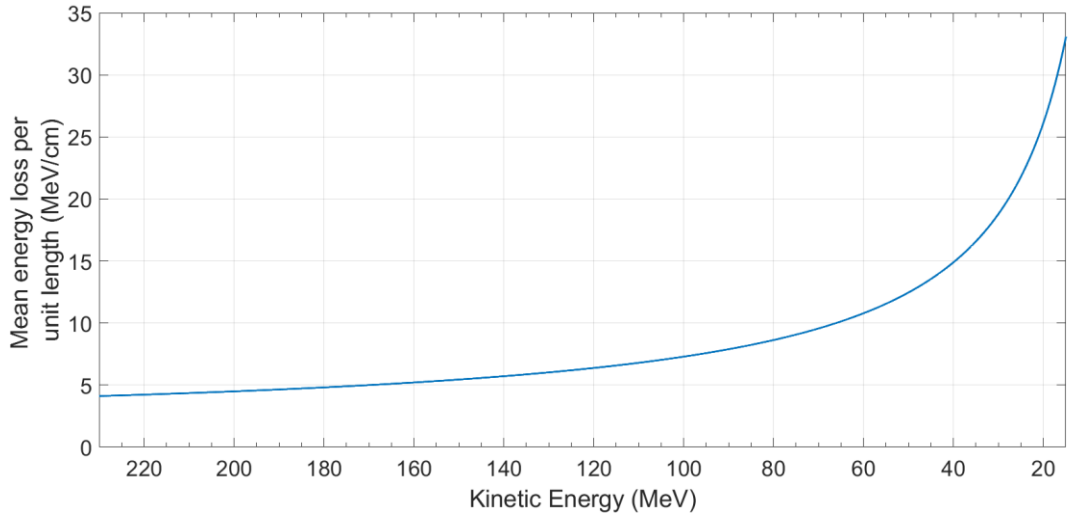

Figure 1.10b. Proton mean energy loss vs energy from the PSTAR database.[10]

There is a simple empirical relation between $(pv)^2$, initial $(p_1v_1)^2$ and R given by Øverhås[49] equation (89) in terms of k from Schneider[49, 50]

$$(pv)^2 = (p_1v_1)^2\left(1 - \frac{z}{R}\right)^{k+1} \quad 1.13$$

$$k = 0.12e^{-0.09\rho X_0} + 0.0753 \quad 1.14$$

For water, $k \approx 0.09$ and is set to zero in "weak Øverhås" so that equation 1.13 becomes

$$(pv)^2 = (p_1v_1)^2\left(1 - \frac{z}{R}\right) \quad 1.15$$

X_0 is the radiation length as given by Rossi[51].

$$\frac{1}{X_0} = 4\alpha\frac{N_A}{A}r_0 \ln\left(183Z^{-\frac{1}{3}}\right) \quad 1.16$$

It is defined as the average distance that a relativistic charged particle travels before its energy drops to $1/e$ of its initial energy.[52]

The kinetic energy of a particle can be found from pv with the relation

$$E = \frac{1}{2}\left[pv - 2m_pc^2\right] + \sqrt{\frac{(pv)^2}{4} + m_pc^2} \quad 1.17$$

So that to find the energy loss in a depth interval dz, one may take

$$\Delta E = E(pv)_i - E(pv)_f \tag{1.18}$$

Where $E(pv)_i$ and $E(pv)_f$ are the energies determined by pv at an initial and final depth z, respectively.

The Transport Equation

Imagine a particle in six-dimensional phase space defined by position and velocity, such that the number of particles in the distribution $f(\vec{r}, \vec{v})$ is the number of particles in $d\vec{r}d\vec{v}$. The time evolution of distribution function $f(\vec{r}, \vec{v})$ is conserved by Liouville's theorem[53] such that it obeys the continuity equation

$$\left(\frac{\partial f}{\partial t}\right) + \vec{v} \cdot \nabla f = 0 \tag{1.19}$$

where the change in the probability distribution of a phase space f with time depends on the change in position of the particles. For elastic scattering, the probability of particles in a phase space with polar angle θ, azimuthal angle φ and energy E scattering into a phase space element with position $\vec{r}$, polar angle θ', azimuthal angle φ' and energy E' is solely determined by the cross section σ of that phase space volume (see Figure 1.11) and is conserved such that

$$\begin{aligned} &N \iiint \sigma(\theta, \varphi, E, \theta', \varphi', E') v' f(r, \theta', \varphi', E') \sin\ \theta' d\theta' d\varphi' dE' \\ &= N \iiint \sigma(\theta', \varphi', E', \theta, \varphi, E) v f(r, \theta, \varphi, E) \sin\ \theta' d\theta' d\varphi' dE' \end{aligned} \tag{1.20}$$

Or assuming the continuous slowing down approximation, the path length can be expressed as the change in position of the particles with time $z = vt$. Combining equations 1.19 and 1.20

$$\left(\frac{\partial f}{\partial z}\right) + \nabla f = N \iiint \sigma(\theta, \varphi, E, \theta', \varphi', E') f(\theta', \varphi', z) \sin\ \theta' d\theta' d\varphi' dE'$$
$$-N \iiint \sigma(\theta', \varphi', E', \theta, \varphi, E) f(\theta, \varphi, z) \sin\ \theta' d\theta' d\varphi' dE' \qquad 1.21$$

This is the form of the elastic scattering transport equation as given by Fathers and Rez.

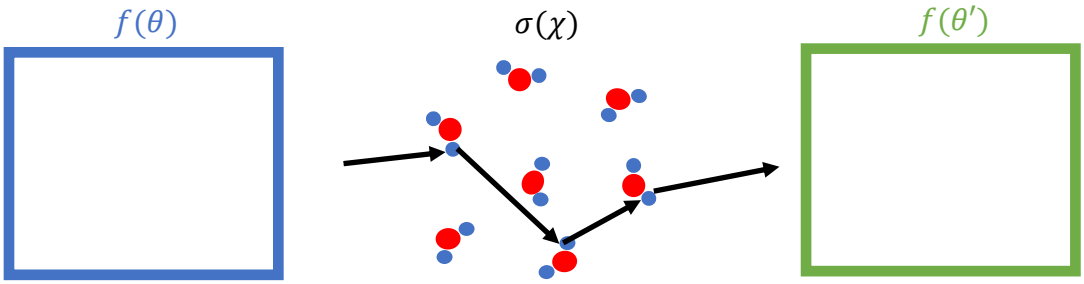

Figure 1.11. Transport equation illustration. Simplified to one dimension θ.

Bethe, Rose and Smith (BR&S) assign the vector $\vec{u}$ and $\vec{u}'$ to the directions of scatter in and out of a phase space volume. $\sigma(\vec{u} - \overrightarrow{u'})$ is the single scattering cross section through angle α between the unit vectors $\vec{u}$ and $\vec{u}'$. BR&S obtain [54]

$$\left(\frac{\partial}{\partial z} + \vec{u} \cdot \nabla\right) f(\vec{u}) = N \iint [\sigma(\vec{u} - \vec{u}') f(\overrightarrow{u'}) - \sigma(\vec{u}' - \vec{u}) f(\vec{u})]\, d\vec{u}' \qquad 1.22$$

Where $f(\vec{u})$ is the probability that a particle scatters along the vector $(\vec{u})$. In terms of α, the angle between the unit vectors $\vec{u}$ and $\vec{u}$

$$\left(\frac{\partial}{\partial z} + \vec{u} \cdot \nabla\right) f(\vec{u}) = N \iint \sigma(\alpha)[f(\vec{u}') - f(\vec{u})] d\vec{u}' \qquad 1.23$$

Expanding $f(\vec{u}')$ as a Taylor series in powers of $\vec{w}$ where $\vec{w} = \vec{u} - \vec{u}'$, $|\vec{w}| = 2 \sin\frac{\alpha}{2}$ and $w_x = w \cos\beta$ and $w_y = w\ sin\ \beta$ where β is the azimuthal angle

$$f(\vec{u}') - f(\vec{u}) = w_x \frac{\partial f}{\partial u_x} + w_y \frac{\partial f}{\partial u_y} + \frac{1}{2} w_x^2 \frac{\partial^2 f}{\partial u_x^2} + \frac{1}{2} w_y^2 \frac{\partial^2 f}{\partial u_y^2} + w_x w_y \frac{\partial f}{\partial u_x} \frac{\partial f}{\partial u_y} \qquad 1.24$$

Setting the transport mean free path

$$\frac{1}{\lambda_{tr}} = 2\pi \int_0^{\pi} \sigma(\alpha)(1 - cos\alpha) d\alpha \qquad 1.25$$

and averaging over β, w_x and $w_y$vanish leaving the Fokker plank equation (BR&S) [54]

$$\left(\frac{\partial}{\partial z}+\vec{u}\cdot\nabla\right)f(\vec{u})=\frac{1}{\lambda_{tr}}\nabla^2 f(\vec{u}) \tag{1.26}$$

We find the probability distribution determined by the transport mean free path λ_{tr}.[55] Expanding ∇^2 in spherical polar coordinates with the small angle approximation and azimuthal symmetry [51], [56]

$$\frac{\partial f}{\partial z}=-\theta\frac{\partial F}{\partial y}+\frac{1}{\lambda_{tr}}\frac{\partial^2 F}{\partial\theta^2} \tag{1.27}$$

Where y is the lateral displacement from the central axis. Equation 1.26 has the solution, from Rossi and Greisen[51],

$$F(z,y,\theta)=\frac{\sqrt{3}}{2\pi}\frac{\lambda_{tr}}{t^2}\exp\left[-\lambda^2\left(\frac{\theta^2}{z}-\frac{3y\theta}{z^2}+\frac{3y^2}{t^3}\right)\right] \tag{1.28}$$

Integrating over the spatial coordinate y gives the angle distribution

$$\int_{-\infty}^{\infty}F(z,y,\theta)dy=\frac{1}{2\sqrt{\pi}}\sqrt{\frac{\lambda_{tr}}{z}}\exp\left[-\frac{1}{4}\left(\frac{\lambda\theta^2}{z}\right)\right] \tag{1.29}$$

And integrating over the scattering angle from the central axis θ gives the spatial distribution

$$\int_{-\infty}^{\infty}F(z,y,\theta)d\theta=\frac{\sqrt{3}}{2\sqrt{\pi}}\sqrt{\frac{\lambda_{tr}}{z^3}}\exp\left[-\frac{3}{4}\left(\frac{\lambda y^2}{z^3}\right)\right] \tag{1.30}$$

These Gaussian probability functions are the Fermi-Eyges pencil beam algorithms used by Hogstrom et al, and Russell. [56] [57] [58] [59] They describe the probability of the lateral beam spreading in a slice of depth z at positions y and angle θ. Rossi and Greisen find the RMS scattering angle of equation 1.29 in terms of the transport mean free path

$$<\theta^2>=\frac{2z}{\lambda_{tr}} \tag{1.31}$$

Where $\sqrt{< \theta^2 >} = \theta_0$ and

$$\theta_0 = \frac{E_s}{pv}\sqrt{\frac{z}{X_0}} \tag{1.32}$$

$$E_s = \sqrt{\frac{4\pi}{\alpha}} m_e c^2 = 21\ Mev \tag{1.33}$$

Where equation 1.32 has an additional factor of $1/\sqrt{2}$ when in terms of the projected angle. For a cross section with $1/\theta^4$ dependence, the transport mean free path λ_{tr} is proportional to[51] (see equations 2.25 to 2.27)

$$\frac{1}{2}\left(\log\left(\frac{\theta_{max}^2}{\theta_{min}^2}\right) - 1\right) \tag{1.34}$$

Williams defines θ_{max} in terms of the ratio of the projectile Debroglie wavelength to the nuclear radius,

$$\theta_{max} \sim \frac{\lambda}{2\pi r_{nuc}} \tag{1.35}$$

since for angles smaller than θ_{max}, the nucleus is effectively a point charge. [60] For angles larger than θ_{max}, there is a phase difference between secondary waves scattered from individual nucleons and a reduced contribution to the mean square scattering angle $< \theta^2 >$. The mean square scattering angle in the Gaussian approximation is therefore proportional to the ratio of the atomic radius to the nuclear radius. This can be seen in Rossi and Greisen[42, 51] who take

$$r_{nuc} = 0.57 r_e Z^{\frac{1}{3}} \tag{1.36}$$

Which is a curve fit of the nuclear radii to their atomic number. A more accurate fit is to the atomic weight A as in ICRU35. [42, 61]

$$r_{nuc} = 0.49 r_e A^{\frac{1}{3}} \quad 1.37$$

Goudsmidt and Saunderson (G&S) [62] exploit the fact that the elastic coulomb scattering is a compound Poisson process, with the probability $W(n)$ from G&S equation (12) that a particle has n collisions

$$W(n) = \frac{e^{-v} v^n}{n!} \quad 1.38$$

Where v is the average number of collisions, G&S equation (11)

$$v = zN\sigma_{el} \quad 1.39$$

In terms of Legendre polynomials, the average scattering angle after n collisions is the nth power of the average of the polynomials after one collision. The average of the Legendre polynomial is G&S equation (4)

$$G_l = \sum_0^\infty W(n) < P_l(\cos\theta_1) >_{Av}^n \quad 1.40$$

Inserting equation 1.38 into 1.40, or G&S in their equations (4), (13) and (14)

$$f(\theta) = \frac{1}{4\pi} \sum (2l+1) G_l P_l(\cos\theta) \quad 1.41$$

$$G_l = \sum e^v v^n P_l \frac{< \cos\theta >_{Av}^n}{n!} = e^{-vQ_l} \quad 1.42$$

Inserting equation 1.39 into 1.42 and taking $Q_l = 1 - < P_l(\cos\theta_1) >_{Av}$

$$G_l = \exp\left[-zN \int \sigma(\chi)(1 - P_l(cos\,\chi) d\Omega\right] \quad 1.43$$

Here χ is distinguished from θ because χ is the single scattering angle associated with the single scattering cross section $\sigma(\chi)$ whereas θ is the *multiple* scattering angle after many interactions. By the central limit theorem of statistics, the mean squared scattering angle $< \theta^2 >$ is the variance of a gaussian distribution for a large number of interactions.

For a small number of interactions characteristic of very thin targets, it tends toward the single scattering distribution of the differential cross section. In proton radiotherapy where the minimum relevant length scale is 1 mm, the single scattering limit is never reached except at large scattering angles for targets of thin and intermediate thickness.

In the theory of Goudsmidt and Saunderson for large angles that are much greater than $< \theta^2 >$, the probability angle distribution tends to the single scattering distribution. Molière will make use of this fact to define his cross section in terms of the deviation from the single scattering cross section of Rutherford.

In the Gaussian limit $1 - P_l(\cos\chi)) = \frac{1}{4} l(l+1) < \theta^2 >$ in equation 1.43 so that

$$G_l = \exp\left[-2\pi z N \int \frac{1}{4}\big(l(l+1)\big)\chi^2 \sigma(\chi) d\Omega\right] \qquad 1.44$$

Equivalently, Lewis found that the Goudsmidt and Saunderson distribution can be found from the transport equation by assuming the phase space does not change with time (the steady state solution) [63]

One needs a very large number of Legendre polynomials for forward peaked scattering in the theory of Goudsmidt and Saunderson. This problem can be alleviated by expressing the Legendre polynomials as Bessel functions and integrating over the η parameter corresponding to the order of the Legendre polynomials (to infinity). This is the approach taken by Molière in the next chapter.

Snyder and Scott (S&S) [55] solve the transport equation in cartesian coordinates by projecting the differential single cross section in the transport equation onto the x-axis where $\chi^2 = \theta_x^2 + \theta_x^2$. S&S equation (4) is

$$\sigma_{proj}(\theta_x) = \int_{-\infty}^{\infty} \sigma\big(\sqrt{\theta_x + \theta_x}\big) d\theta_y \qquad 1.45$$

The transport equation is then S&S equation (3)

$$\left(\frac{\partial}{\partial z}+\theta_x\frac{\partial}{\partial x}\right)f(\theta_x,x|z)=N\int_{-\infty}^{\infty}\sigma_{proj}(\theta_x)[f(\theta_x',x|z)-f(\theta_x,x|z)]d\theta_x' \qquad 1.46$$

Where $f(\theta_x,x|z)$ is the probability distribution function for projection of scattering onto the xz plane. In equations (7), (8) and (9) S&S solve the transport equation with Laplace and Fourier transforms, so that

$$f(\theta,z)=Real\left\{\frac{1}{\pi}\int_0^{\infty}e^{i\eta\theta_x}g(\eta,z)d\eta\right\} \qquad 1.47$$

$$g(\eta,z)=\exp\left[-zN\int_{-\infty}^{\infty}\left(1-e^{i\eta\theta_x}\right)\sigma_{proj}(\theta_x)d\theta_x\right] \qquad 1.48$$

$$f(\theta_x,x|z)=Real\left\{\frac{1}{\pi}\int_0^{\infty}\exp\left[e^{i\eta\theta_x}-zN\int_{-\infty}^{\infty}\left(1-e^{i\eta\theta_x}\right)\sigma_{proj}(\theta_x)d\theta_x\right]\right\} \qquad 1.49$$

Equation 1.48 determines the number of elastic scattering events $g(\eta,z)$ as a function of the reciprocal projected scattering angle η. The inverse Fourier transform of which gives the probability angular distribution in terms of the projected multiple scattering angle θ_x.

To describe scattering in terms of a polar angle θ, the $f(\theta_x,x|z)$ must be projected back onto the polar scattering angle θ.[64] Molière theory in the next chapter differs from S&S's treatment in that Molière solves the transport equation in terms of the polar angle θ and the transforms are therefore in the form of Bessel functions.

CHAPTER 2

MOLIÈRE THEORY

Rutherford scattering from the Born Approximation

The probability of deflection of an individual proton through a solid angle by the coulomb field of an atomic nucleus can be described in terms of the differential cross section $\sigma(\chi)$, which can be obtained from the scattering amplitude $f(\Omega)$.[65] Following Zetilli, Sakurai and Martin

$$\sigma(\chi) = |f(\Omega)|^2 \tag{2.1}$$

To find the scattering amplitude we can take a first order plane wave approximation, or the first order Born approximation, valid when the kinetic energy of the incident particle is much greater than the average interaction energy.[66]. The scattering amplitude in the Born approximation is [65, 67, 68].

$$f^{(1)}(\Omega) = -\frac{m}{2\pi\hbar^2}\int d^3r' e^{i\boldsymbol{q}\cdot\boldsymbol{r}'} V(\boldsymbol{r}') \tag{2.2}$$

Where m is the reduced mass in the proton-target system $m = \frac{m}{\left(1+\frac{m}{M}\right)}$.[69] Although the incident proton interacts with the coulomb field of the atomic nucleus, the nucleus is "screened" by atomic electrons. The screened coulomb potential of an atomic nucleus can be written as[68]

$$V(r) = \frac{ge^{-\mu r}}{r} \tag{2.3}$$

This is the screened coulomb potential[70] with inverse screening length μ and scaling constant $g = Zr_e(m_e c^2)$ in terms of the classical electron radius $r_e = 2.818 \times 10^{-13}\ cm$, electron rest energy $m_e c^2 = 0.511\ MeV$ and atomic number Z of the target material.

Since the potential equation 2.3 is spherically symmetric, we can integrate over the azimuthal angle, leaving the cross section in terms of the single scattering angle χ.

$$f(\chi) = -\frac{2m}{\hbar^2}\frac{1}{q}g\int_0^\infty r'V(r')\sin qr'\,dr' \tag{2.4}$$

$$f(\chi) = -\frac{2m}{\hbar^2}g\left(\frac{1}{q^2+\mu^2}\right) \tag{2.5}$$

For elastic scattering, the magnitude of the wave vectors before after the collisions are equal and the momentum transfer is therefore $q = |\boldsymbol{k} - \boldsymbol{k}'| = 2k\sin\frac{\chi}{2}$.

$$f(\chi) = -\frac{2m}{\hbar^2 k^2}g\left(\frac{1}{4\sin^2\frac{\chi}{2}+\frac{\mu^2}{k^2}}\right) \tag{2.7}$$

We set

$$\frac{pv}{2} = \frac{\hbar^2 k^2}{2m} \tag{2.8}$$

Where pv is the product of the relativistic momentum and velocity, which can be calculated using equations 1.6 to 1.8, 1.12 to 1.15 and 1.17. μ^2/k^2 gives the minimum scattering angle [51, 55] as determined by the ratio of the Debroglie wavelength λ to the size of atom.[52]

$$\frac{\mu^2}{k^2} = \frac{\lambda^2}{4\pi^2 a^2} = \chi_{min}^2 \tag{2.9}$$

The atomic radius is $a = 0.855a_0Z^{-1/3}$ where a_0 is the Bohr radius and 0.855 is the Thomas-Fermi constant[71].

Then the cross section is, in terms of the classical electron radius r_e

$$\sigma(\chi) = |f(\chi)|^2 = \frac{4Z^2r_e^2(m_ec^2)^2}{(pv)^2}\frac{1}{\left(4\sin^2\frac{\chi}{2}+\chi_{min}^2\right)^2} \tag{2.10}$$

which is the Yukawa or screened Rutherford cross section.[18, 70]. The single scattering amplitude falls off quickly at large angles and so we can take the small angle approximation $\sin\chi \approx \chi$.

$$\sigma(\chi) = \frac{4Z^2 r_e^2 (m_e c^2)^2}{(pv)^2} \frac{1}{(\chi^2 + \chi_{min}^2)^2} \qquad 2.11$$

In the limit $\chi_{min} \to 0$ the cross section goes over to the unscreened Rutherford cross section.

$$\sigma(\chi) = \frac{4Z^2 r_e^2 (m_e c^2)^2}{(pv)^2} \frac{1}{\chi^4} \qquad 2.12$$

In principle, the single scattering cross section provides a complete description of elastic proton scattering in a material. However, as can be seen in Figure 1.7, the elastic mean free path is much shorter than the relevant length scale in proton therapy, such that multiple scattering treatment is appropriate. Equation 2.12 is the starting place for Molière's theory of multiple scattering.

Molière theory

Molière theory is among the more successful multiple elastic scattering theories due to its excellent agreement with experiment. [47] It is based on the parameterization B of the effective number of elastic scattering events in a given depth based on a screening parameter χ_a. [72, 73] Molière assumes no explicit scattering cross section but describes the scattering probability in terms of its deviation from the unscreened Rutherford cross section equation 2.12.

Differences between Bethe and Molière's derivations

Molière theory is best known through a rigorous review by Bethe which includes some changes in the derivation of Molière's theory. [59] Some of these changes are

empirical in that they have been added to allow Molière theory to better fit measurements. Bethe (from Kulchitsky and Latyshev) substitutes $Z(Z+1)$ for Z in the differential cross section which was not present in Molière's original theory. [74] We have left out that change to the differential cross section here. Bethe (from Hanson) also incorporates the approximation $\sqrt{B} \to \sqrt{B-1.2}$ so that the zeroth order Gaussian $f^{(0)}$ is not too large when taken together with the first order term $f^{(1)}$. [75] This change is included. We use Bethe's derivation in terms of Bessel functions, rather than Molière's in terms of Hankel functions. Molière's 1947 and 1948 papers are referred to as I and II respectively when citing equations.

Bethe equation (1) begins with the elastic scattering transport equation in cylindrical coordinates, where the evolution of the multiple scattering probability distribution function $f(\theta, z)$ is determined by the single scattering cross section $\sigma(\chi)$

$$\frac{\partial f(\theta,z)}{\partial z} = -N * f(\theta,z) \int \sigma(\chi)\chi d\chi \; + \frac{N}{2\pi} \int f(\boldsymbol{\theta} - \mathbf{X}, \mathrm{t})\sigma(\chi)\chi d\chi d\phi \qquad 2.13$$

$\boldsymbol{\theta} - \mathbf{X}$ is the vector in the plane of the charged particle before the last scattering and ϕ is the azimuthal angle. Bethe equations (2) and (3) are the Bessel transforms

$$f(\theta,z) = \int_0^\infty \eta d\eta J_0(\eta\theta) g(\eta,t) \qquad 2.14$$

$$g(\eta,z) = \int_0^\infty \theta d\theta J_0(\eta\theta) f(\theta,z) \qquad 2.15$$

Bethe equation (4) solves equation 2.13 by applying the Bessel transform and the convolution theorem to obtain

$$g(\eta,z) = \exp\left[-zN \int_0^\infty \sigma(\chi)\chi d\chi (1 - J_0(\eta\chi))\right] \qquad 2.16$$

So that the multiple scattering probability density function (PDF) is Bethe equation (7)

$$f(\theta,z)=\int_0^\infty \eta d\eta J_0(\eta\theta)\exp\left[-zN\int_0^\infty \sigma(\chi)\chi d\chi(1-J_0(\eta\chi))\right] \quad 2.17$$

The exponent of Equation 2.16 is the number of elastic scattering events as a function of the reciprocal multiple scattering angle η. Molière equations I(E, 2) I(9,3) I(6, 5) and II(1,2) and Bethe equations (21) and (10) define the scattering angles,

$$\chi_a=\frac{\chi_{min}}{\sqrt{1.13+\frac{3.76Z^2\alpha^2}{\beta^2}}}=\frac{\lambda}{2\pi\left(0.855a_0Z^{\left(-\frac{1}{3}\right)}\right)\sqrt{1.13+\frac{3.76Z^2\alpha^2}{\beta^2}}} \quad 2.18$$

$$\chi_a'^2=1.167\chi_a^2 \quad 2.19$$

$$\chi_c^2=\frac{4\pi Nzr_e^2(m_ec^2)^2Z^2}{(pv)^2} \quad 2.20$$

Where χ_a is Molière's screening parameter obtained with the WKB approximation and α is the fine structure constant $\sim 1/137$.[72, 73].

Molière equations II(1,1), II(1,2) II(1,1') and Bethe equations (9) parameterize the scattering probability in terms of χ_c^2, equivalent to the cross section $\sigma(\chi)$ in the following relation (which includes a factor of 2π for azimuthal symmetry)

$$Nz\sigma(\chi)\chi d\chi=Nz\frac{8\pi Z^2r_e^2(m_ec^2)^2}{(pv)^2}\frac{q(\chi)}{\chi^4}\chi d\chi=\frac{2\chi_c^2\chi d\chi q(\chi)}{\chi^4} \quad 2.21$$

$q(\chi)$ describes the deviation of the scattering probability from the unscreened Rutherford cross section at small angles. At large angles, $q(\chi)=1$. Molière equation I(9,1) is

$$q(\chi)=\frac{\chi^4}{(\chi^2+\chi_a^2)^2} \quad 2.22$$

Inserting $Nz\sigma(\chi)\chi d\chi$ into equation 2.16 or Bethe equation (11)

$$\log g(\eta, z) = -2\chi_c^2 \int_0^\infty q(\chi)\chi^{-3} d\chi [1 - J_0(\eta\chi)] q(\chi) \quad 2.23$$

Bethe then splits equation 2.23 into two regions. In the small angle region where $\chi < \chi_g$ he approximates the Bessel function in equation 2.23 as Bethe equations (12), (13) and Molière equation (2,2)

$$1 - J_0(\chi\eta) = \frac{1}{4}\chi^2\eta^2 \quad 2.24$$

$$\int_0^{\chi_g} q(\chi)\chi^{-3} d\chi [1 - J_0(\eta\chi)] = \frac{1}{4}\eta^2 \int_0^{\chi_g} \frac{\chi^3}{(\chi^2 + \chi_a^2)^2} d\chi \quad 2.25$$

$$= \frac{1}{8}\eta^2 \left(\log \frac{\chi_g^2}{\chi_a^2} - 1 \right) \quad 2.26$$

From Molière II(2,2), the integral in equation 2.25 is equivalent to

$$\frac{1}{2\chi_c^2} \int_{e\chi_a^2}^{\chi_g} \sigma(\chi)\chi^3 d\chi = \frac{1}{2} \left(\log \frac{\chi_g^2}{\chi_a^2} - 1 \right) \quad 2.27$$

Which is the transport mean free path equation 1.25 in the small angle approximation $\sin\chi \approx \chi$. Combining with Molière equation I(2,3) The mean squared scattering angle is then

$$< \theta^2 >= \chi_c^2 B = \chi_c^2 \left(\log \frac{\chi_g^2}{\chi_a^2} - 1 \right) \quad 2.28$$

Or in terms of the transport mean free path of BR&S [51]

$$< \theta^2 >= \frac{z}{2\lambda_{tr}} \quad 2.29$$

Equation 2.26 is therefore the Bessel transform of a Gaussian function with a variance of $< \theta^2 >$ in terms of a reciprocal multiple scattering angle η. For the region where χ is greater than χ_g and $q(\chi) = 1$, Bethe equation (13)

$$\int_{\chi_g}^{\infty} d\chi\chi^{-3}[1-J_0(\chi\eta)] = \eta^2 \int_{\chi_g\eta}^{\infty} dt\, t^{-3}[1-J_0(t)] = \frac{1}{4}\eta^2 I_1(\chi_g\eta) \qquad 2.30$$

To solve I_1 Bethe takes by parts twice and uses the identity $\int tJ_0(t)dt = tJ_1(t)$. Taking $x = k\eta$ produces Bethe equation (14)

$$I_1 = 4\int_x^{\infty} \frac{dt}{t^{-3}}[1-J_0(t)] = \frac{2}{x^2}[1-J_0(x)] + \frac{J_1(x)}{x} + \int_x^{\infty} \frac{dt}{t} J_0(t) = 1 - \ln x + \ln 2 - C + O(x^2) \qquad 2.31$$

Where $C = 0.577$ is Euler's constant. I_1 diverges logarithmically at second order.

Molière, therefore, defines a parameter b in terms of B by taking Molière equation II(1, 5) and Bethe equation (16)

$$b = \log\left(\frac{\chi_c^2}{\chi'^2_a}\right) = \lim_{\chi_g\to\infty}\left[\log\left(\frac{\chi_g^2}{\chi_a^2}\right) - 1 + \log\left(\frac{\gamma^2\chi_g^2}{e^2\chi_a^2}\right)\right] \qquad 2.32$$

Where $\log\gamma = C$. Putting equations 2.23, 2.26 and 2.32 together Bethe obtains equation (17)

$$g(\eta, z) = exp\left(\tfrac{1}{2}(\chi_c\eta)^2[-\ln(\chi_a\eta) + \tfrac{1}{2} + \ln 2 - C]\right) \qquad 2.33$$

taking $y = \chi_c\eta,\ \lambda = \theta/\chi_c$ Bethe equation (2) and Molière equation II(5, 5) obtain

$$f(\theta)\theta d\theta = \lambda d\lambda \int_0^{\infty} ydyJ_0(\lambda y)\exp\left(\frac{1}{4}y^2\left(-b + ln\left(\frac{1}{4}y^2\right)\right)\right) \qquad 2.34$$

Where the upper limit of $d\eta$ should be evaluated at $\sim\chi_c$ with minimal loss of accuracy to avoid the integral diverging.

Bethe equation (22) or Molière II(1,6) and (1,7) which is $b = \log\left(\frac{\chi_c^2}{\chi'^2_a}\right)$, is used to find Molière equation (7,1) or Bethe equation (23), the transcendental equation

$$b = B - \log B \qquad 2.35$$

Resulting in B that varies between 5 and 20. Equation 2.34 can be expanded in terms of B and $\vartheta = \frac{\theta}{\chi_c\sqrt{B-1.2}}$ to get Molière (A,1) to (D,13) or Bethe equation (25), (26) and (27)

$$f(\theta)\theta d\theta = \vartheta d\vartheta\left[f^{(0)}(\vartheta) + B^{-1}f^{(1)}(\vartheta) + B^{-2}f^{(2)}(\vartheta) + \cdots\right] \quad 2.36$$

$$f^{(n)}(\vartheta) = n!^{-1}\int_0^\infty u du J_0(\vartheta u) \times \exp\left(-\frac{1}{4}u^2\right)\left[\frac{1}{4}u^2\ln\left(\frac{1}{4}u^2\right)\right]^n \quad 2.37$$

$$f^{(0)} = 2e^{\vartheta^2} = 2e^{\frac{\theta^2}{\chi_c^2(B-1.2)}} \quad 2.38$$

Equation 2.38 is the Gaussian approximation in Molière theory, with higher order $f^{(n)}$ becoming important at larger angles. Equation 2.38 has Hanson's change $B - 1.2$. Equation 2.17 can also be obtained from Goudsmidt and Saunderson's formula [59, 73, 76]

$$f(\theta, z) = \sum_{i=1}^{\infty}\left(l + \frac{1}{2}\right)P_l(\theta) \times \exp\left\{-z\int \sigma(\chi)\chi\, sin\,\chi d\chi[1 - P_l(\chi)]\right\} \quad 2.39$$

Where the exponential in equation 2.39 is g_l or Goudsmidt and Saunderson's equation (13). From Bethe's equation (40) and Goudsmidt and Saunderson's footnote 4, Bethe takes the transformation, valid for small χ

$$P_l(\chi) = J_0\left(\left(l + \frac{1}{2}\right)\chi\right) \quad 2.40$$

Then replaces $\left(l + \frac{1}{2}\right)$ with η and replace the sum over η with an integral. Since χ is small, $\sin\chi \to \chi$. g_l becomes $g(\eta, z)$ (equation 2.16 or Bethe equation (3)). The result is equation 2.17.

An approximation to Molière's solution has been offered by Highland.[50, 77-79] Highland equations (4) and (2) define the root mean squared scattering angle θ_0 in terms of equation 1.32

$$\theta_0 = \frac{E_s}{pv}\sqrt{\frac{z}{X_0}}f_{High} \tag{2.41}$$

Where

$$E_s = \sqrt{\frac{2\pi}{\alpha}}m_e c^2 = 15\ Mev \tag{2.42}$$

$$f_{High} = \left[1 + \frac{1}{9}log10\left(\frac{z}{X_0}\right)\right] \tag{2.43}$$

Highland found that the values of E_s such that θ_0 fits Molière theory depended on the atomic weight of the material as well as the total depth in the target. He, therefore, introduced equation 2.43 as a correction factor. Gottschalk (2010) equation (13) extended Highland's fit to thick targets by integrating over $pv(z)$ as determined by equation 1.15

$$\theta_{Highland} = f_{High}\sqrt{\int_0^z \left(\frac{14.1\ MeV}{pv(z)}\right)^2 \frac{1}{X_0}dz} \tag{2.44}$$

Where the empirical change $E_s = 14.1\ MeV$ has been made.[42, 78]. Gottschalk's "Generalized Highland Approximation" is available in the form of a digital lookup table called BGWARE.[80]. Gottschalk equation (40) replaces the radiation length X_0 (equation 1.16) with the parameter X_s in equation 2.41 that use improved screening lengths that better reflect the nuclear (equation 1.37) and atomic radii. Rather than integrate over $pv(z)$ he fits θ_0 to Molière's gaussian solution with Hanson's corrections using a polynomial and obtains

$$f_{dM} = 0.5244 + 0.1975\log\left(1 - \left(\frac{pv}{p_1 v_1}\right)^2\right)$$
$$+0.2320\log(pv) - 0.0098\log(pv)\log\left(1 - \left(\frac{pv}{p_1 v_1}\right)^2\right) \tag{2.45}$$

So that equation 2.45 replaces equation 2.43.

As with Highland's correction factor, Molière's B parameter is a function of the total depth of the material as it is calculated from equation (2.35) which is a function of $\log(\chi_c^2)$. Hanson's empirical correction to $\sqrt{B} \rightarrow \sqrt{B - 1.2}$ is fixed for all depths, which is an additional non-local factor. The evolution of the phase space of the beam at each depth in Molière theory and Highland's approximation, therefore, depends on their interactions throughout the total depth of the material, rather than their single scattering interactions at each depth. This makes them non-local in the sense that they do not depend solely on the phase space evolution as described by the transport equation. In a compound Poisson process, the interaction between events is statistically independent, and the phase space evolution occurs independently in each layer as governed by the single scattering cross section. Ideally, the phase space evolution of the proton beam would occur independently in each depth interval, evolving according to the single scattering cross section in that layer and reflected in the multiple scattering distribution.

Let us find a solution that depends solely on the phase space evolution of the beam in the transport equation by solving equation 2.17 numerically using Molière's implicit cross section equation 2.21. In principle, this will describe the evolution of the phase space of the beam purely in terms of the number of elastic scattering events at each depth interval as determined by the single scattering cross section in that interval.

Numeric solution to Molière theory in the small angle approximation

Equation 2.17 may be solved numerically and is valid for a single thin layer where the energy loss is not too great. For thicker targets, we take the convolution of $f(\theta, dz)$ over the depth z, where dz is the thickness of a single depth interval. $i =$

1,2,3 ... is the index of the depth interval with n intervals and $\sigma_i(\chi)$ is the cross section (along with pv, β^2 and χ_a) at depth interval i.

$$f_1(\theta, dz) * f_2(\theta, dz) * f_3(\theta, dz) \quad 2.46$$

Applying the folding theorem to equation (2.46)

$$\prod_i g_i(\eta, dz) = g_1(\eta, dz) \times g_2(\eta, dz) \times g_3(\eta, dz) \quad 2.47$$

Next, we multiply over $g_i(\eta, z)$ by summing over the argument of the exponents.

$$\prod_i g_i(\eta, dz) = \exp\left[-\sum_{i=1} dz_i \int_0^\infty \sigma_i(\chi)\chi d\chi(1 - J_0(\eta\chi))\right] \quad 2.48$$

So that the scattering PDF for a homogenous material is

$$f(\theta, z) = \int_0^\infty \eta d\eta J_0(\eta\theta) \exp\left[-\sum_{i=1}^{n} dz_i \int_0^\infty \sigma_i(\chi)\chi d\chi(1 - J_0(\eta\chi))\right] \quad 2.49$$

In cases where the depth intervals are composed of different materials, we break up the sum

$$\sum_{i=1}^{n} \rightarrow \sum_{i=1}^{n} + \sum_{j=n+1}^{k} \quad 2.50$$

Where n and k are indexes of depth intervals of the first material and second material, respectively. Here, the number of elastic scattering events is determined solely by the interactions in each depth interval as described by $\sigma(\chi)$. Because the scattering events are statistically independent the order of the summation doesn't matter.

To account for an initial beam divergence characteristic of a real accelerator, we assume a Gaussian distribution of the divergence where $\frac{\sigma}{2.355}$ is the full width at half maximum of the divergence σ. We can write down

$$f(\theta) = \frac{1}{2\sigma^2}\exp\left[-\frac{1}{2}\left(\frac{\theta^2}{\sigma^2}\right)\right] \quad 2.51$$

Inserting equation (24) into equation (12)

$$g_{div}(\eta, z) = \int_0^\infty \theta d\theta J_0(\eta\theta)\frac{1}{2\sigma^2}\exp\left[-\frac{1}{2}\left(\frac{\theta^2}{\sigma^2}\right)\right] = \exp\left[-\frac{1}{2}(\eta^2\sigma^2)\right] \quad 2.52$$

So that the convolution of the beam divergence with $\prod_i g_i(\eta, z)$ is

$$g_{div}(\eta, z) \times \prod_i g_i(\eta, z) \quad 2.53$$

And equation (2.49) becomes

$$f(\theta, z) = \int_0^\infty \eta d\eta J_0(\eta\theta)\exp\left[-\frac{1}{2}(\eta^2\sigma^2) - \sum_{i=1}^{n} dz_i \int_0^\infty \sigma_i(\chi)\chi d\chi(1 - J_0(\eta\chi))\right] \quad 2.54$$

Numeric solution to Molière using the full cross section

For the complete cross section that is not in the small angle approximation, we take equation 2.10 for $\sigma(\chi)$. Expressed in terms of Molière's parameter $q(\chi)$

$$q(\chi) = \frac{\chi^4}{\left(4\sin^2\frac{\chi}{2} + \chi_a^2\right)^2} \quad 2.55$$

We replace the transform of equation 2.40 with Bethe equation (56) and Molière equation (A,1) for large angles[59, 72]

$$P(\chi) = \sqrt{\frac{\chi}{\sin\chi}}\, J_0\left(\left(l + \frac{1}{2}\right)\chi\right) \quad 2.56$$

As we are no longer in the small angle approximation, we replace χ with $\sin\chi$ in equation 2.39 so that g_l becomes

$$g(\eta,z)=\exp\left[-\sum_{i=1}^{n}dz_i\int_0^{\infty}\sigma_i(\chi)\sqrt{\chi\sin\chi}\,d\chi(1-J_0(\eta\chi))\right] \qquad 2.57$$

Equation 2.57 is the exponent of the sum of the effective number of elastic scattering events in each depth interval dz_i according to the complete differential scattering cross section. From Bethe equation (58) one can take $f(\theta,z)\rightarrow f(\theta,z)\sqrt{\theta/\sin\theta}\,d\theta$ and the result is

$$f(\theta,z)=\sqrt{\frac{\theta}{\sin\theta}}\,d\theta\int_0^{\infty}\eta d\eta J_0(\eta\theta)$$
$$\times\exp\left[-\sum_{i=1}^{n}dz_i\int_0^{\infty}\sigma_i(\chi)\sqrt{\chi\sin\chi}\,d\chi(1-J_0(\eta\chi))\right] \qquad 2.58$$

Convolution with an initial Gaussian beam divergence (equation 2.51) gives

$$f(\theta,z)=\sqrt{\frac{\theta}{\sin\theta}}\,d\theta\int_0^{\infty}\eta d\eta J_0(\eta\theta)$$
$$\times\exp\left[-\frac{1}{2}(\eta^2\sigma^2)-\sum_{i=1}^{n}dz_i\int_0^{\infty}\sigma_i(\chi)\sqrt{\chi\sin\chi}\,d\chi(1-J_0(\eta\chi))\right] \qquad 2.59$$

Comparison with FLUKA Monte Carlo

FLUKA[37-39, 45-47] is a particle scattering Monte Carlo code produced as a collaboration between The European Council for Nuclear Research (CERN) in Switzerland and The National Institute for Nuclear Physics (INFN) in Italy. FLUKA's multiple elastic scattering model uses Molière's approximation of equation 2.23 in terms of $f^{(0)},f^{(1)},f^{(2)}$ (with the substitution $\theta\approx\sqrt{\sin\theta\,/\theta}$). In the single scattering region it

uses a correction factor to the small angle approximation so that the large angle distribution goes over into the full scattering cross section rather than the small angle.

In Figures 2.1 to 2.12 FLUKA was run with a pristine beam (with no angular divergence) normally incident on different phantoms, each composed of different materials. The geometry used in FLUKA for Figures 2.13b and 2.13c is illustrated in Figure 2.13a. For all figures, EMFCUT, IONFLUCT, THRESHOL, and STEPSIZE cards were used and where physics was disabled, it was disabled by setting the threshold above the initial beam energy (to 1 GeV). Using EMFCUT, the transport of secondary electrons and gammas was disabled. IONFLUCT was used to disable energy straggling of hadrons and electrons/positrons. THRESHOL was used to disable hadronic elastic and inelastic scattering of protons. The range of the energy loss STEPSIZE was from $[10^{-6}, 10^{-1}]$ cm. Scoring was performed with the USRYIELD setting measuring proton fluence with respect to lab angle and lab kinetic energy. A 230 MeV proton energy was chosen because it allows the broadest choice of depths.

Setting depth interval size

We have taken the depth interval size dz in equations 2.49, 2.54 and 2.58 to be the same across the total depth z. This isn't required but is done for simplicity. One expects that a small depth interval leads to a more accurate probability distribution than a large one. A small depth interval size leads to minimal additional computational overhead, so we have chosen the size such that a smaller interval achieves no benefit, depending on the material. An efficient algorithm would vary the depth interval size depending on the stopping power at each depth interval. Figures 2.1 and 2.2 show the effect of the depth interval size on the probability angle distribution using a range of sizes

in water and tungsten. It can be seen that for depth intervals of 5 cm in water, the probability distribution deviates somewhat from the distributions with finer depth interval sizes. Figure 2.1 shows that equation 2.49 calculated with depth intervals of 0.1 cm (green dot-dash line) and 0.01 cm (blue dot-dash line) are indistinguishable. A depth interval in water for dz of 0.01 cm has thus been used for comparisons against FLUKA. Figure 2.2 shows equation 2.49 for tungsten with some small difference in the distribution between depth intervals of 0.5 cm and 0.01 cm. For tungsten, a depth interval of 0.001 cm (10 microns) has therefore been used. For other materials, the depth interval size has been chosen similarly.

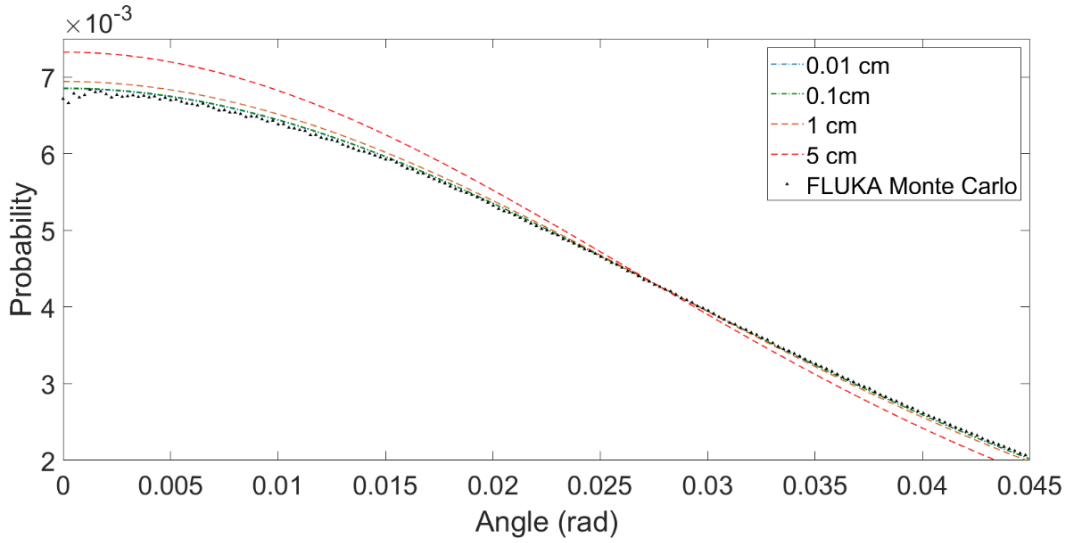

Figure 2.1. Depth interval comparison in water. Probability distribution vs angle for 230 MeV proton beam in water at 20cm depth. The colored lines are equation 2.49 with the depth interval dz as listed in the legend. The probabilities are normalized such that they individually sum to 1 over [0,0.25] rad. Linear scale in y.

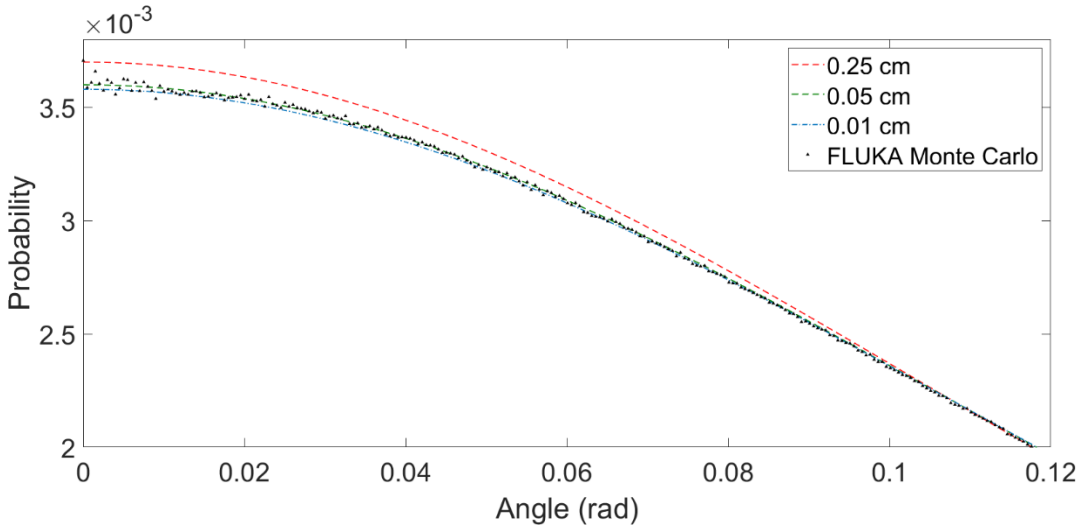

Figure 2.2. Depth interval comparison in tungsten. Probability distribution vs angle for 230 MeV proton beam in tungsten at 2cm depth. The colored lines are equation 2.49 with the depth interval dz as listed in the legend. The probability distributions are normalized such that they individually sum to 1 over [0,0.5] rad. Linear scale in y.

Interpolation for speed

To generate plots of equations 2.49, 2.58 and 2.59, tables containing $g(\eta, z)$ for various materials and energies were prepared so that the code only needed to look up the proper $g(\eta, z)$. This was interpolated for different values of η using a spline function, and $g(\eta, z)$ was Bessel transformed into the scattering probability at angle θ.

Behavior at large angles

At large angles, Molière theory "naturally" goes over into the single scattering cross section. To plot the single scattering probabilities for thick targets where pv changes with depth we take the sum of $N\sigma(\chi)$ over dz so that

$$zN\sigma(\chi) = dz\sum_{i=1}^{n} N\sigma_i(\chi) \qquad 2.60$$

Equation 2.60 is used to calculate equation 2.11 and equation 2.10 in Figures 2.3 and 2.4 with the same depth interval dz as described above with equation 2.49. In Figure 2.3 it can be seen that as the number of scattering events in the distribution decreases at small angles, the multiple scattering distribution, equation 2.49 converges on single scattering cross sections equation 2.11.

In Figures 2.4a, 2.4b and 2.5 it can be seen that irrespective of whether they are in the small angle, equations 2.49 and 2.58 follow each other closely until they reach the region of single scattering, when they converge on equations 2.11 and 2.10, respectively. The single scattering region is approximately 6 orders of magnitude smaller than the peak of the multiple scattering region, placing it outside the region of clinical significance for a single fractionated beam.[81]

Plot normalization

Figures 2.6 through 2.13 show comparisons with FLUKA Monte Carlo of probability distributions vs angle in various depths and materials. Each probability distribution is normalized such that its total probability sums to 1.

Behavior in the small angle region

It can be seen in Figures 2.6a, 2.7a, 2.8a, 2.9a and 2.10a that equations 2.49 and 2.58 show slight differences at small angles, with equation 2.58 followed FLUKA more closely. This is not surprising since FLUKA also makes the change $\theta \rightarrow \sqrt{\sin\theta\,/\theta}$ from Bethe equation (56-57).[47] Due to the normalization of the total probability to 1 across each probability distribution, the deviation between equations 2.49, 2.58 and FLUKA Monte Carlo represents accumulated differences.

General agreement with FLUKA in different materials

Figures 2.6b,c 2.7b,c 2.8b,c 2.9b,c 2.10b,c 2.11, and 2.12 show Equation equation 2.58 for graphite, water, aluminum, iron, tungsten and lead which are in agreement with FLUKA Monte Carlo. At depths near the end of the range, the calculated probability is higher than with FLUKA. The very dense materials; tungsten and lead also show some deviation.

Calculation of probability distribution in a beamline

A simplified beamline for 230 MeV protons is illustrated in Figure 2.13a. It is composed of a beam nozzle with a 100 mrad, 50 mrad or 0 gaussian divergence with a 1 cm scatterer, a 10 cm nitrogen gap, and a 5cm water target. Figures 2.13b and 2.13b show probability vs angle distributions that are in agreement with FLUKA Monte Carlo for all three divergences.

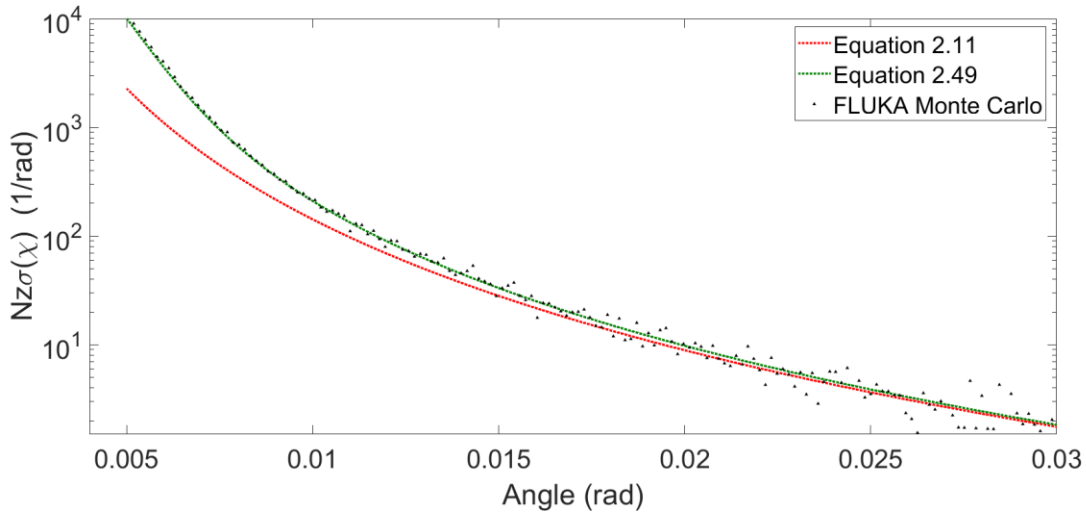

Figure 2.3. Behavior at large angles 1. Probability vs angle for 230 MeV proton beam at 2mm depth in water. Log scale in y.

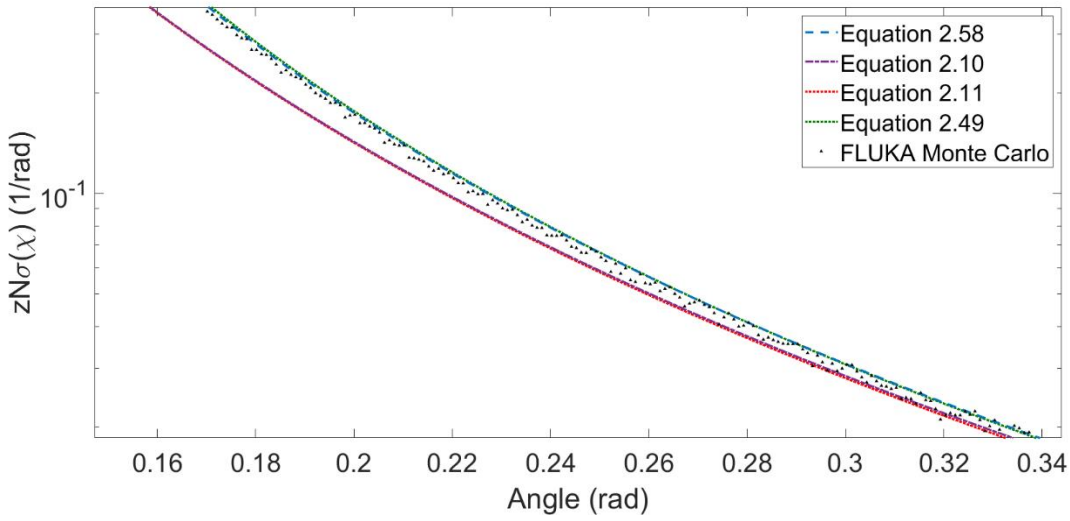

Figure 2.4a. Behavior at large angles 2. Probability vs angle for 230 MeV proton beam at 20cm depth in water. Log scale in y.

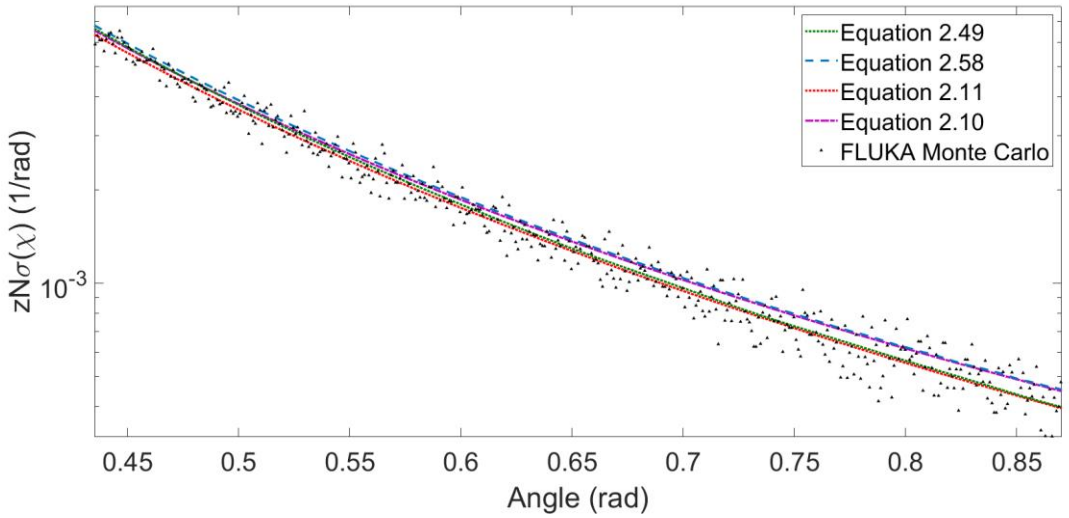

Figure 2.4b. Behavior at large angles 3. Probability vs angle for 230 MeV proton beam at 20cm depth in water. Log scale in y.

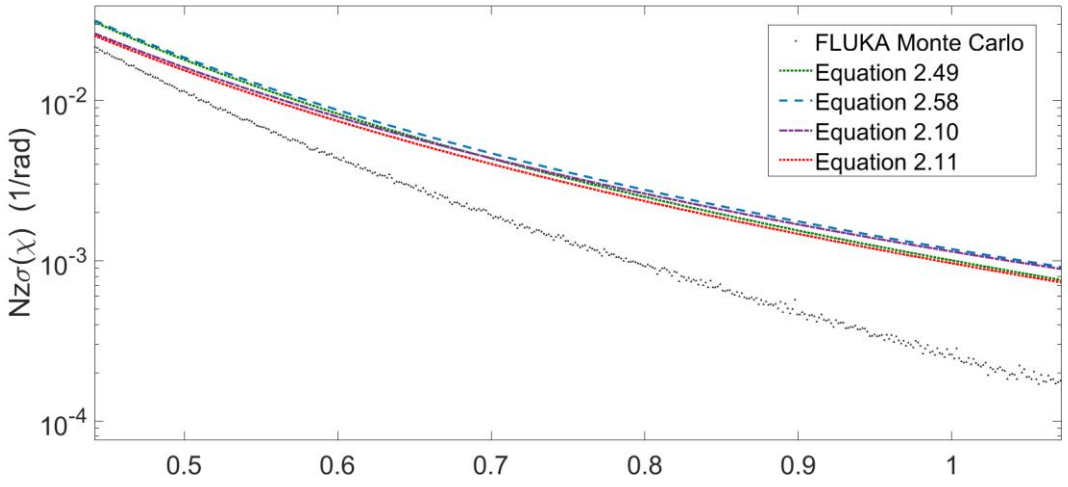

Figure 2.5. Behavior at large angles 4. Probability vs angle for 230 MeV proton beam at 32cm depth in water. Log scale in y.

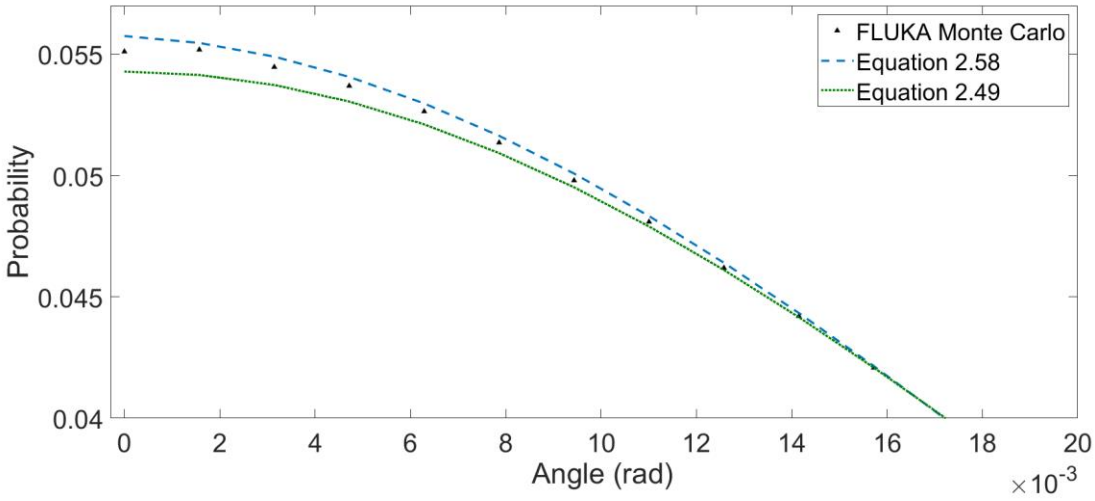

Figure 2.6a. Angle PDF in Graphite 1. 230 MeV proton beam PDF at 10 cm depth in graphite. Linear scale in y.

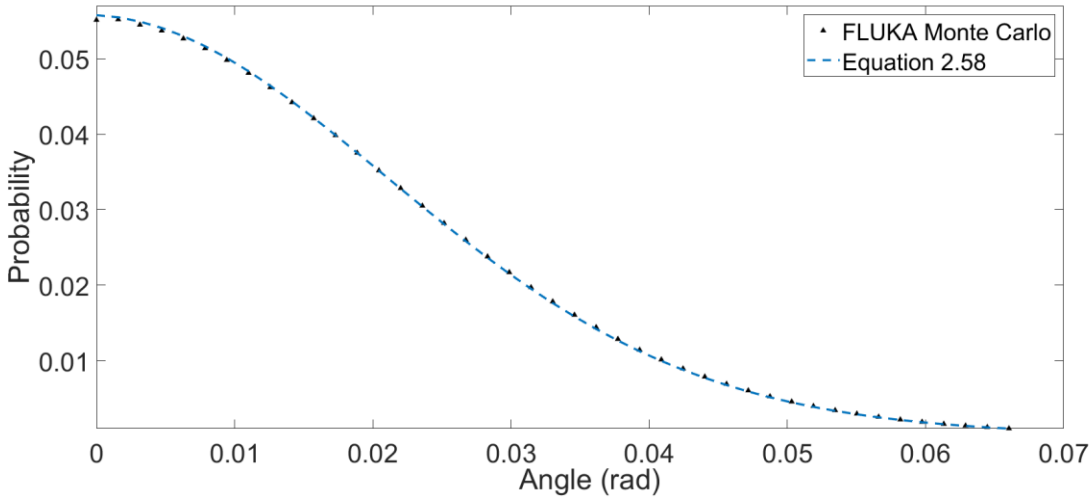

Figure 2.6b. Angle PDF in Graphite 2. 230 MeV proton beam PDF at 10 cm depth in graphite. Linear scale in y.

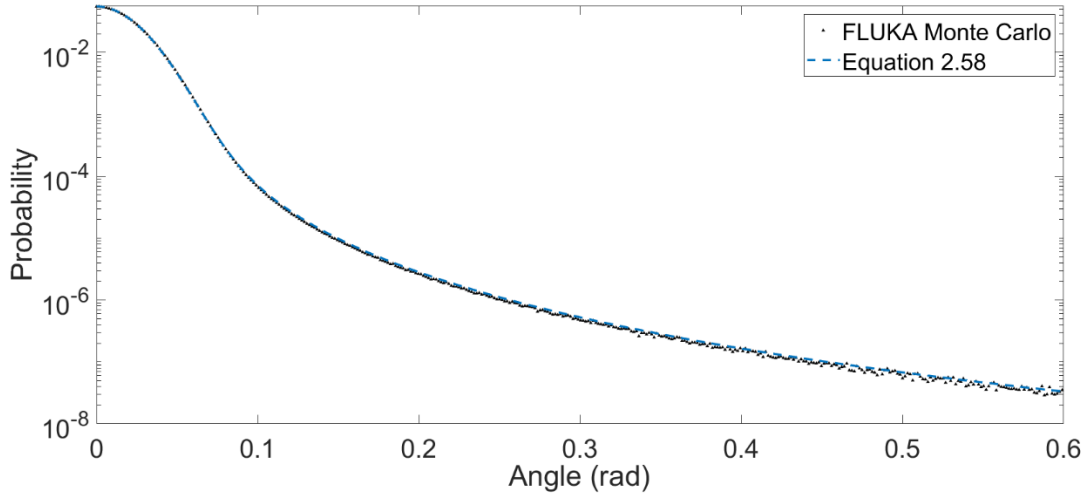

Figure 2.6c. Angle PDF in Graphite 3. 230 MeV proton beam PDF at 10 cm depth in graphite. Log scale in y.

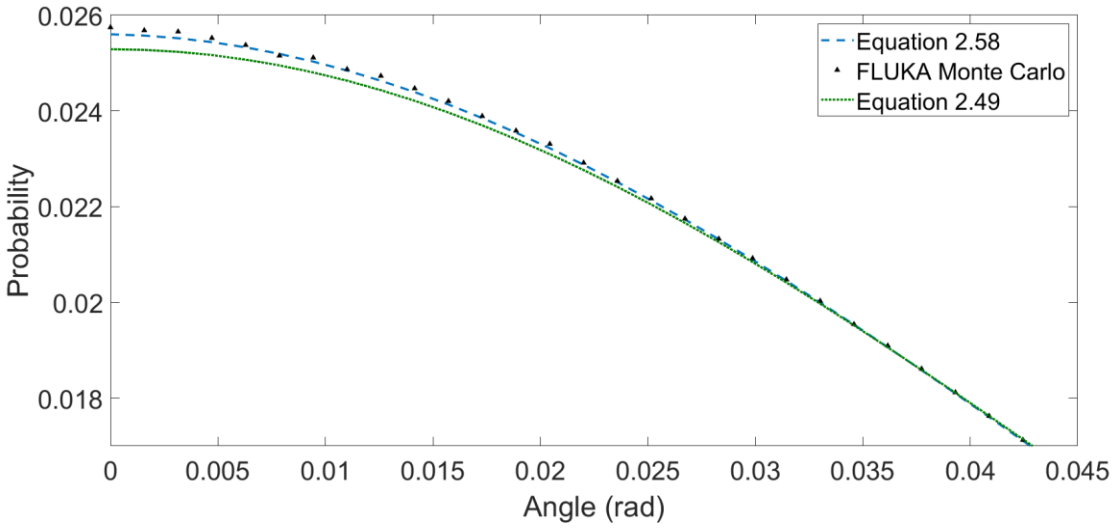

Figure 2.7a. Angle PDF in Graphite 4. 230 MeV proton beam PDF at 20 cm depth in graphite. Linear scale in y.

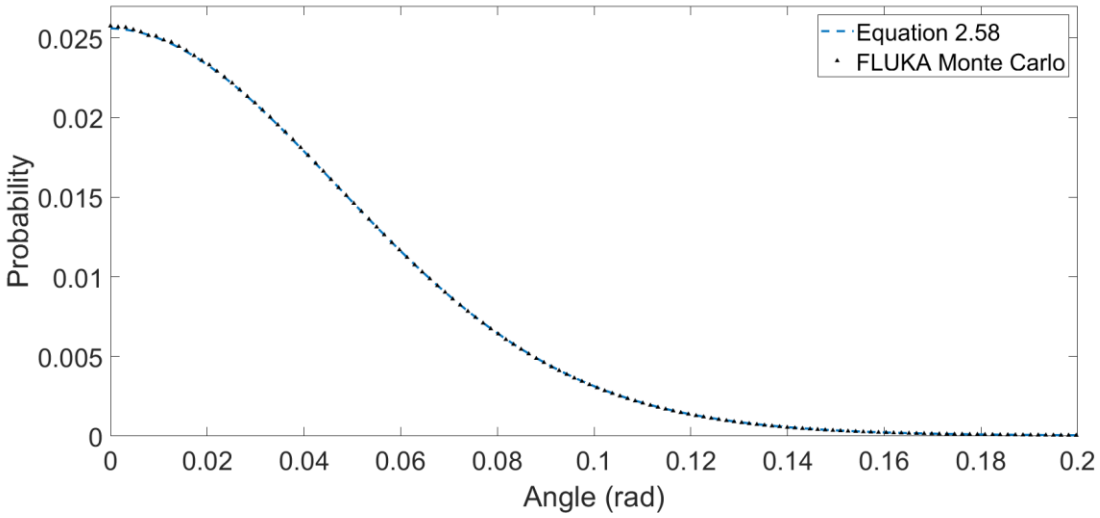

Figure 2.7b. Angle PDF in Graphite 5. 230 MeV proton beam PDF at 20 cm depth in graphite. Linear scale in y.

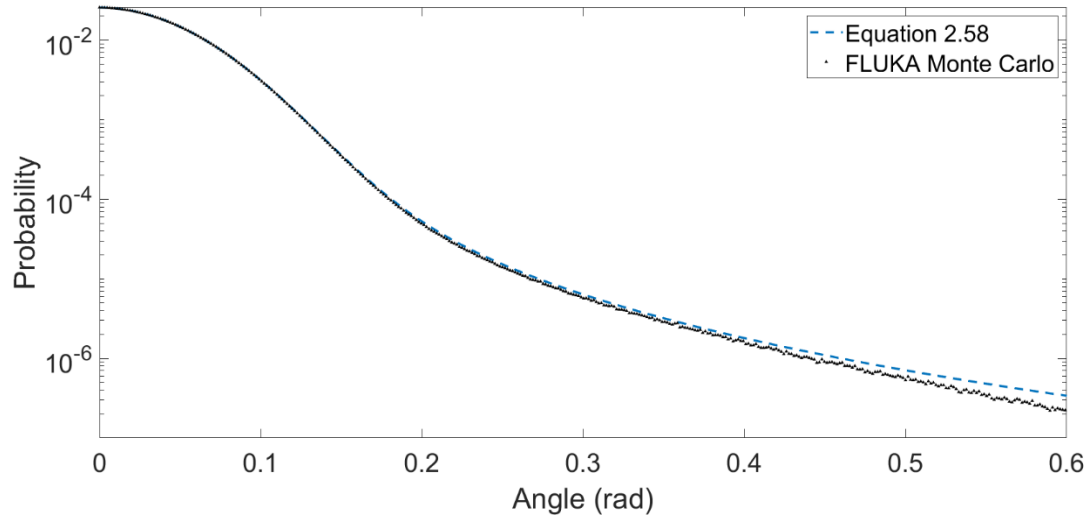

Figure 2.7c. Angle PDF in Graphite 6. 230 MeV proton beam PDF at 20 cm depth in graphite. Log scale in y.

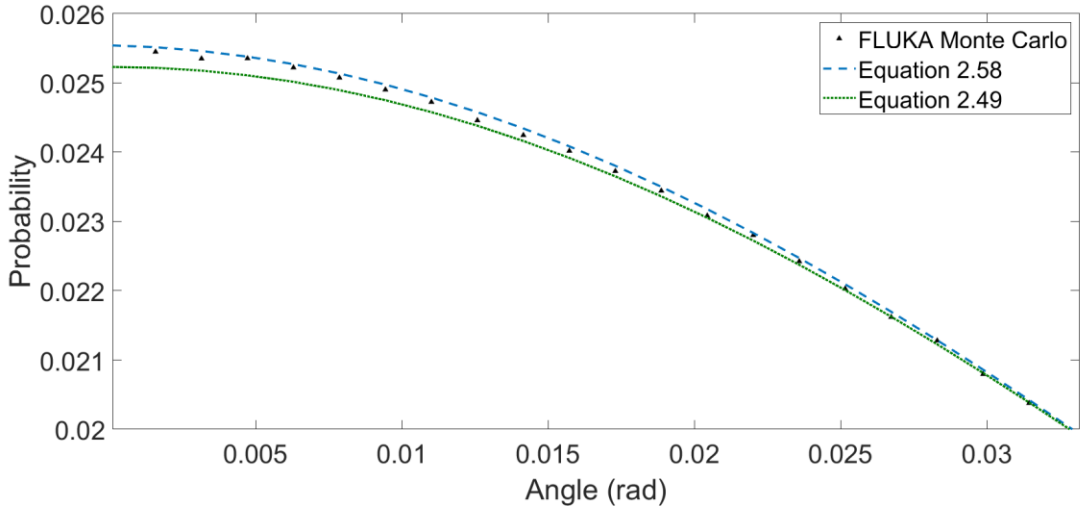

Figure 2.8a. Angle PDF in Water 1. 230 MeV proton beam PDF at 30 cm depth in water. Linear scale in y.

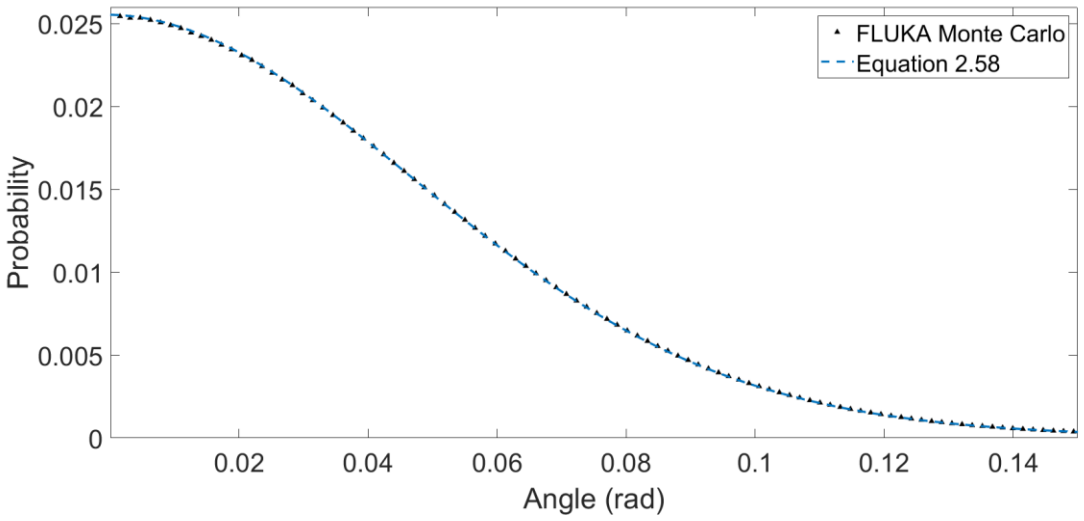

Figure 2.8b. Angle PDF in Water 2. 230 MeV proton beam PDF at 30 cm depth in water. Linear scale in y.

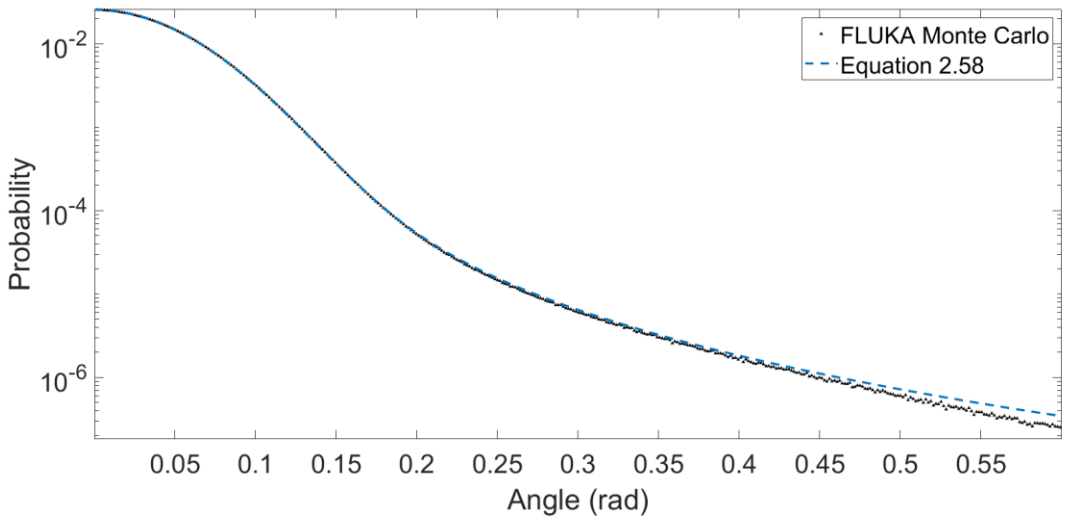

Figure 2.8c. Angle PDF in Water 3. 230 MeV proton beam PDF at 30 cm depth in water. Log scale in y.

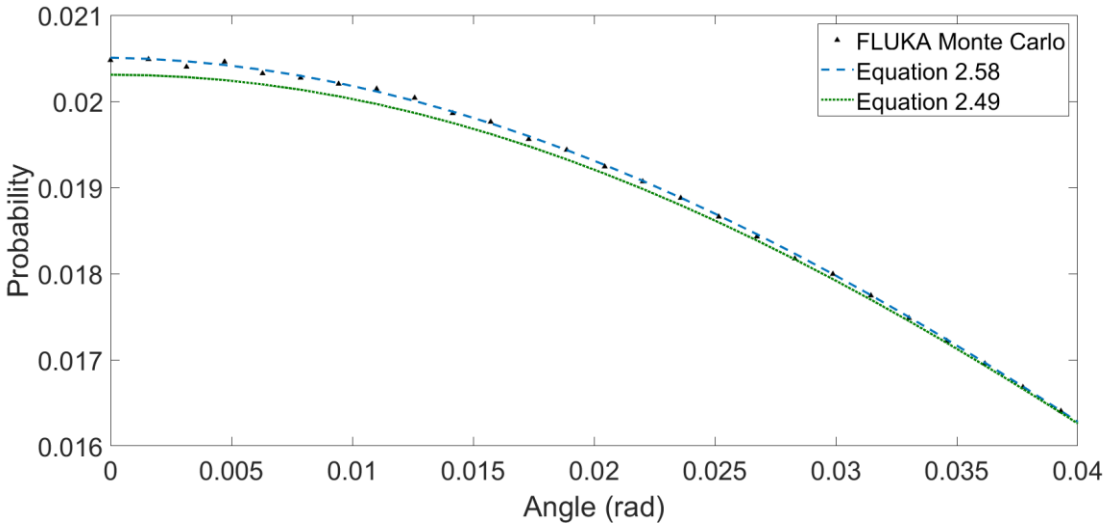

Figure 2.9a. Angle PDF in Aluminum 1. 230 MeV proton beam PDF at 13 cm depth in aluminum. Linear scale in y.

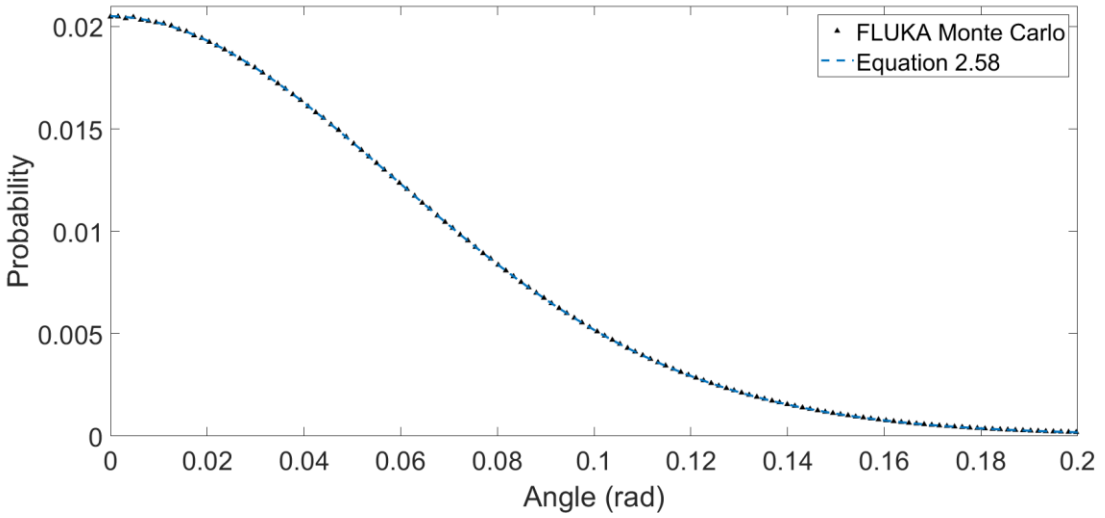

Figure 2.9b. Angle PDF in Aluminum 2. 230 MeV proton beam PDF at 13 cm depth in aluminum. Linear scale in y.

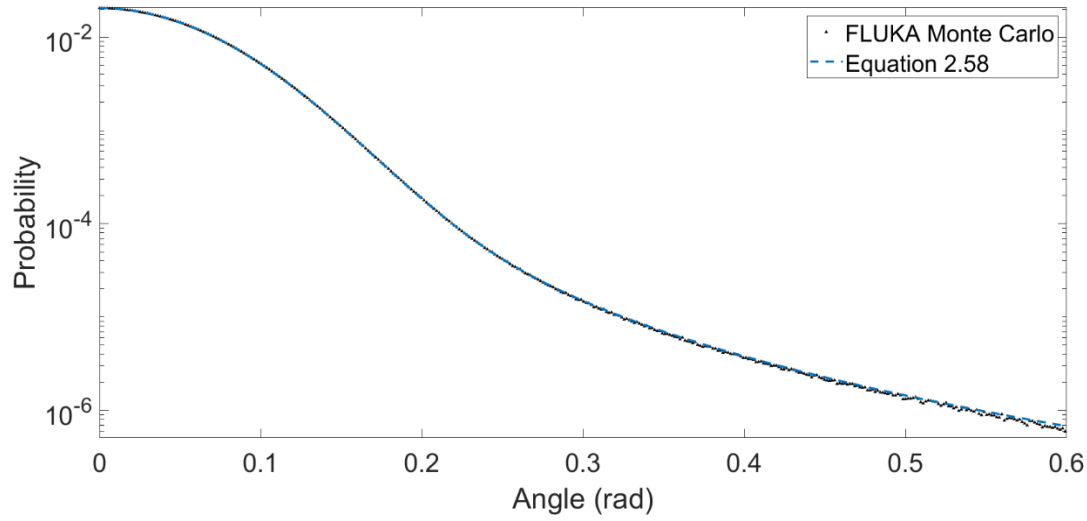

Figure 2.9c. Angle PDF in Aluminum 3. 230 MeV proton beam PDF at 13 cm depth in aluminum. Log scale in y.

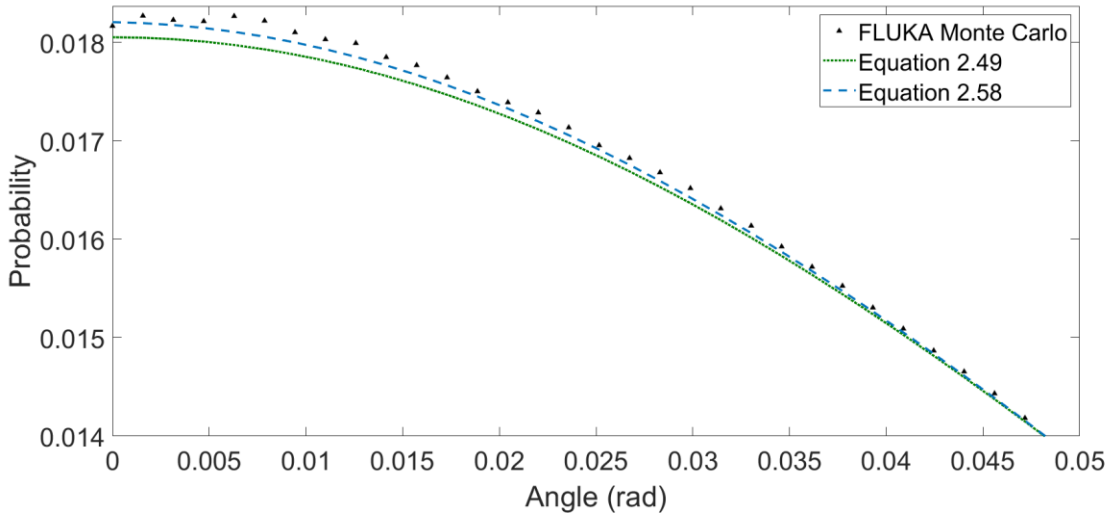

Figure 2.10a. Angle PDF in Iron 1. 230 MeV proton beam PDF at 4cm depth in iron. Linear scale in y.

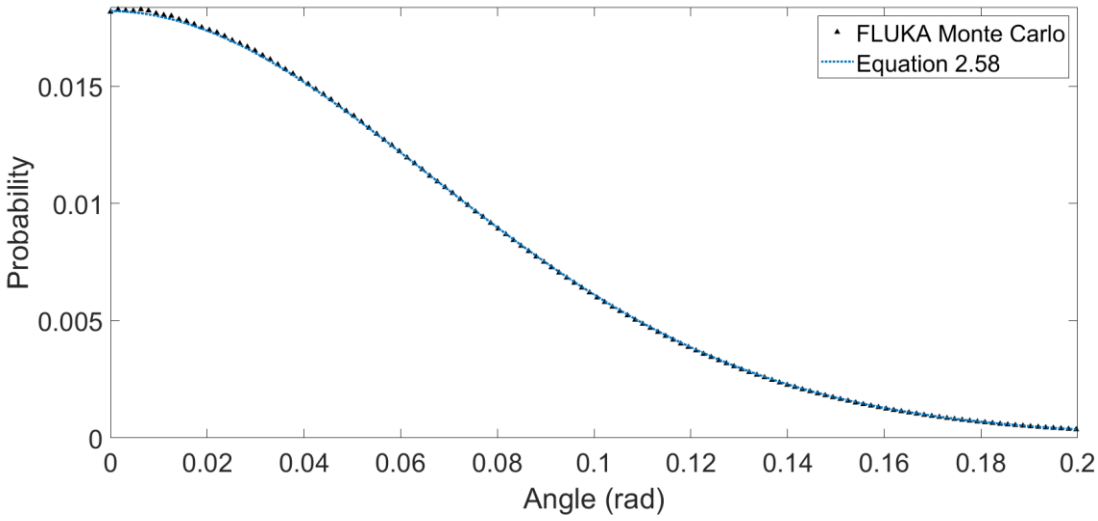

Figure 2.10b. Angle PDF in Iron 2. 230 MeV proton beam PDF at 4cm depth in iron. Linear scale in y.

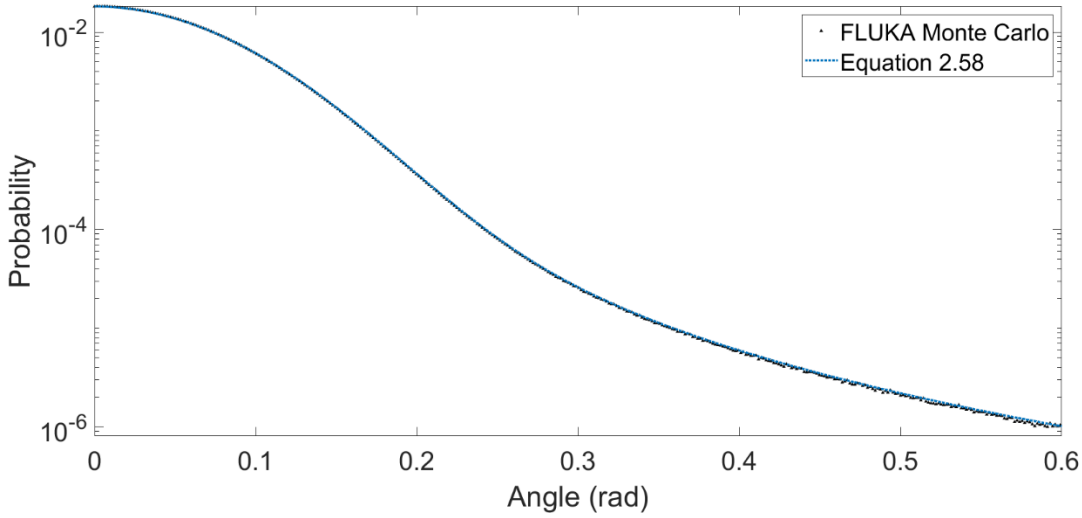

Figure 2.10c. Angle PDF in Iron 3. 230 MeV proton beam PDF at 4cm depth in iron. Log scale in y.

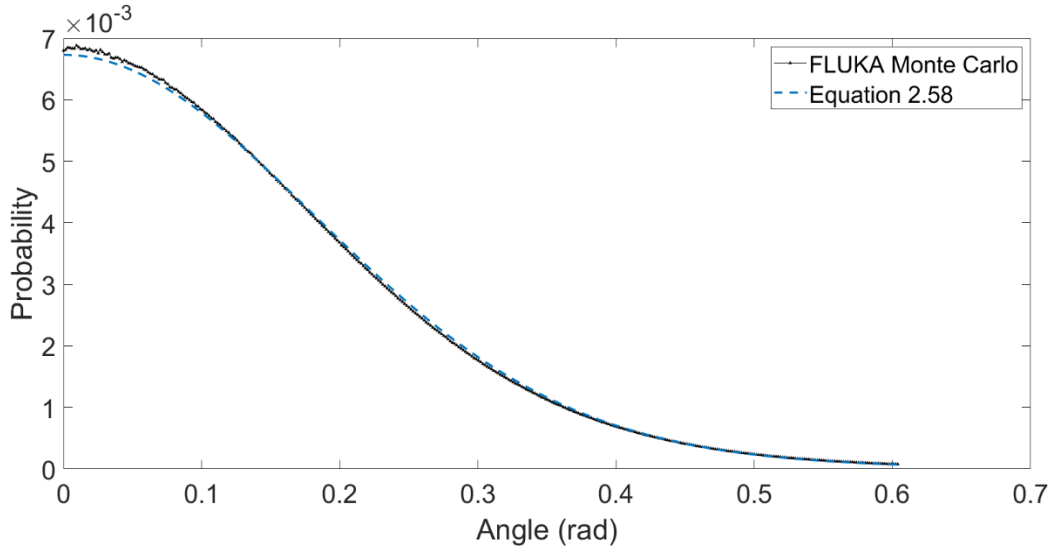

Figure 2.11. Angle PDF in Tungsten. 230 MeV proton beam PDF at 3cm depth in tungsten. Linear scale in y.

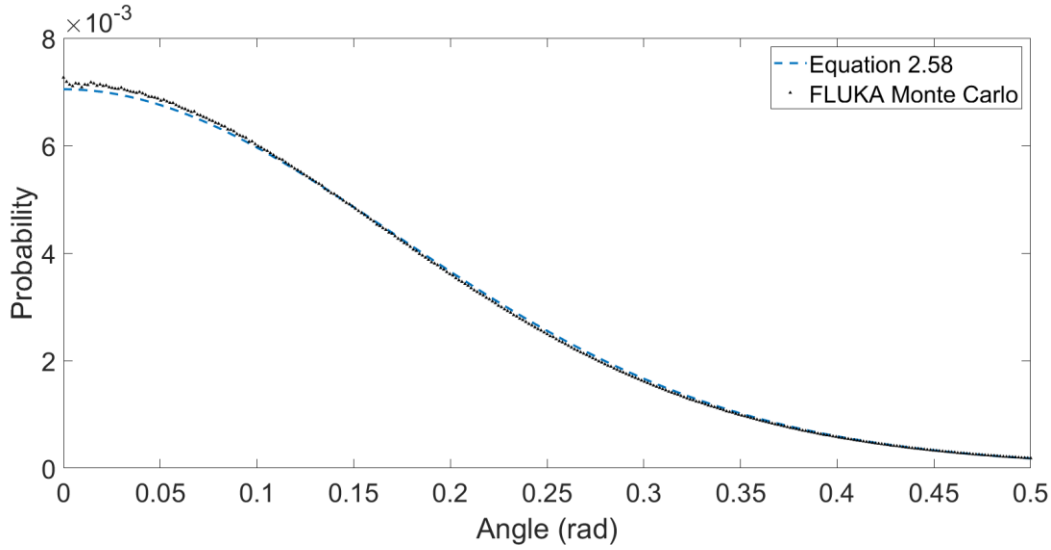

Figure 2.12a. Angle PDF in Lead 1. 230 MeV proton beam PDF at 5cm depth in lead. Linear scale in y.

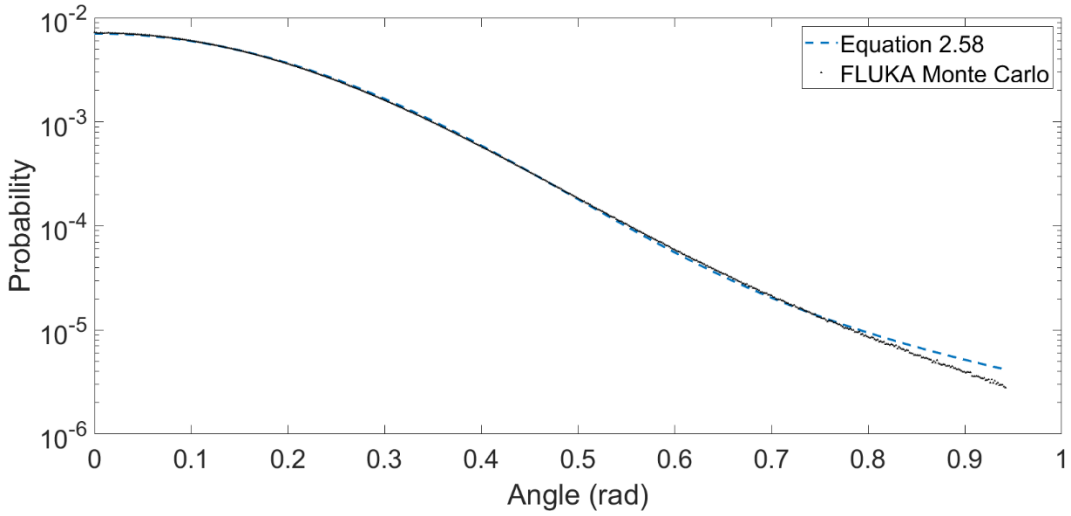

Figure 2.12b. Angle PDF in Lead 2. 230 MeV proton beam PDF at 5cm depth in lead.

Log scale in y.

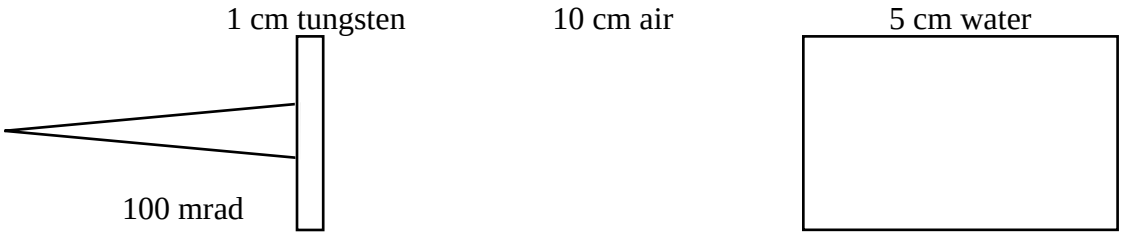

Figure 2.13a (above). Diagram of the simulated beamline.

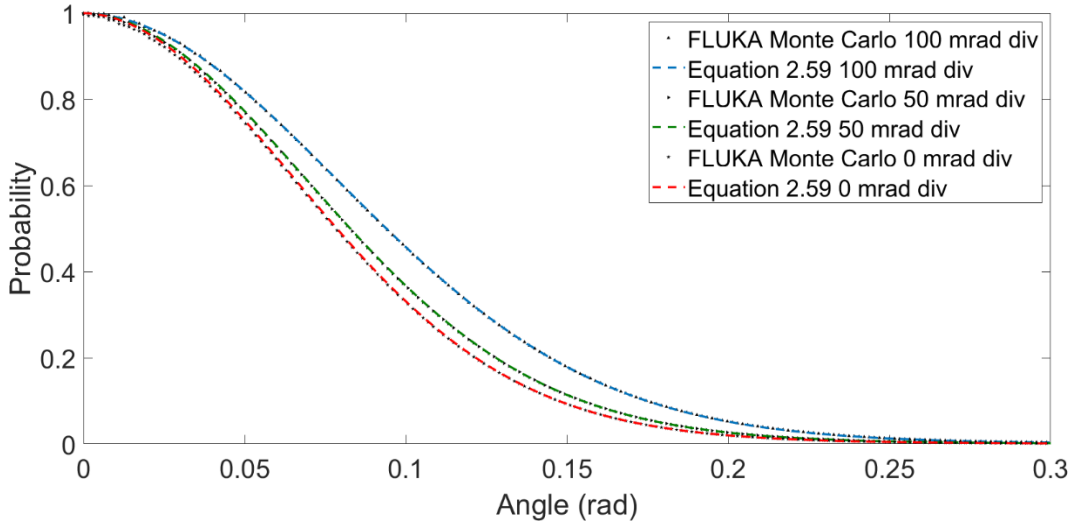

Figure 2.13b. Angle PDF after traversing simulated beamline 1. The proton beam has either 100, 50 or 0 mrad initial divergences. All pass through 1 cm of tungsten, 10 cm of nitrogen and 5 cm of water. Linear scale in y.

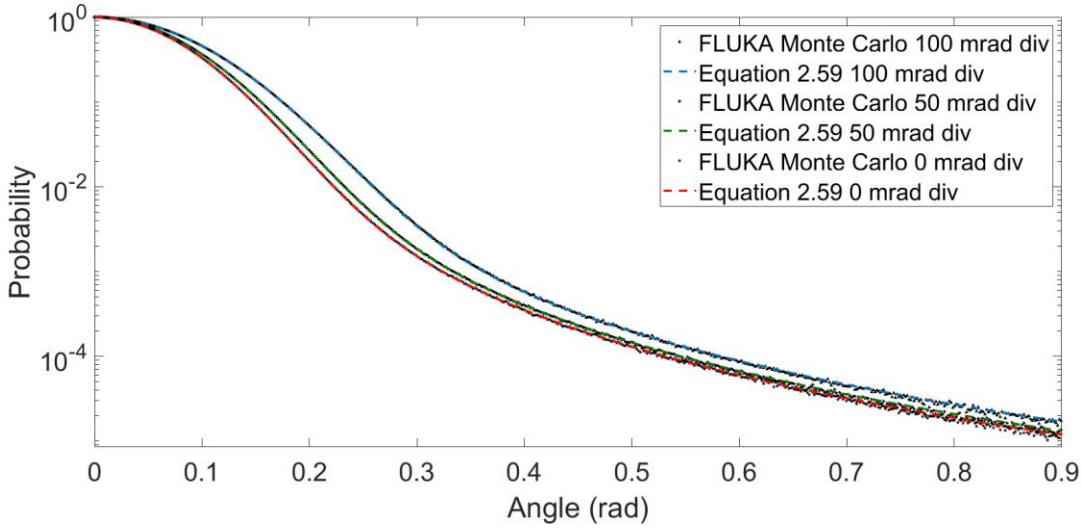

Figure 2.13c. Angle PDF after traversing simulated beamline 2. Proton beam has either 100, 50 or 0 mrad initial divergences. All pass through 1 cm of tungsten, 10 cm of nitrogen and 5 cm of water. Log scale in y.

Conclusion

The analytic solution to equation 2.17 in terms of the parameter B, including the $B - 1.2$ correction, is expressly non-local in that it requires knowledge of the proton history in prior pathlengths to determine the evolution of the beam along additional path lengths. This requirement also applies to the Highland Approximation and its extension to thicker targets.

However, the interactions of the proton beam in a target are a statistically independent Poisson process, as in the solution of Goudsmidt and Saunderson, and the transport equation describes the evolution of the phase space that is determined only by the single scattering cross section along a depth interval.

We have shown that a numerical solution to equations 2.49, 2.58 and 2.59 accurately describes the multiple scattering distribution in a variety of materials by relying only on the single scattering cross section in each depth interval. This is in accordance with the transport equation and the statistical independence of elastic scattering events. The multiple scattering distribution gradually gives over to the single scattering distribution as the number of elastic scattering events diminishes for larger multiple scattering angles. A convolution over the depth accurately contributes additional elastic scattering events as a function of the reciprocal scattering angle which broadens the multiple scattering region. Since the dynamics depend only on the interactions in each depth interval, the depth intervals may be composed of any material provided the single scattering cross sections can be determined. The elastic scattering events in a depth interval may be calculated in any order as per the sum in equation 2.50. An initial

Gaussian beam divergence may be included, as per equations 2.51 to 2.54, to better describe the protons from a realistic accelerator nozzle.

We have also shown that using the alternative Legendre to Bessel function transforms combined with the complete differential cross section the numerical solution (equation 2.58) may be extended beyond the small angle approximation. This solution accurately converges on the complete differential cross section at large angles as expected. It also accurately reproduces the small angle multiple scattering distributions produced by FLUKA slightly better than the distributions with equation 2.49. This is likely because the same transform used by equation 2.58 is used by the FLUKA code. The differences between equations 2.48 and 2.58 at large energy losses and large angles as compared to FLUKA may be due to long path lengths tracked by FLUKA at large angles in the simulation. The slight disagreement between equation 2.58 and FLUKA for tungsten and lead may be explained by deviations from the single scattering cross section equation 2.10 for those high-Z materials.

Although we have made all comparisons for protons, similar calculations for electrons should differ only in their energy loss and corresponding single scattering cross sections.

For use in a Monte Carlo code, different tables correspond to $g(\eta, z)$ for different thicknesses and materials can be stored, interpolated and transformed into $f(\theta, z)$ as needed.

CHAPTER 3

ENERGY LOSS DISTRIBUTIONS

Landau-Vavilov Theory

As energetic protons pass through matter, they collide with atomic electrons in the form of inelastic scattering. [44, 82, 83] As with elastic collisions, inelastic collisions are statistically independent and the number of collisions is Poisson distributed along a path length. Some collisions result in a greater energy loss than other collisions. The energy loss in a single collision is described by the probability $\omega(\epsilon)$ per unit length per energy loss ϵ to the recoil of the atomic electron, as given by the differential cross section.[43, 84, 85] Assuming no minimum or maximum energy loss, the total probability of an inelastic collision per unit length, or in the inverse inelastic mean free path is

$$\omega_{inel} = \frac{1}{\lambda_{in}} = \int_0^\infty \omega(\epsilon) d\epsilon \tag{3.1}$$

In the theory of Landau[86], the target is considered to not be very thick, such that the energy loss is small compared with the initial energy, and that $\omega(\epsilon)$ does not change too much over the depth z. The energy loss Δ after many collisions in the target is a stochastic parameter and the probability energy loss distribution $f(\Delta, \mathrm{z})$ can be determined by the kinetic equation for the distribution function or inelastic transport equation as given by Landau[86, 87]

$$\frac{\partial f(\Delta, \mathrm{z})}{\partial z} = \int_0^\infty \omega(\varepsilon)[f(\Delta - \varepsilon, z) - f(\Delta, z)]\, d\epsilon \tag{3.2}$$

Landau takes the Laplace transform of $f(\Delta, z)$

$$\varphi(p, z) = \int_0^\infty f(\Delta, \mathrm{z}) e^{-p\Delta} d\Delta \tag{3.3}$$

Then the inverse Laplace transform

$$f(\Delta, \mathrm{z}) = \frac{1}{2\pi i}\int_{-i\infty+\sigma}^{+i\infty+\sigma} e^{p\Delta}\varphi(p,z)dp \qquad 3.4$$

Multiplying by $e^{-p\Delta}$ and integrating over $d\Delta$

$$\frac{\partial\varphi(p,z)}{\partial x} = -\varphi(p,z)\int_0^\infty \omega(\epsilon)(1-e^{-pe})d\epsilon \qquad 3.5$$

Applying boundary conditions $f(\Delta,0) = \delta(\Delta)$ and $\varphi(p,0) = 1$ Landau gets

$$\varphi(p,z) = \exp\left[-z\int_0^\infty \omega(\epsilon)(1-e^{-pe})d\epsilon\right] \qquad 3.6$$

Inserting equation 3.6 into equation 3.4

$$f(\Delta, \mathrm{z}) = \frac{1}{2\pi i}\int_{-i\infty+\sigma}^{+i\infty+\sigma} e^{p\Delta - \mathrm{z}\int_0^\infty \omega(\epsilon)(1-e^{-p\epsilon})d\epsilon}dp \qquad 3.7$$

with $\omega(\epsilon)$ in terms of the electron density $\frac{Z\rho}{A}$ [84, 86, 87]

$$\omega(\epsilon) = \frac{2\pi N_A(\alpha\hbar c)^2}{m_e c^2}\frac{1}{\beta^2}\frac{Z\rho}{A}\frac{1}{\epsilon^2}\left(1-\frac{\epsilon\beta^2}{\epsilon_{max}}\right) = 0.1534\frac{1}{\beta^2}\frac{Z\rho}{A}\frac{1}{\epsilon^2}\left(1-\frac{\epsilon\beta^2}{\epsilon_{max}}\right) \qquad 3.8$$

Equation 3.8 is from the cross section of Livingston and Bethe.[84, 85] Equation 3.7 is Landau's general solution to the transport equation 3.2. After some parametrization, it reduces to

$$f(z,\Delta) = \frac{1}{\xi}\varphi(\lambda) \qquad 3.9$$

Where,

$$\xi = 0.1534\frac{1}{\beta^2}\frac{Z\rho}{A}z\ MeV \qquad 3.10$$

$\varphi(\lambda)$ is the universal function

$$\varphi(\lambda) = \frac{1}{2\pi i}\int_{-i\infty+\sigma}^{+i\infty+\sigma} e^{u\ln u+\lambda u}\, du \qquad 3.11$$

And, where C is Euler's constant 0.577….

$$\lambda = \frac{\Delta - \xi\left(\ln\frac{\xi}{\epsilon_{min}} + 1 - C\right)}{\xi} \qquad 3.12$$

Landau's universal function has been tabulated by Borch-Sapan and is shown in Figure 1.[88] ξ is a function of particle velocity β, so that for a charged particle of same absolute value of its charge and velocity, ξ will have the same energy.

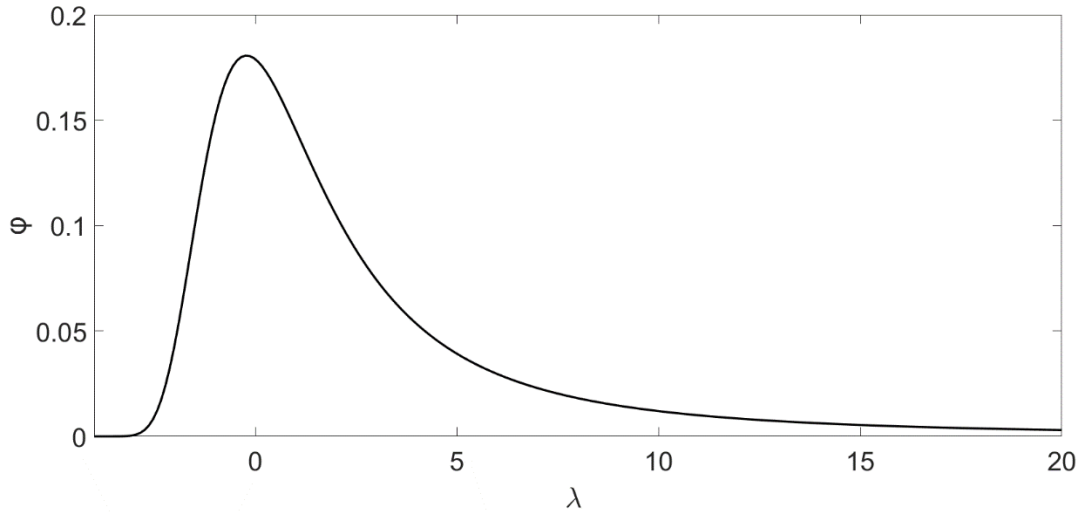

Figure 1. Landau's universal function. Equations 3.11 and 3.12.

Because the maximum energy loss in Landau's theory is unbounded, the area under the curve of the distribution is infinite. Since the proton energy loss is the recoil energy of the electron as determined by the momentum transfer,[89] the largest recoil energy comes from a head-on collision between the proton and the electron. In terms of electron rest energy $m_e c^2$, the incident particle velocity β in units of c, and the Lorentz factor $\gamma^2 = 1/(1-\beta^2)$, from Jackson equation 13.4 (including the factor in the

denominator) the maximum energy imparted by an incident proton to the atomic electron is

$$\epsilon_{max} = \frac{2m_e c^2 \beta^2 \gamma^2}{1 + \frac{2\gamma m_e}{m} + \left(\frac{m_e}{m}\right)^2} \tag{3.13}$$

Where $\left(\frac{m_e}{m}\right)$ is the ratio of the electron mass to the mass of the incident particle. The minimum energy imparted corresponds to momentum transfer with a zero scattering angle, or a glancing collision. Although Equation 3.7 treats the target electron as free, it is bound to the nucleus and has a mean excitation energy I so that Landau gives

$$\epsilon_{min} = \frac{I^2}{\epsilon_{max}} \exp(\beta^2) \tag{3.14}$$

Landau and Vavilov both have equation 3.14 as the implicit lower limit of the integrals over $d\epsilon$ in equations 3.7 and 3.21. I is an empirical parameter that is difficult to determine both theoretically and experimentally[83]. A very crude approximation is $I = Z * 13eV$.[90] Figure 1 shows values of I reproduced from ICRU37 [91] via Rossi.[83]

Rossi gives the mean energy loss per unit length, or "stopping power" $\left(\frac{\overline{\Delta}}{z}\right)$ in terms of $\omega(\epsilon)$

$$\left(\frac{\overline{\Delta}}{z}\right) = \int_{\epsilon_{min}}^{\epsilon_{\max(s)}} \epsilon\, \omega(\epsilon)\, d\epsilon \tag{3.15}$$

Vavilov takes a simplified $\epsilon_{\max(s)}$ such that $\left(\frac{m_e}{m}\right) = 0$

$$\epsilon_{\max(s)} = \frac{2m_e c^2 \beta^2}{(1-\beta^2)} \tag{3.16}$$

Then Vavilov obtains, for the mean energy loss per unit length

$$\left(\frac{\overline{\Delta}}{z}\right) = \int_{\epsilon_{min}}^{\epsilon_{\max(s)}} \epsilon\, \omega(\epsilon) d\epsilon = 0.1534\, \frac{1}{\beta^2}\frac{Z\rho}{A}\left[log\left(\frac{2m_e c^2 \beta^2 \epsilon_{max}}{(1-\beta^2)I^2}\right) - 2\beta^2\right]\frac{MeV}{cm} \quad 3.17$$

Which is the Bethe stopping power formula [54]. Although the Bethe stopping power formula can include a density effect correction, it is zero for clinical energy protons in water.[92] Likewise, detailed cross sections are available that include shell corrections.[43, 93, 94] Bichsel has found that as targets become thicker, the shell structure ceases to influence the shape (but may still affect the mean) of the energy loss distribution $f(\Delta, z)$. [95, 96] Ultimately, in thick targets, the shape of the straggling distribution is determined only by the effective number of inelastic scattering events as a function of p.

Vavilov defines the parameter

$$k = \frac{\xi}{\epsilon_{max}} \quad 3.18$$

which describes the number of inelastic collisions in the target. k can be expressed in terms of the mean free path λ_{in} as $k = \frac{z}{\lambda_{in}}\frac{\epsilon_{min}}{\epsilon_{max}}$. If ξ is much larger than ϵ_{max} then $k >>$ 1 and $f(\Delta, \mathrm{z})$ tends toward a Gaussian distribution. Since ξ is a function of target thickness z, $f(\Delta, \mathrm{z})$ goes to a Gaussian distribution for thick targets. As defined by Rossi,

$$f(\Delta, \overline{\Delta}) \cong \frac{1}{\sqrt{2\pi\sigma_2}} \exp\left[\frac{-(\Delta - \bar{\Delta})^2}{2\sigma_2}\right] \quad 3.19$$

Where

$$\sigma_2 = z\int_0^{\epsilon_{max}} \epsilon^2 \omega(\epsilon) d\epsilon \quad 3.20$$

For small $k < 0.01$, $f(\Delta, z)$ can be described by equations 3.9, 3.11 and 3.12. Vavilov takes the upper limit of equation 3.7 to be ϵ_{max}, equation 3.16. Vavilov's solution to equation 3.2 is then

$$f(\Delta, \mathrm{z}) = \frac{1}{2\pi i}\int_{-i\infty+\sigma}^{+i\infty+\sigma} e^{p\Delta - \mathrm{z}\int_0^{\epsilon\max(s)}\omega(\epsilon)(1-e^{-p\epsilon})d\epsilon}dp \qquad 3.21$$

In equation 3.21, broad distributions are adequately described by small absolute values of p, while narrow distributions require large p to be accurate. For the Landau distribution equation 3.7 where $\epsilon_{max} \to \infty$ and $k \to 0$, the absolute value of the required p is theoretically infinite.

Vavilov (in equation (4')) finds that the exponent of equation 3.21, valid for any value of p can be written as

$$J = p\left(\Delta - z\left(\frac{\overline{\Delta}}{z}\right)\right) - z\int_0^{\epsilon_{max}} \omega(\epsilon)(1 - e^{-\epsilon p} - \epsilon p)d\epsilon \qquad 3.21a$$

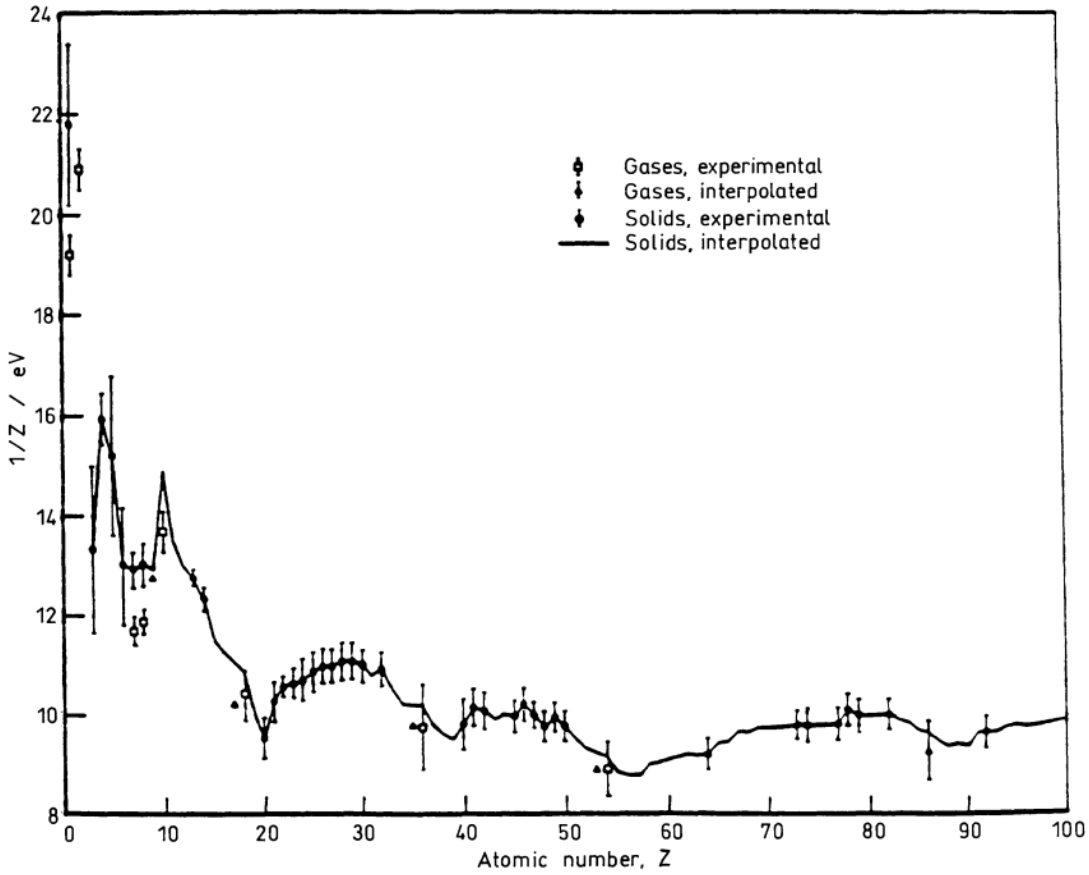

Figure 3.1. The mean excitation energy as a function of Z. (Taken from Rossi[83])

Expanding the integral, Vavilov (equation (5)) obtains

$$J = p\left(\Delta - z\left(\frac{\overline{\Delta}}{z}\right)\right) - p\xi(1+\beta^2) + k(1 - e^{-\epsilon_{max}p}) \qquad 3.21b$$

$$+(k\beta^2 + \xi p)\int_0^{\epsilon_{max}} \frac{1 - e^{-\epsilon p}}{\epsilon}\, d\epsilon$$

The solution to the integral over $d\epsilon$ in equation 3.22c is then Vavilov (equation (6)),

$$\int_0^{\epsilon_{max}} \frac{1 - e^{-\epsilon p}}{\epsilon}\, d\epsilon = C + \log(\epsilon_{max}p) - Ei(-\epsilon_{max}p) \qquad 3.21c$$

Where $Ei(x)$ is the exponential integral function. Vavilov shows that equations 3.21b, and 3.21c go to equations 3.11 and 3.12 when $\epsilon_{max} \to \infty$.

For $k \gtrapprox 1$ Vavilov approximates the exponent of equation 3.21 as a series in p which becomes

$$p\left(\Delta - \int_{\epsilon_{min}}^{\epsilon_{\max}(s)} \omega(\epsilon)\epsilon\, d\,\epsilon\right) + \frac{kp^2}{2!}\int_0^{\epsilon_{\max}(s)} \omega(\epsilon)\epsilon^2\, d\,\epsilon - \frac{kp^3}{3!}\int_0^{\epsilon_{\max}(s)} \omega(\epsilon)\epsilon^3\, d\,\epsilon \qquad 3.22$$

This is an expansion in terms of the moments of $\omega(\epsilon)$. The first term determines the mean energy loss, the second term the width of the distribution, and the third term, the asymmetry (or "skewness") of the distribution. Vavilov reduces these integrals to closed-form solutions in terms of the Airy function.

In the limit that $0 < k < 1$, Vavilov integrates equation 3.21 along the imaginary axis to obtain a "full" solution in terms of sine and cosine integrals $Si(z)$ and $Ci(z)$ given by

$$f(\Delta, z) = \frac{1}{\pi\xi} k e^{k(1+\beta^2 C)} \int_0^{\infty} e^{kf_1} \cos(y\lambda_1 + kf_2)\, dy \qquad 3.23$$

$$f_1 = \beta^2[\log y - Ci(y)] - \cos y - y\, Si(y) \qquad 3.24$$

$$f_2 = y[\log y - Ci(y)] + \sin y + \beta^2 Si(y) \tag{3.25}$$

$$\lambda_1 = \frac{\Delta - z\left(\frac{\overline{\Delta}}{z}\right)}{\epsilon_{max}} - k(1 + \beta^2 - C) \tag{3.26}$$

Shulek makes the modification[95, 97-99]

$$f_1 \rightarrow f_1 - \frac{Dy^2}{\epsilon_{max}} \tag{3.27}$$

Where D accounts for the binding effects of atomic electrons.

$$D = \frac{4}{3}\sum_i I_i f_i \log\left(\frac{2m_e c^2 \beta^2}{I_i}\right) \tag{3.28}$$

$$f_i = \frac{Z_i}{Z} \tag{3.29}$$

In the i'th shell, I_i is the effective excitation potential, f_i is the fraction of the electron population, and Z_i is the number of electrons. Sternheimer gives methods for determining these factors.[100, 101].

Figure 3.2 shows values of k for protons scattering in thin water targets. Figure 3.3 shows the energy loss distributions from the numerical solution of equation 3.21 for various values of k. In a 1 mm target, the straggling distribution of fast (230 MeV) protons with $k \approx 0.02$ resemble the Landau distribution of Figure 3.1. Slow protons in thin targets or fast protons in thicker targets with $k < 1$ have an intermediate-shaped distribution than can be described by Vavilov's full solution equations 3.23 to 3.26. At $k \geq 1$, the distribution can be described by the first three moments, as in equations 3.21 and 3.22. At thicknesses larger than 4mm, $k > 2$ and $f(\Delta, \mathrm{z})$ goes to equations 3.19 and 3.20 due to the large number of inelastic scattering events.

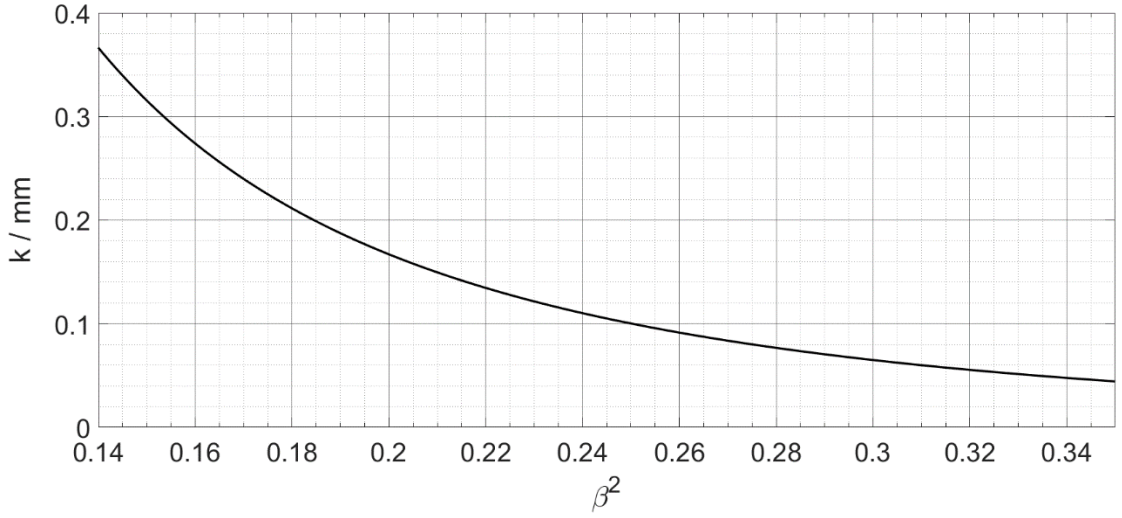

Figure 3.2. k / mm vs β^2 in water. These velocities correspond to proton clinical energies from 70 MeV to 230 MeV.

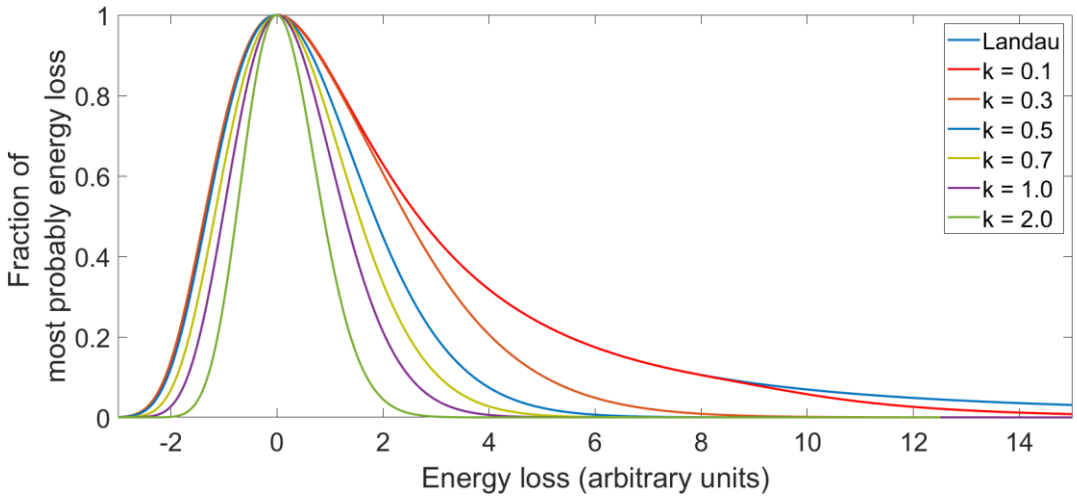

Figure 3.3. Straggling PDF. This is equation 3.21 for different k values at a fixed energy loss. The most probable energy loss is shifted to zero.

Moments methods

Equation 3.22 is an expansion in terms of 3 moments of $\omega(\epsilon)$ applicable for $k \geq 1$. Expressing $f(\Delta, z)$ in terms of additional moments of $\omega(\epsilon)$ allows the calculation of $f(\Delta, z)$ for smaller values of k than equation 3.22. The distribution can then be described

in terms of its deviation from a Gaussian using the Edgeworth expansion equation 3.37.[90, 102] Rotondi writes the transport equation 3.2 in terms of equation 3.30 or Rotondi (7)

$$\frac{d}{dz}\int_0^\infty (\Delta-\overline{\Delta})^n f(\Delta,z)d\Delta = \sum_k \binom{n}{k}\int_{\epsilon_{min}}^{\epsilon_{max}} d\epsilon\, \epsilon^k\, \omega(\epsilon)$$
$$\times \int_0^\infty d\Delta(\Delta-\overline{\Delta}-\epsilon)^{n-k} f(z,\Delta-\epsilon) - \mu_n \int_{\epsilon_{min}}^{\epsilon_{max}} \omega(\epsilon)d\epsilon \qquad 3.30$$

$$\mu_n = \int (\Delta-\overline{\Delta})^n f(\Delta,z)\, d\Delta \qquad 3.31$$

Where μ_n is the n'th moment of the distribution. Rotondi (8a), (8b) and (8c) are

$$\gamma_0 = \int_{\epsilon_{min}}^{\epsilon_{max}} \omega(\epsilon)d\epsilon \quad \gamma_1 = \int_{\epsilon_{min}}^{\epsilon_{max}} \epsilon\, \omega(\epsilon)d\epsilon \qquad 3.32$$

$$\gamma_n = \int_{\epsilon_{min}}^{\epsilon_{max}} \epsilon^n \omega(\epsilon)d\epsilon = \frac{\xi^n}{z}\frac{1}{k^{n-1}}\left(\frac{1}{n-1}-\frac{\beta^2}{n}\right) \text{ (for } n\geq 2) \qquad 3.33$$

$$\alpha_n = \gamma_n z \qquad 3.34$$

So that he can write the transport equation 3.30 as Rotondi (9) or

$$\frac{d}{dz}\mu_n = \sum_{k=2}^{n}\binom{n}{k}\gamma_k\mu_{n-k} \qquad 3.35$$

moments μ_n are given by Rotondi (10), the Edgeworth Expansion by Rotondi (12)

$$\mu_0 = 1 \quad \mu_1 = 0 \quad \mu_2 = \alpha_2 \quad \mu_3 = \alpha_3 \quad \mu_4 = 3\alpha_2^2+\alpha_4 \quad \mu_5 = 10\alpha_2\alpha_3+\alpha_5 \qquad 3.36$$

$$f(z,\Delta) = \frac{1}{\sqrt{2\pi\sigma}}\exp\left(-\frac{\Delta^2}{2\sigma^2}\right)$$
$$\left[1+\frac{1}{3!}\frac{\mu_3}{\sigma^3}H_3\left(\frac{\Delta}{\sigma}\right)+\frac{1}{4!}\left(\frac{\mu_4}{\sigma^4}-3\right)H_4\left(\frac{\Delta}{\sigma}\right)+\frac{1}{5!}\left(\frac{\mu_5}{\sigma^5}-10\frac{\mu_3}{\sigma^3}\right)H_5\left(\frac{\Delta}{\sigma}\right)\right.$$
$$\left.+\frac{10}{6!}\left(\frac{\mu_3}{\sigma^3}\right)^2 H_6\left(\frac{\Delta}{\sigma}\right)+\frac{35}{7!}\frac{\mu_3}{\sigma^3}\left(\frac{\mu_4}{\sigma^4}-3\right)H_7\left(\frac{\Delta}{\sigma}\right)+\frac{280}{9!}\left(\frac{\mu_3}{\sigma^3}\right)^3 H_9\left(\frac{\Delta}{\sigma}\right)\right] \qquad 3.37$$

Where $\sigma=\sqrt{\mu_2}$ as given by equation 3.33 for $n=2$. $H_i(t)$ are the Hermite polynomials of $i'th$ order. Rotondi finds that equation 3.35 (to the 5th moment) accurately calculates

the straggling PDF for $k \geq 0.29$ in thin to intermediate targets where the energy loss distribution is not too broad.[90]

In Lewis equation (10) he proposes an alternative transport equation in terms of the kinetic energy (T) distribution function $f(T,z)$ at some depth z. The mass of the incident particle is M and the electron mass is m_e. Lewis defines the parameters m_u, m_d and K

$$m_u = 4\left(\frac{m_e}{M}\right)\left(1+\frac{m_e}{M}\right)^{-2} \tag{3.38}$$

$$m_d = \frac{I^2}{m_u T^2} \tag{3.39}$$

$$K = 2\pi \frac{N_A}{A} Z e^4 \frac{M}{m_e} \tag{3.40}$$

So that the transport equation is

$$\frac{\partial f(T',z)}{\partial z} = \frac{1}{2}K\left[\int_{\frac{T'}{1-m_d}}^{\frac{T'}{1-m_u}} \frac{f(T,z)dT}{T(T-T')^2} - \frac{f(T',z)}{T'}\int_{m_d T'}^{m_u T'} \frac{dT}{(T'-T)^2}\right] \tag{3.41}$$

Tschalar solves equation 3.41 in the manner of equations 3.30 to 3.37, in terms of the cumulants of the cross section. In the version of his theory that does not remove particles from the distribution as their energy loss exceeds the initial energy, he calculated energy loss distributions for thick targets distributions for up to 80% of initial particle energy. The solution accurately accounts for the increased broadening and skewness of the energy loss distribution for very thick targets, due to the variation in the cross section across the energy loss distribution.[103, 104 105] Tschalar also cancels the material dependent parameter K, by replacing z with the mean energy per unit length as an approximation to the stopping power.

In Ferrari equations (1) to (10), FLUKA calculates the straggling distribution in terms of the cumulants of the straggling distribution

$$k_m^{\Delta} = \sum_{i=1}^{N_d} N\sigma z E_i + Nz\left[\int_{\eta}^{T_{min}} dT_e \frac{d\sigma_\delta}{dT_e}\right]\left[\int_{\eta}^{T_{min}} dT_e\, T_e^m \frac{d\sigma_\delta}{dT_e}\right] \qquad 3.42$$

Where $\frac{d\sigma_\delta}{dT_e}$ is the secondary electron (delta ray) production cross section, T_{min} is the minimum delta ray energy, η is the cutoff energy between "close" and "distant" collisions, and E_i are the energy levels for excitation and ionization.[45] FLUKA samples among the cumulants (equation 3.42) to 6th order to obtain the energy loss distribution, provided it doesn't deviate too much from a gaussian. If the distribution is very non-gaussian, delta rays are produced explicitly and their energy is added to the energy loss distribution.

An advantage to the methods of Tschalar, and the FLUKA team is that they can be quickly used to calculate distributions where there is variation in the cross section across the energy loss distribution $f(\Delta, \epsilon)$ in thick targets. Assuming a constant $\omega(\epsilon)$ across the straggling distribution can result in distributions that are far too narrow. The assumption of a constant $\omega(\epsilon)$ over the straggling distribution is a limitation of Landau and Vavilov's formulations. However, the moments (or cumulants) methods are limited to distributions where k is not too small. As k approaches 0, the number of moments required to describe the distributions goes to infinity. All of the authors of the moments method found diminishing returns when the number of moments exceeds 6 (Rotondi) or 9 (FLUKA team). Therefore, these methods cannot calculate energy loss distributions for very small values of k as in very thin targets.

Figure 3.4 shows a comparison of the energy loss of 230 MeV protons in 23.4 microns of water for FLUKA Monte Carlo with the Landau distribution. This corresponds to a Vavilov k parameter of 0.001. Due to the finite number of moments used to calculate straggling distributions in FLUKA, it does not calculate a Landau distribution for the energy straggling despite being in that regime of k.

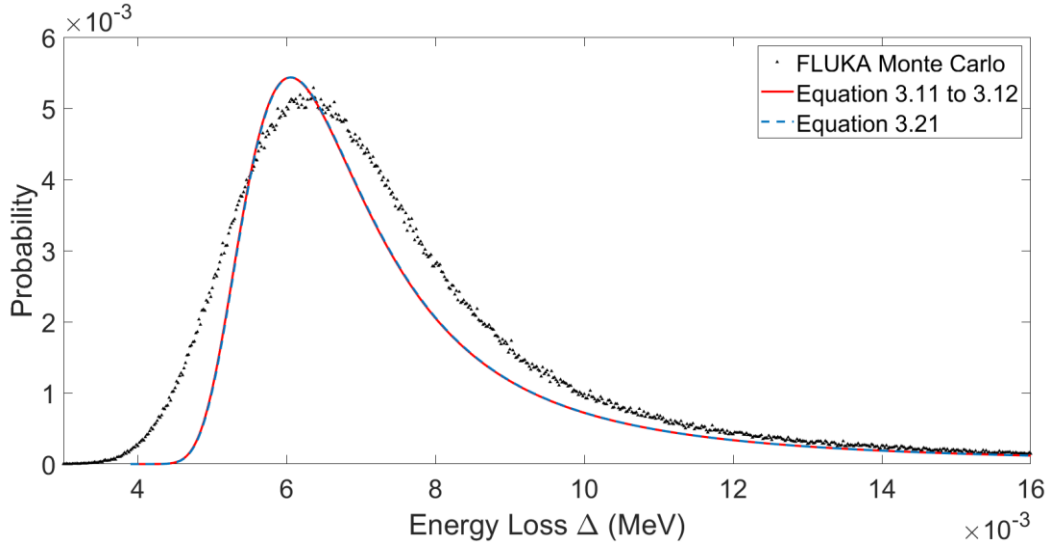

Figure 3.4. Energy straggling in a very thin target. Energy straggling of 230 MeV protons in 23.4 microns of water, corresponding to $k = 0.001$. Equations 3.11 to 3.12 are from a lookup table, equation 3.21 was solved numerically.

Williams and later, Herring, showed that the distribution $f(\Delta, z)$ from may be calculated from the convolution of the single scattering spectra or from the self-convolution of the distribution for $f(\Delta, z)$ in an infinitesimal layer.[106, 107] Kellerer later applied this method to Monte Carlo.[82]

Energy loss distributions from Fourier transforms

Herring finds the corollary to equation 3.7 in terms of the Fourier transforms.[106] Each inelastic collision is statistically independent and the energy loss Δ in a path length

z is the sum of the individual energy losses from n total collisions along that path length. [44, 83, 95, 98, 106, 108] this is Kellerer equation (35)

$$\Delta(z) = \sum_{i=1}^{n} \epsilon_i \tag{3.43}$$

The average number of collisions in a path length (Herring equation (4)) is then

$$\nu = z\omega_{inel} \tag{3.44}$$

The events in a given path length are Poisson distributed so that the probability of undergoing n collisions is Herring equation (1)

$$p(n) = \frac{\exp(-\nu)\,\nu^n}{n!} \tag{3.45}$$

Since the inelastic scattering events are Poisson distributed, their distribution of energy losses in n collisions can be described as the n convolutions of the spectra from the inelastic scattering cross section. Bichsel (1975) equation (19) is

$$\int_0^{\Delta} \omega(\epsilon)\omega^{*(n-1)}(\Delta - \epsilon)d\epsilon \tag{3.46}$$

So that the energy loss distribution $f(\Delta, z)$ is Herring equation (6)

$$\frac{f(\Delta, z)}{z} = \frac{\exp(-\nu)\,\nu^n}{n!} \int_0^{\Delta} \omega(\epsilon)\omega^{*(n-1)}(\Delta - \epsilon)d\epsilon \tag{3.47}$$

Herring expresses equation 3.48 in terms of Fourier transforms (Herring equation (7))

$$\int_{-\infty}^{\infty} e^{ip\Delta} \left[\int_0^{\infty} \omega(\epsilon) e^{-ip\epsilon}\, d\epsilon \right]^n d\Delta \tag{3.48}$$

Summing the series in equation 3.48, Herring obtains

$$f(\Delta, x) = \frac{1}{2\pi} \int_0^{\infty} e^{ip\Delta - z\int_0^{\infty}\left(1 - e^{-ip\epsilon}\right)\omega(\epsilon)d\epsilon} \tag{3.49}$$

The integral $d\epsilon$ determines the effective number of inelastic collisions per unit length as a function of the reciprocal energy loss parameter p.

For electron energy loss straggling distributions, McLellan[44] found the Fourier transforms of the energy loss distributions ϕ for electron "soft" scattering, "hard" scattering and in terms of bremsstrahlung. McLellan considered collisions with energy losses below a cutoff energy to be "soft" scattering, with "hard" scattering collisions above this energy. For relativistic electrons of 1 MeV, Bremsstrahlung in water accounts for about 1% of total stopping power and dominates stopping power at energies above 100 MeV. [10] [44] McLellan finds the complete energy loss distribution by taking the convolution of "soft," "hard" and Bremsstrahlung distributions, which is equivalent to the product of Fourier transforms.

McLellan equation (13) finds the complete energy loss distribution from the inverse Fourier transform of the convolution

$$f(\Delta, z) = \mathcal{F}^{-1}\left[\phi(\mathrm{p,z})_{Brehm} * \phi(\mathrm{p,z})_{Soft} * \phi(\mathrm{p,z})_{Hard}\right] \qquad 3.50$$

Using convolutions of Fourier transforms and equation 3.49, let us extend Landau's and Vavilov's treatments to include very thick targets.

An extension of Landau-Vavilov theory to very thick targets

For thick targets, the statistical independence of the collisions means that the distribution $f(\Delta, z)$ is a convolution of the straggling distribution functions along the path length z.[82] Let us divide the path length into n intervals of infinitesimal size dz. Then we take the convolution of the straggling functions at each depth, with each interval of z given by dz and indexed 1,2,3…

$$f_1(\Delta, dz) * f_2(\Delta, dz) * f_3(\Delta, dz) \ldots \qquad 3.51$$

This can be expressed in Fourier space as a sum of exponents in equation 3.49. $\omega_i(\epsilon, z)$ is the probability per unit length per energy loss ϵ in the i'th depth interval and $\epsilon_{i_{min}}(z)$ and $\epsilon_{i_{max}}(z)$ are the kinematically allowed minimum and maximum values of ϵ for proton kinetic energy at that depth.

$$z\int_{\epsilon_{min}}^{\epsilon_{max}}\left(1-e^{-ip\epsilon}\right)\omega(\epsilon)d\epsilon=\sum_{i=1}^{n}dz_i\int_{\epsilon_{i_{min}}(z)}^{\epsilon_{i_{max}}(z)}\left(1-e^{-ip\epsilon}\right)\omega_i(\epsilon,z)d\epsilon \qquad 3.52$$

So that

$$f(\Delta,z)=\frac{1}{2\pi}\int_{-\infty}^{\infty}e^{ip\Delta-\sum_{i=1}^{n}dz_i\int_{\epsilon_{min}(z)}^{\epsilon_{max}(z)}\left(1-e^{-ip\epsilon}\right)\omega_i(\epsilon,z)d\epsilon}\,dp \qquad 3.53$$

Let us express $\omega(\epsilon, z)$, $\epsilon_{min}(z)$ and $\epsilon_{max}(z)$ as a function of the kinetic energy of the incident proton so that $\omega_i(\epsilon, z) \rightarrow \omega_i(\epsilon, E)$, $\epsilon_{i_{min}}(z) \rightarrow \epsilon_{i_{min}}(E)$, $\epsilon_{i_{max}}(z) \rightarrow \epsilon_{i_{max}}(E)$. Let us also express z terms of the continuous slowing down approximation equation 1.11

$$z=\frac{dE}{\frac{\overline{\Delta}}{z}(E)} \qquad 3.54$$

Thereby converting the sum over z to an integral of the inverse of the stopping power $\frac{\overline{\Delta}}{z}(E)$ over dE. We then obtain

$$\sum_{i=1}^{n}dz_i\int_{\epsilon_{min}(z)}^{\epsilon_{max}(z)}\left(1-e^{-ip\epsilon}\right)\omega_i(\epsilon,z)d\epsilon=\int_{E_0-\overline{\Delta}}^{E}\frac{\int_{\epsilon_{min}(E)}^{\epsilon_{max}(E)}\omega(\epsilon,E)\left(1-e^{-ip\epsilon}\right)d\epsilon}{\frac{\overline{\Delta}}{z}(E)}dE \qquad 3.55$$

where $\overline{\Delta}$ is the average energy loss. It is illuminating to apply equation 3.1 to the integrand of equation 3.55 and take (from Rossi equation III.91)

$$n_e = \frac{\omega_{inel}(E)}{\frac{\overline{\Delta}}{z}(E)} \tag{3.56}$$

where n_e is the total number of collisions per unit of energy lost. The integrand of equation 3.55 is then

$$n_e - \frac{\int_{\epsilon_{min}}^{\epsilon_{max}} e^{-ip\epsilon}\omega(\epsilon, E)d\epsilon}{\frac{\overline{\Delta}}{z}(E)} \tag{3.57}$$

Equation 3.57 is the effective number of collisions per unit of energy lost, as a function of the reciprocal energy loss parameter p.

Inserting equation 3.17 into equation 3.55, we then can factor and cancel ξ/z in $\omega(\epsilon, E)$ and $\frac{\overline{\Delta}}{z}(E)$ in equation 3.55. For $\omega(\epsilon)$ with a $1/\epsilon^2$ dependence as in equation 3.8 this leaves

$$f(\Delta, z) = \int_{-\infty}^{\infty} \exp\left[ip\Delta - \int_{E_0-\overline{\Delta}}^{E} \frac{\int_{\epsilon_{min}(E)}^{\epsilon_{max}(E)} \frac{\left(1 - e^{-ip\epsilon}\right)d\epsilon}{\epsilon^2}}{log\left(\frac{\epsilon_{\max(s)}(E)}{\epsilon_{min}(E)}\right)} dE\right] dp \tag{3.58}$$

Equation 3.58 is a function of only the minimum and maximum values of ϵ and the average energy loss $\overline{\Delta}$. It, therefore, applies to any material, though the mean excitation energy must be known to calculate $\epsilon_{min}(E)$. The numerator of the integrand of equation 3.58 can be solved numerically, but for $\omega(\epsilon)$ in the form of equation 3.8, we can adapt equations 3.21a, 3.21b and 3.21c to the Fourier transform by replacing $p\epsilon$ with $ip\epsilon$. We also apply the lower integration limit ϵ_{min} explicitly. Having already replaced z with equation 3.54 in equation 3.58 and canceled the factor ξ we therefore obtain

$$-\int_{\epsilon_{min}}^{\epsilon_{max}} \frac{\left(1 - e^{-ip\epsilon}\right)d\epsilon}{\epsilon^2} = -ip\int_{\epsilon_{min}}^{\epsilon_{max}} \frac{d\epsilon}{\epsilon} - \int_{\epsilon_{min}}^{\epsilon_{max}} \frac{\left(1 - e^{-ip\epsilon} - \epsilon p\right)}{\epsilon^2} d\epsilon \tag{3.59}$$

$$-\int_{\epsilon_{min}}^{\epsilon_{max}} \frac{\left(1-e^{-ip\epsilon}-\epsilon p\right)}{\epsilon^2} d\epsilon = -ip(1+\beta^2) + \frac{1}{\epsilon_{max}}\left(1-e^{-ip\epsilon_{max}}\right) + \left(\frac{\beta^2}{\epsilon_{max}} + ip\right)\int_{\epsilon_{min}}^{\epsilon_{max}} \frac{1-e^{-ip\epsilon}}{\epsilon} d\epsilon \quad 3.60$$

$d\epsilon$ on the right side of equation 3.60 is

$$\int_{\epsilon_{min}}^{\epsilon_{max}} \frac{1-e^{-ip\epsilon}}{\epsilon} d\epsilon = Ei(ip\epsilon_{max}) - Ei(ip\epsilon_{min}) + \log\frac{\epsilon_{max}}{\epsilon_{min}} \quad 3.61$$

So that the numerator of equation 3.58 is

$$\int_{\epsilon_{min}}^{\epsilon_{max}} \frac{\left(1-e^{-ip\epsilon}\right)d\epsilon}{\epsilon^2} = -ip\left(\log\left(\frac{\epsilon_{max}}{\epsilon_{min}}\right)\right) - ip(1+\beta^2) + \frac{1}{\epsilon_{max}}\left(1-e^{-ip\epsilon_{max}}\right) + \left(\frac{\beta^2}{\epsilon_{max}} + ip\right)\left[Ei(ip\epsilon_{max}) - Ei(ip\epsilon_{min}) + \log\frac{\epsilon_{max}}{\epsilon_{min}}\right] \quad 3.62$$

And the straggling distribution is

$$f(\Delta, z) = \frac{1}{2\pi}\int_{-\infty}^{\infty} \exp\left[ip\Delta - \int_{E_0-\overline{\Delta}}^{E_0} \frac{\int_{\epsilon_{min}(E)}^{\epsilon_{max}(E)}\left(1-e^{-ip\epsilon}\right)/\epsilon^2\, d\epsilon}{\log(\epsilon_{\max(s)}(E)/\epsilon_{min}(E))} dE\right] dp \quad 3.63$$

Where $\int_{\epsilon_{min}(E)}^{\epsilon_{max}(E)}\left(1-e^{-ip\epsilon}\right)/\epsilon^2\, d\epsilon$ is given by equation 3.62. The limits of integration for dE in equation 3.63 go from the average residual energy $E_0 - \overline{\Delta}$ to the initial energy E_0 for all Δ. This assumes that $\omega(\varepsilon, E)$, $\epsilon_{min}(E)$, $\epsilon_{max}(E)$ are constant across the straggling distribution $f(\Delta, z)$. If we want to find the correct number of collisions for the energy loss Δ rather than $\overline{\Delta}$ then $\omega(\epsilon, E)$, $\epsilon_{min}(E)$ and $\epsilon_{max}(E)$ should depend on Δ rather than $\overline{\Delta}$. The particles with energy loss Δ have traversed the same path length z as the particles having energy loss $\overline{\Delta}$. Since the particles have lost energy Δ, the interval of dE in equation 3.63 should be $[E_0 - \Delta, E_0]$. Since the path length z remains unchanged for all Δ, the stopping power $\frac{\overline{\Delta}}{z}(E)$ must be such that equation 3.54 is still obeyed. The stopping

power $\frac{\overline{\Delta}}{z}(E)$ should therefore continue to depend on $\overline{\Delta}$ rather than Δ, with integration limits for $\frac{dE}{\frac{\overline{\Delta}}{z}(E)}$ being $E_0 - \overline{\Delta}$ to E_0.

To integrate $\frac{\overline{\Delta}}{z}(E)$ in the appropriate limits, we want to find a function $g(x)$ such that

$$\int_a^b f(x)dx = \int_A^b \frac{dg(x)}{dx} f\big(g(x)\big)dx \tag{3.64}$$

We find

$$g(x) = a + \frac{b-a}{b-A}(x - A) \tag{3.65}$$

$$\frac{dg(x)}{dx} = \frac{b-a}{b-A} \tag{3.66}$$

Setting $f(x) = \frac{1}{\frac{\overline{\Delta}}{z}(x)}$ and $b = E_0$, $a = E_0 - \overline{\Delta}$, $A = E_0 - \Delta$ then

$$g(x) = (E_0 - \overline{\Delta}) - \left(\frac{\overline{\Delta}}{\Delta}\right)(x - E_0 + \Delta) \tag{3.67a}$$

$$\frac{dg(x)}{dx} = \left(\frac{\overline{\Delta}}{\Delta}\right) \tag{3.67b}$$

Substituting $E = x$ and $dE = dx$ equation 3.64 becomes

$$\int_{E_0-\overline{\Delta}}^{E_0} \frac{dE}{\frac{\overline{\Delta}}{z}(E)} = \left(\frac{\overline{\Delta}}{\Delta}\right) \int_{E_0-\Delta}^{E_0} \frac{dE}{\frac{\overline{\Delta}}{z}(g(E))} \tag{3.68}$$

Taking $\overline{\Delta} \to \Delta$ in equation 3.58 and making the substitution $\frac{dE}{\frac{\overline{\Delta}}{z}(E)} \to \left(\frac{\overline{\Delta}}{\Delta}\right)\frac{dE}{\frac{\overline{\Delta}}{z}(g(E))}$ from equation 3.68 then equation 3.55 becomes

$$\left(\frac{\overline{\Delta}}{\Delta}\right) \int_{E_0-\Delta}^{E} \frac{\int_{\epsilon_{min}(E)}^{\epsilon_{max}(E)} \omega(\epsilon, E)\big(1 - e^{-ip\epsilon}\big)d\epsilon}{\frac{\overline{\Delta}}{z}(g(E))} dE \tag{3.69}$$

Canceling the terms of $\omega(\epsilon, E)$ and $\frac{\Delta}{z}(g(E))$ which are not functions of ϵ or E, this leaves $\beta^2(g(E))$ from $\frac{\bar{\Delta}}{z}(g(E))$ in the numerator and $\beta^2(E)$ from $\omega(\epsilon, E)$ in the denominator.

$$\left(\frac{\bar{\Delta}}{\Delta}\right)\int_{E_0-\Delta}^{E}\frac{\beta^2(g(E))\int_{\epsilon_{min}(E)}^{\epsilon_{max}(E)}\frac{\left(1-e^{-ip\epsilon}\right)}{\epsilon^2}d\epsilon}{\beta^2(E)\log\left(\frac{\epsilon_{\max(s)}(g(E))}{\epsilon_{min}(g(E))}\right)}dE \qquad 3.70$$

$f(\Delta, z)$ is then

$$f(\Delta,z)=\frac{1}{2\pi}\int_{-\infty}^{\infty}\exp\left[ip\Delta-\left(\frac{\bar{\Delta}}{\Delta}\right)\int_{E_0-\Delta}^{E}\frac{\beta^2(g(E))\int_{\epsilon_{min}(E)}^{\epsilon_{max}(E)}\frac{\left(1-e^{-ip\epsilon}\right)}{\epsilon^2}d\epsilon}{\beta^2(E)\log\left(\frac{\epsilon_{\max(s)}(g(E))}{\epsilon_{min}(g(E))}\right)}dE\right]dp \qquad 3.71$$

Comparison with FLUKA

For comparisons with FLUKA Monte Carlo, FLUKA was run with a pristine beam normally incident on phantoms of different materials. FLUKA was run with EMFCUT, IONFLUCT, MCSTHRES, DISCARD, DELTARAY, THRESHOL, and STEPSIZE cards and where physics was disabled, it was disabled by setting the threshold above the initial beam energy (to 1 GeV). Using EMFCUT, the production of secondary electrons and gammas was disabled. DELTARAY was used to disable transport of secondary electrons. THRESHOL was used to disable hadronic elastic and inelastic scattering of protons. The range of the energy loss STEPSIZE was from $[10^{-3}, 10^{-1}]$ cm. IONFLUCT for hadrons was set to 4 for the most detailed straggling calculations. Scoring was performed with the USRYIELD setting measuring proton fluence with respect to lab kinetic energy and lab angle (from 0 to π). A 230 MeV proton energy was chosen for all simulations because it allows the broadest choice of depths and the smallest

value of k for a given target thickness (see Figure 3.2). The probability distributions were normalized such that they sum to 1 for each $f(\Delta, z)$. To solve $d\epsilon$ in equation 3.71, we used the relation in equation 3.62. The integrals over dE and dp were solved numerically.

For comparison with the Gaussian approximation, we found σ_2 in equation 3.19 by integrating equation 3.20 over the energy loss $\overline{\Delta}$

$$\sigma_2 = \frac{1}{\overline{\Delta}} \int_{E_0 - \overline{\Delta}}^{E_0} \int_0^{\epsilon_{max}(E)} \omega(\epsilon) \epsilon^2 \, d\epsilon = \frac{1}{\overline{\Delta}} \int_{E_0 - \overline{\Delta}}^{E_0} \xi(E) \, \epsilon_{max}(E) \, dE \qquad 3.72$$

We determined $\overline{\Delta}$ from the CSDA range in water by finding the zero of the relation

$$\delta R(\overline{\Delta}) = z - \int_{\overline{\Delta}}^{E_0} \frac{dE}{\left(\frac{\Delta}{z}(E)\right)} \qquad 3.73$$

Where $\delta R(\overline{\Delta})$ is the deviation from the CSDA range at $\delta R(\overline{\Delta}) = 0$. For materials other than water, $\overline{\Delta}$ was determined from FLUKA's probability distributions.

Figure 3.4 shows that equation 3.71 accurately reproduces the Vavilov distribution in a thin water target. The Landau distribution is shown for comparison. Figure 3.6 through 3.9 shows that equation 3.71 agrees with energy loss distributions calculated by FLUKA, including the skewness and width of distributions for thick targets. The additional widening of the straggling distribution with depth due to the variation in $\omega(\epsilon)$ across the straggling distribution is visible in its deviation from the Gaussian approximation equation 3.19. The Gaussian distribution itself is roughly correct at shallow depths but overall is too narrow for much of the distribution.

Figures 3.10 and 3.11 show deviation of equation 3.71 from FLUKA, with figure 3.11 showing a long tail that is inconsistent with the FLUKA distributions. For water

targets thicker than 30cm (as in Figure 3.11), with higher mean energy losses, equation 3.71 no longer produces reasonable results. The energy loss in Figure 3.11 is approximately 80% of the initial beam energy. If we take the energy loss in Figure 3.11 as the upper limit of validity of equation 3.71, then it has the same range of validity as Tschalar's theory.

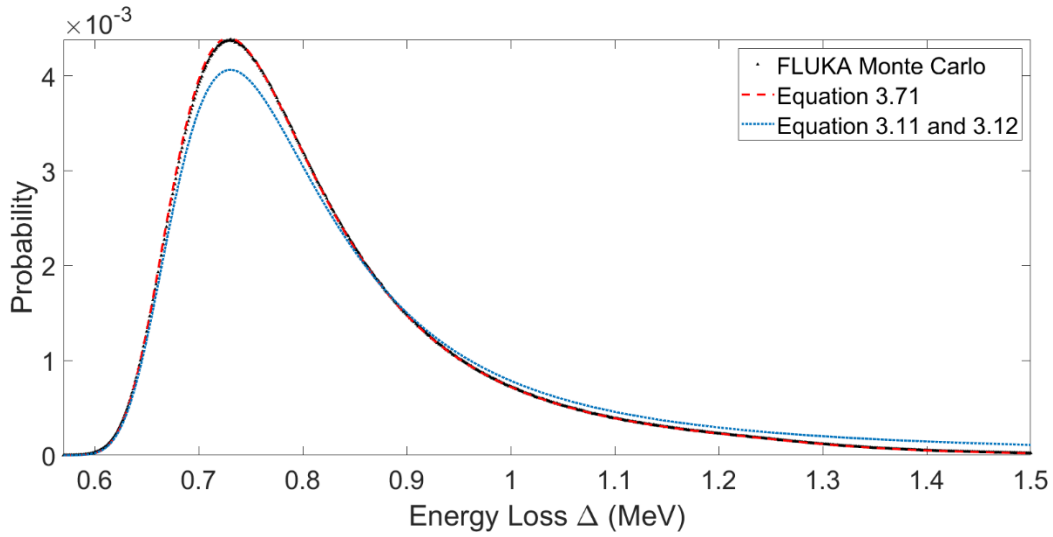

Figure 3.5. Energy straggling distribution in 0.2 cm of water. 230 MeV proton beam.

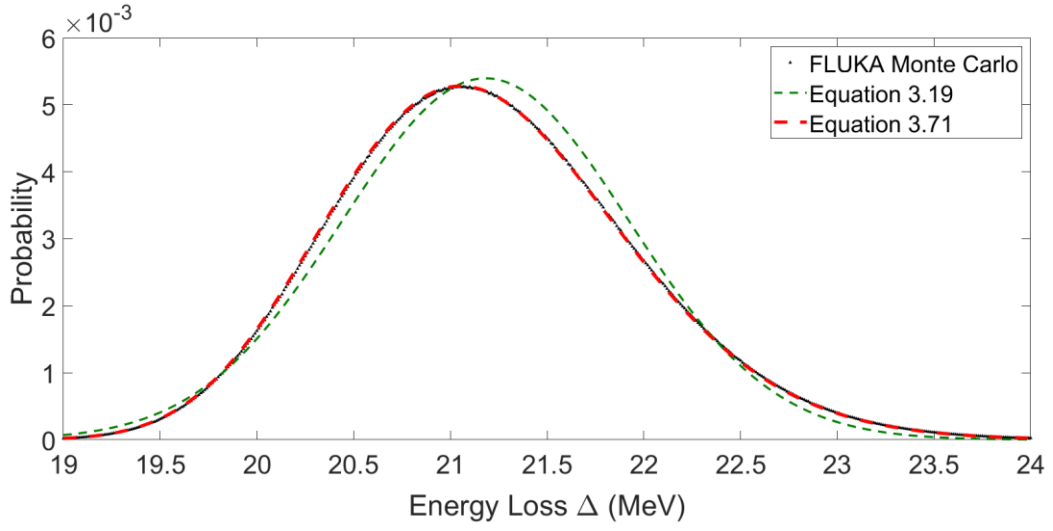

Figure 3.6. Energy straggling distribution in 5 cm of water. 230 MeV proton beam.

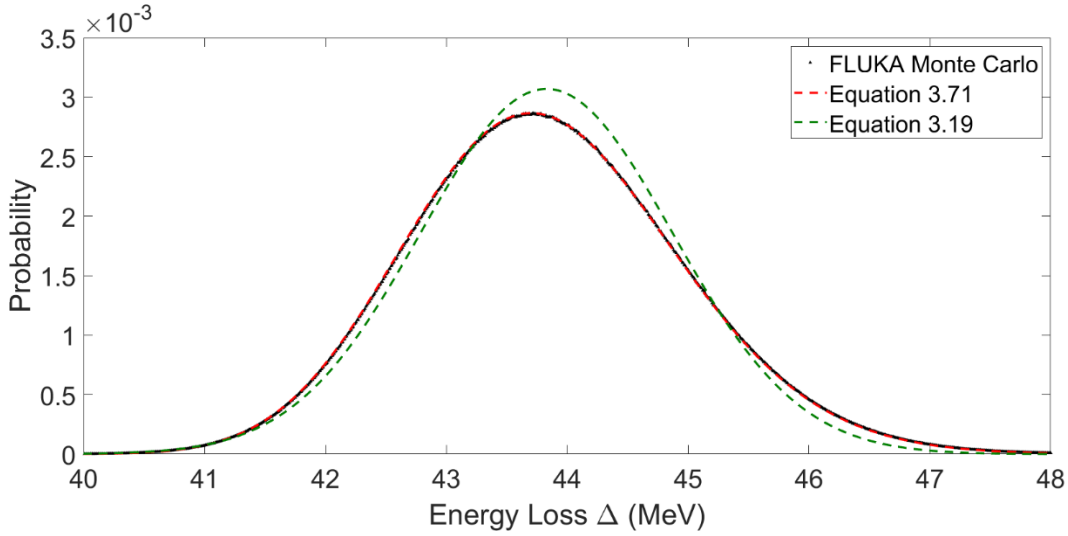

Figure 3.7. Energy straggling distribution in 10 cm of water. 230 MeV proton beam.

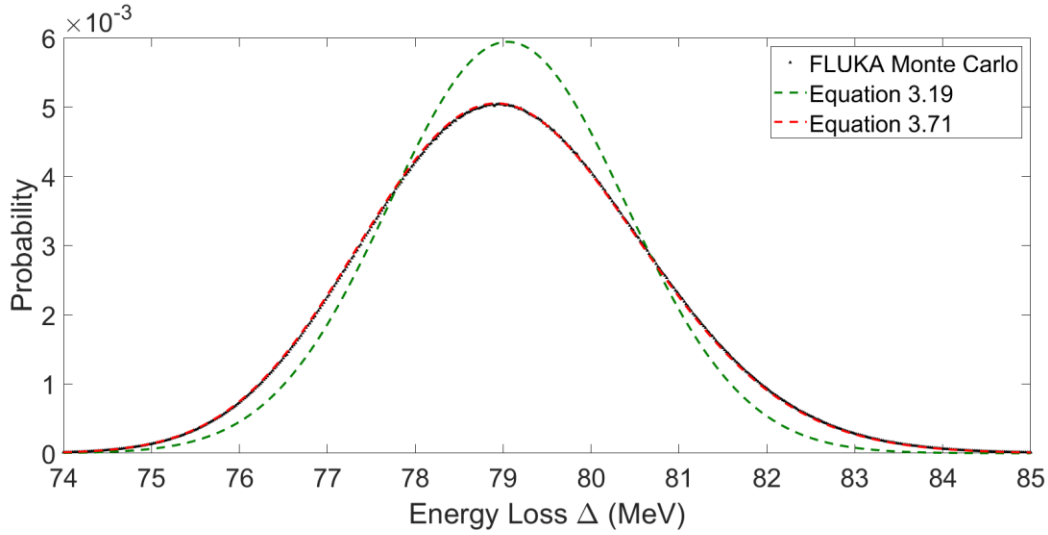

Figure 3.8. Energy straggling distribution in 17 cm of water. 230 MeV proton beam.

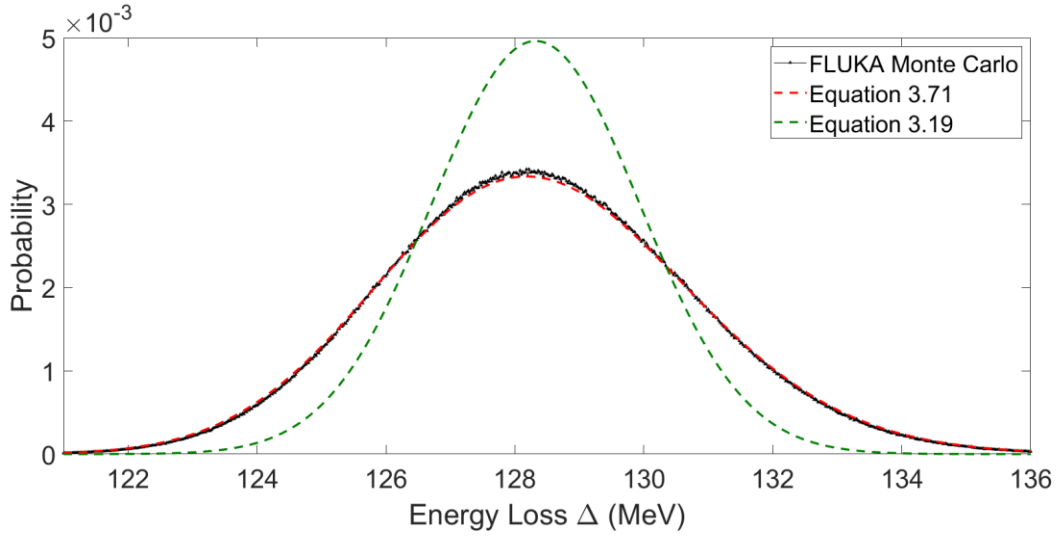

Figure 3.9. Energy straggling distribution in 25 cm of water. 230 MeV proton beam.

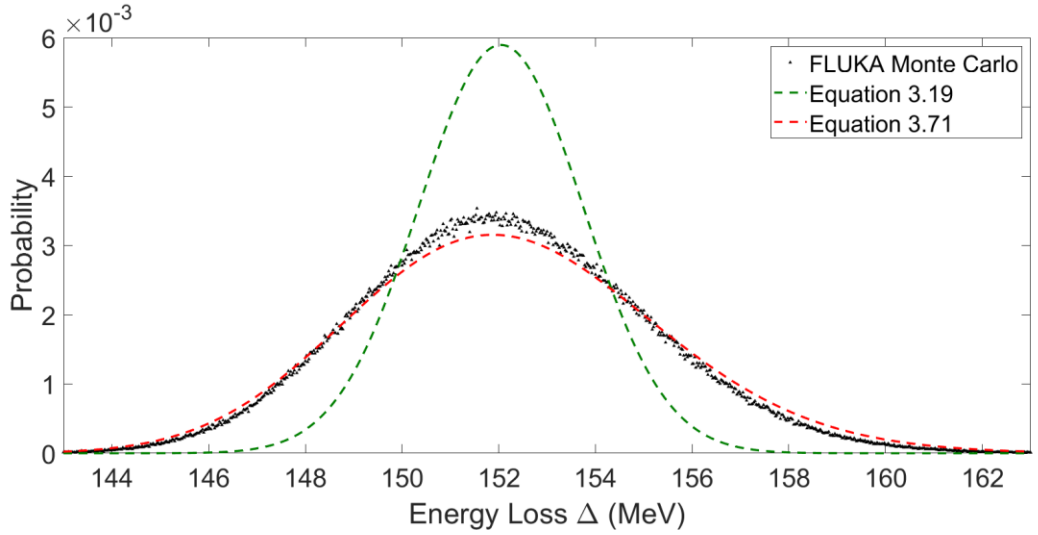

Figure 3.10. Energy straggling distribution in 28 cm of water. 230 MeV proton beam.

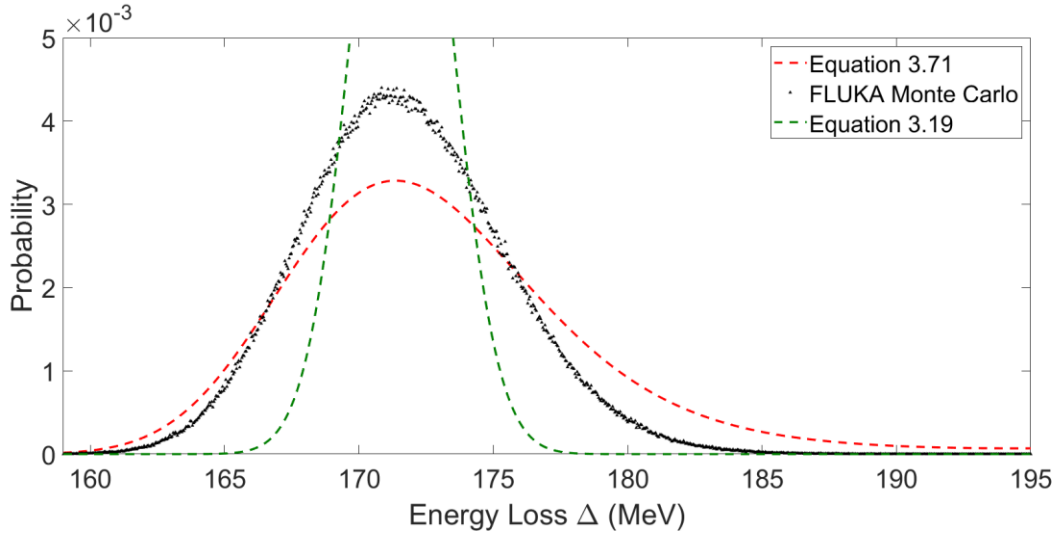

Figure 3.11. Energy straggling distribution in 30 cm of water. 230 MeV proton beam.

Figures 3.12, 3.13 and 3.14 compare equation 3.71 with energy loss distributions from FLUKA in graphite, iron and lead. Figure 3.12 shows agreement with FLUKA, as does Figure 3.13. In figure 3.14, the energy loss in 3cm of tungsten is at the edge of the validity of equation 3.71 (80% of initial beam energy), just as in figure 3.11.

Figure 3.15 shows the energy loss distributions dependence on the mean excitation energy I, which is the only material specific parameter.

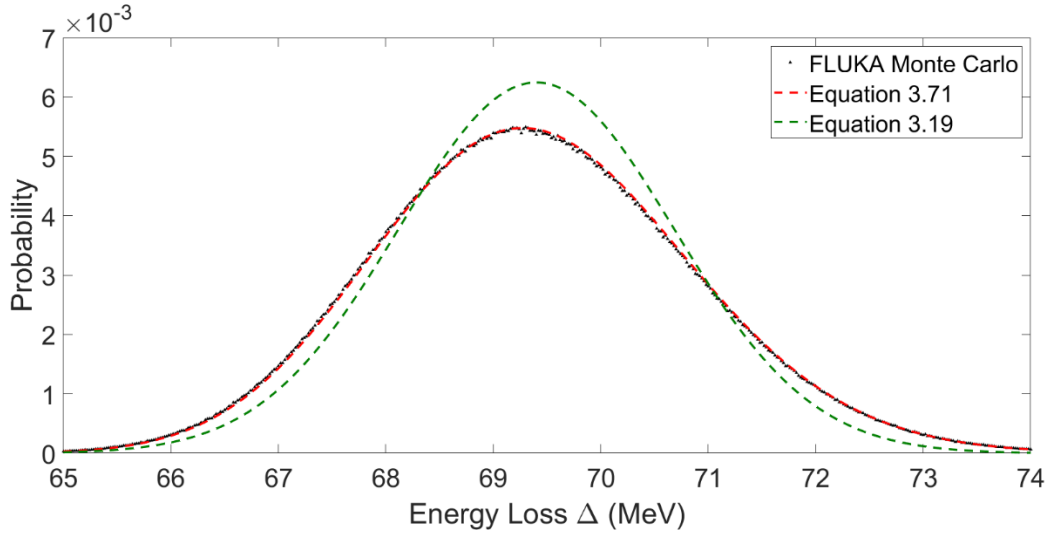

Figure 3.12. Energy straggling distribution in 10 cm of graphite. 230 MeV proton beam.

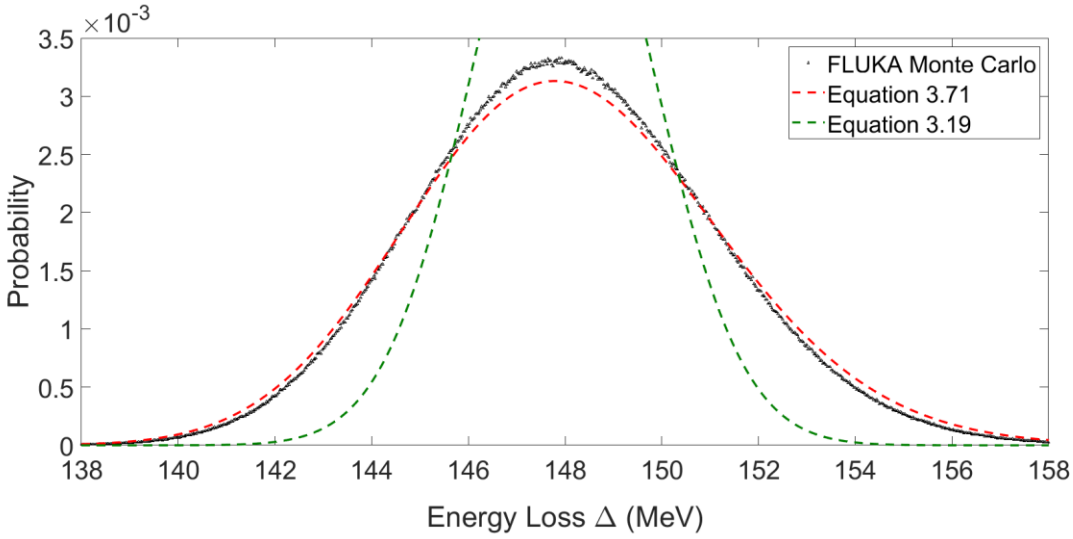

Figure 3.13. Energy straggling distribution in 5 cm of iron. 230 MeV proton beam.

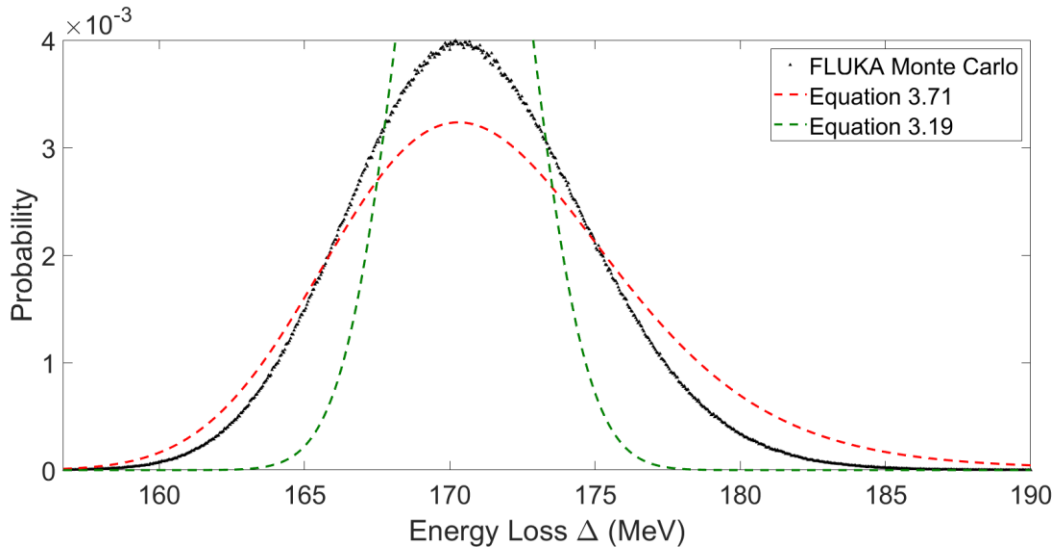

Figure 3.14. Energy straggling distribution in 3 cm of tungsten. 230 MeV proton beam.

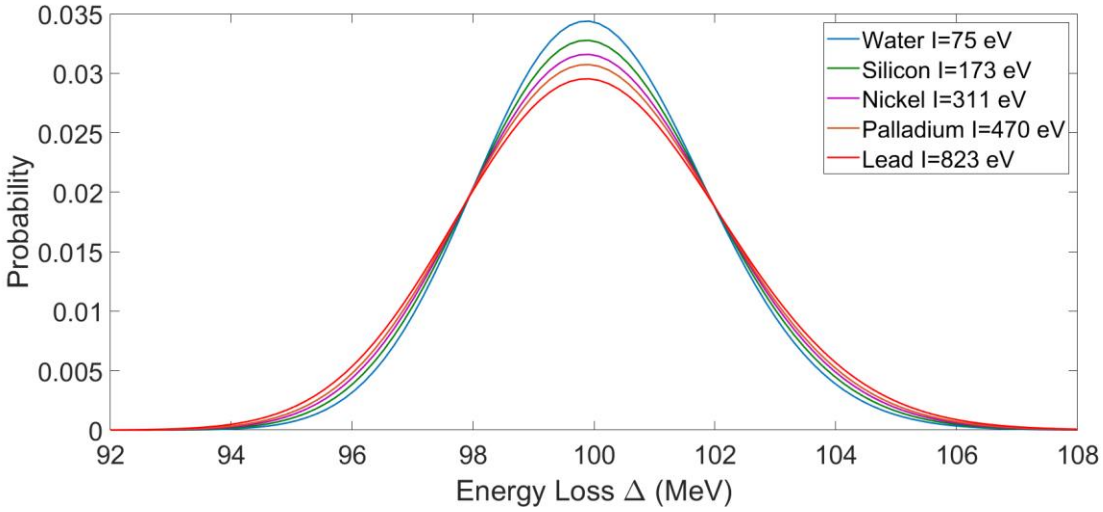

Figure 3.15. Energy straggling distributions in various materials for the same $\overline{\Delta}$. 230 MeV initial energy.

Conclusion

We have shown that equation 3.71 agrees with FLUKA Monte Carlo results, except for very thin and very thick targets. Equation 3.71 remains valid to approximately 80% of the energy loss of the initial beam. The cancellation of material dependent factors in $\omega(\epsilon)$ and $\omega(\epsilon, E)$, resulting in equations 3.58 and 3.70 means that the energy loss spectrum can be calculated from only the characteristics of the incident particle and the electron, the initial energy, mean energy loss and mean excitation energy of the target. Aside from the mean excitation energy, probability energy loss distributions are independent of the target material. In practice, one may know the dimensions of a material but not the mean energy loss. In that case, one may calculate the mean energy loss from equation 3.73, providing one has the correct stopping power for that material.

The integrals over dp do not require large absolute values of p, and one may find the probability of a specific energy loss Δ without calculating all of $f(\Delta, z)$. It may therefore be calculated quickly in a treatment planning system or Monte Carlo code.

To better apply this theory to a real accelerator, one might take the convolution of a function describing the initial beam spectrum at the accelerator nozzle with that due to energy loss in the target as described here.

CHAPTER 4

NUCLEAR INELASTIC SCATTERING

Nuclear basics

Although elastic and inelastic coulomb scattering are the primary interactions of protons in a patient, protons also interact with the atomic nuclei through hadronic (nuclear) processes. The probability of a proton nuclear interaction is given by the total nuclear cross section σ_{nuc}. The mean free path λ_{nuc} is

$$\lambda_{nuc} = \frac{1}{N\sigma_{nuc}} \tag{4.1}$$

Where N is the number of scattering centers per unit volume, which is 3.34×10^{22} cm^{-3} for water. It can be seen in figure 4.1 that the maximum nuclear cross section is at approximately 26 MeV. Using equation 4.1, this corresponds to a minimum mean free path of 56 cm. The cross section is zero below the threshold energy of about 6 MeV.

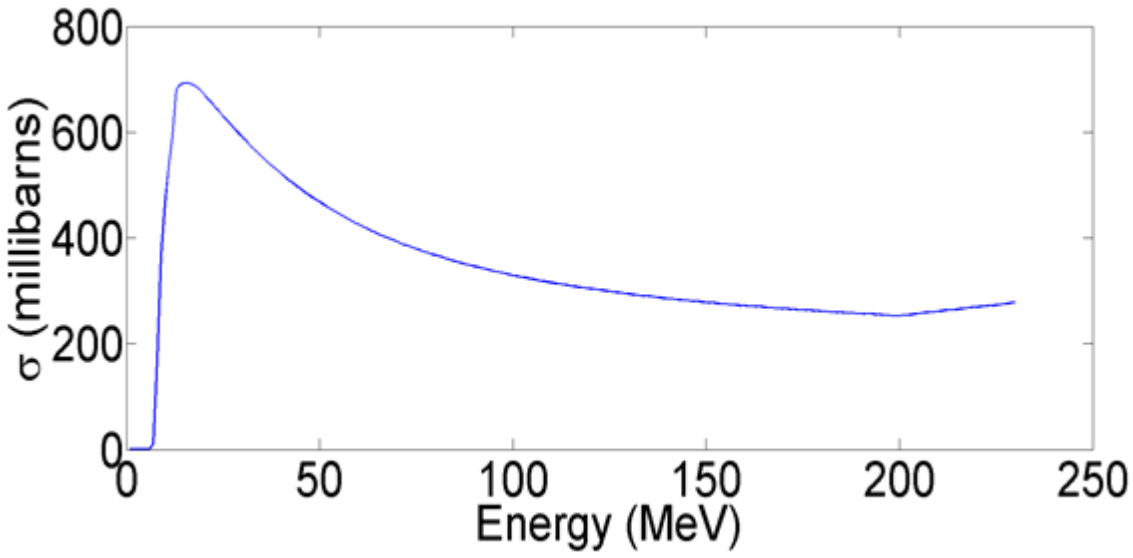

Figure 4.1: Total nuclear inelastic scattering cross sections. Protons incident on ^{16}O as a function of energy referenced from the TALYS1.8 nuclear data library. [109]

This is approximately seven orders of magnitude larger than the mean free path for elastic coulomb scattering at 26 MeV. Unlike coulomb scattering, hadronic interactions are single scattering and likely to occur once at most in a patient.

Fippel and Soukup[110] established that outside the primary beam, dose from secondary protons constitutes a low dose nuclear halo. It can be seen in Figure 4.2 that dose due to nuclear scattering begins to contribute to lateral dose distributions where it is approximately 1% of the dose from primary protons. Nuclear dose builds up with depth and is very broad so that for higher energies the nuclear halo accounts for up to 15% of total patient dose. [111, 112] Figure 4.3 shows that the majority of dose from secondary particles produced in hadronic scattering comes from secondary protons. The energy from secondary photons and neutrons is mostly transported out of the patient. While secondary alpha particles are common, their short range means that their energy is locally deposited. Secondary protons are therefore the largest contributor to the nuclear halo.[110]

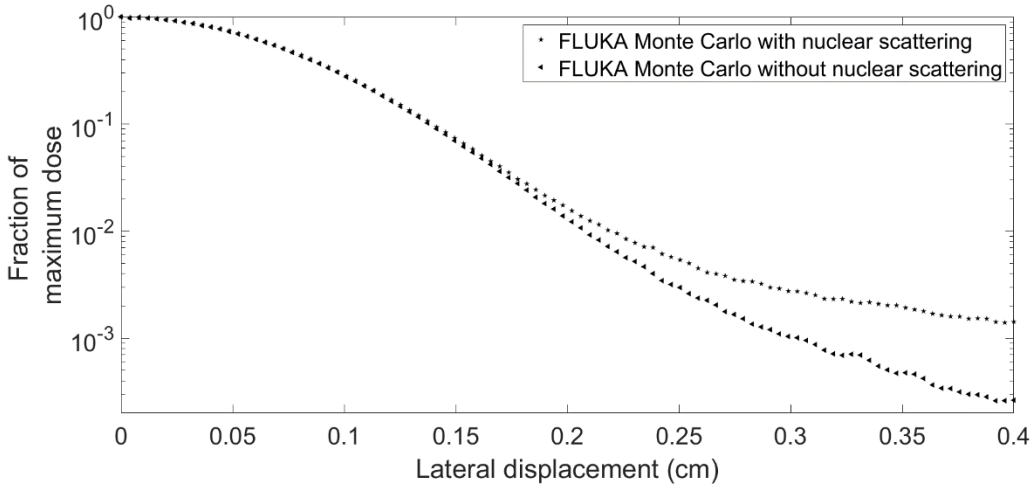

Figure 4.2. Effect of nuclear scattering on dose. 120 MeV proton beam in water. Where nuclear interactions were disabled, the THRESHOLd card for nuclear interactions in FLUKA was set to exceed the beam energy.

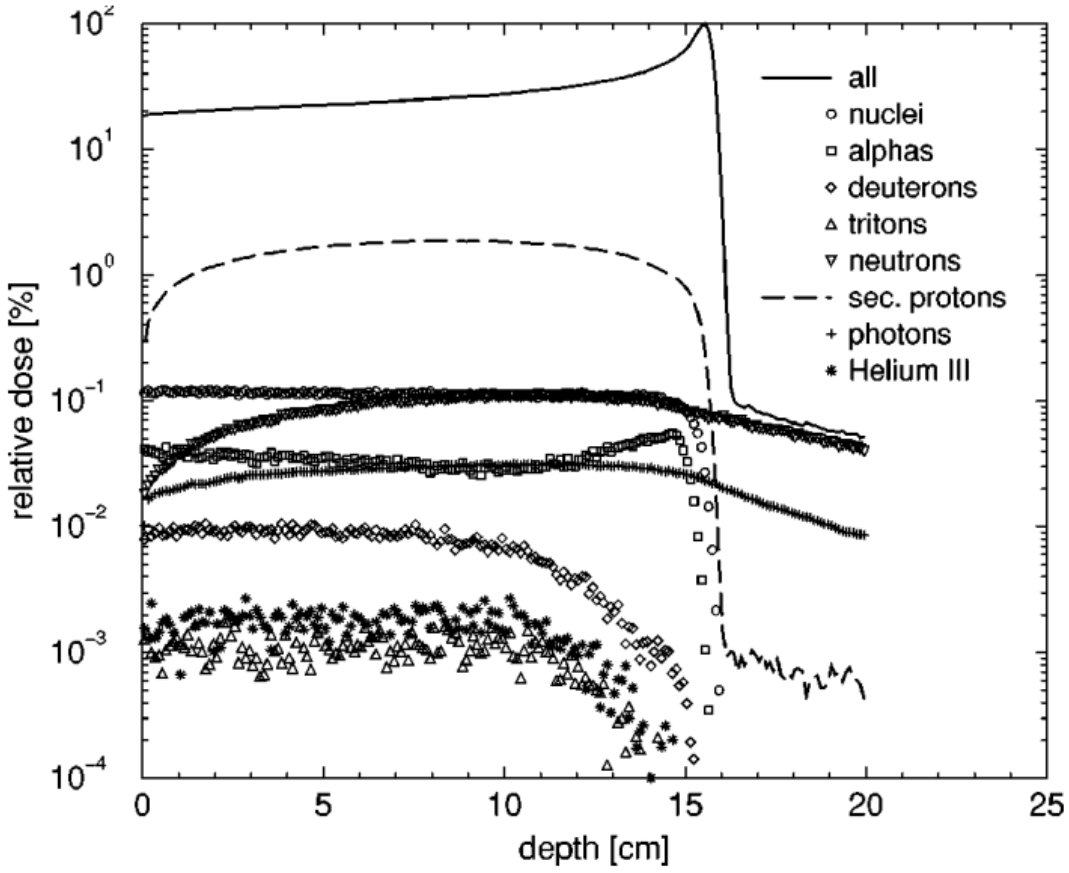

Figure 4.3. Dose contributions from different reaction channels. 150 MeV protons in water. (Taken from Fippel and Soukup[110]).

On the parameterization of the nuclear scattering

Kalbach[113-115] found that nuclear inelastic scattering cross sections are proportional to

$$\propto \exp\left(a \cos\theta\right) \qquad 4.2$$

Which becomes a Gaussian in the small angle approximation. Gaussian distributions have therefore had good results when used to parameterize the nuclear halo in treatment planning systems.

In commercially available treatment planning systems (TPS) such as Eclipse (Varian Medical Systems, Palo Alto, California)[116], the multiple coulomb scattering distribution is characterized by kernel parameters[117]. These are determined during commissioning by fitting a Gaussian to lateral dose distributions of the beam calculated by Monte Carlo codes such as FLUKA.

To incorporate the nuclear halo into dose calculation, an additional Gaussian function was added to the dose kernel by Soukup[111]. The double gaussian parameterization was further extended to three terms by Li[40] by fitting a Cauchy-Lorentz function. The current iteration of the Eclipse Treatment Planning System uses the two-Gaussian method.[116] Bellinzona[118] compares several parameterizations of Monte Carlo results, including a Gaussian-Rutherford function composed of a Gaussian core with a Rutherford-like function to characterize large angles. [119] Bellinzona accurately modeled the lateral profile down to 10^{-3} of central axis dose as compared to measurement using a Cauchy-Lorentz model that incorporates energy loss. Van den Huevel[120] parameterized the lateral profile in terms of "stable distributions," of which Gaussians are a type. All three methods approximated the nuclear halo well due to the similarity of their functional form to that of equation 4.2. [113-115]

A simple fit of Gaussians to the lateral nuclear halo generated in particle physics Monte Carlo codes such as FLUKA provides an adequate description for a single beam sub-spot, but without ad-hoc field size factors, the dose for different field sizes does not scale correctly.[121, 122 46, 123] They also suffer from a lack of robustness. A method is needed to accurately model the nuclear halo without resorting to curve fits to Monte Carlo. Introduced here is a simple model based on single scattering.

Hadronic interactions

The behavior of proton hadronic scattering with oxygen is characterized by the initial energy of the proton, and the timescale of the interaction. When the DeBroglie wavelength of the incident proton is comparable to the nucleon spacing the proton interactions with the nucleus are treated in terms of collisions with individual nucleons. In this case, secondary particles exit the nucleus on a very short time scale and are strongly forward peaked. Lower energy models treat the nucleus as a Fermi gas. Figure 4.4 shows that in the JENDL nuclear cross section tables, most secondary protons leave the nucleus with a large residual energy and a scattering angle of less than 60 degrees[124-127]. Scattering by this process is the source of the "low-dose halo" measured by Pedroni, Soukup and others.[111, 128-130]

After that, the nucleus begins to de-excite[131]. By this time, the proton momentum has been absorbed by the nucleus. After equilibrium, the density of states (from Fermi breakup) determines the probability of low-energy secondary proton escape. This distribution is isotropic and most protons have a short (less than 1mm) residual range. Although these protons are as likely to backscatter as to forward scatter, their short range means backscattering can be ignored and the residual energy of the particle can be considered to be locally deposited.

Calculating dose due to nuclear inelastic scattering.

To model proton single scattering, consider a beam normally incident on a water phantom. The phantom is divided into 1 mm depth intervals parallel to the surface as shown in Figure 4.5. The protons deposit energy in each 1 mm slice with energy given by

equations 1.12 to 1.16. This determines the initial energy of the nuclear processes at that depth.

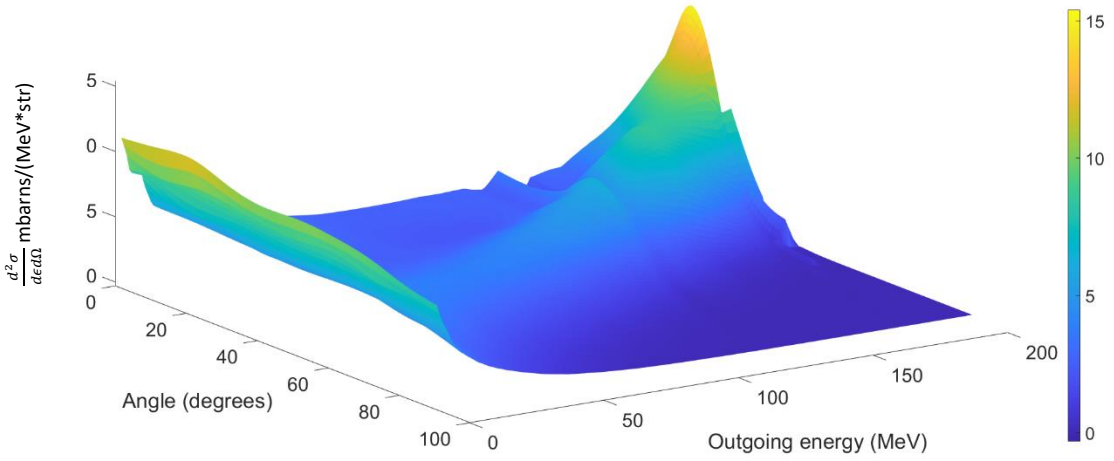

Figure 4.4. Inelastic double differential cross sections. $\frac{d^2\sigma}{d\Omega dE}$ for inelastic hadronic scattering of 230 MeV protons on oxygen, interpolated from JENDL-/HE-2007.

To calculate spatial distributions, it is necessary to determine the trajectory of the secondary proton. This was determined from the double differential cross section tables for inelastic scattering of JENDL-4.0/HE scattering on Oxygen-16 nuclei.[132] Elastic nuclear scattering was not included. The JENDL is a database of cross section tables from the Japan Nuclear Data Center, produced from many different codes. This is described in the JENDL-4.0/HE file. [124-127]. [111, 128-130]. [131]

In equation 4.3, the probability $P(\theta, \varepsilon)$, of a single scattering event for each angle θ and outgoing proton energy ϵ is determined from JENDL tables. The factor of 2π reflects azimuthal symmetry.

$$P(\theta,\varepsilon) = 2\pi n dz \int_{\varepsilon_1}^{\varepsilon_2} \int_{\theta_2}^{\theta_1} \frac{d^2\sigma}{d\varepsilon d\Omega}(\theta,\varepsilon) dcos\theta d\varepsilon \qquad 4.3$$

Where dz is the depth interval and $dcos\theta$ and $d\varepsilon$ refer to the angle step size and energy step size in the lookup table. $d\epsilon$ is bounded from below at 9 MeV, and secondary protons of less than 9 MeV have their energy locally deposited. For each primary proton energy, secondary proton cross sections from JENDL-4.0/HE were interpolated using a cubic spline into 200 secondary proton energies and angle steps of 1 degree.

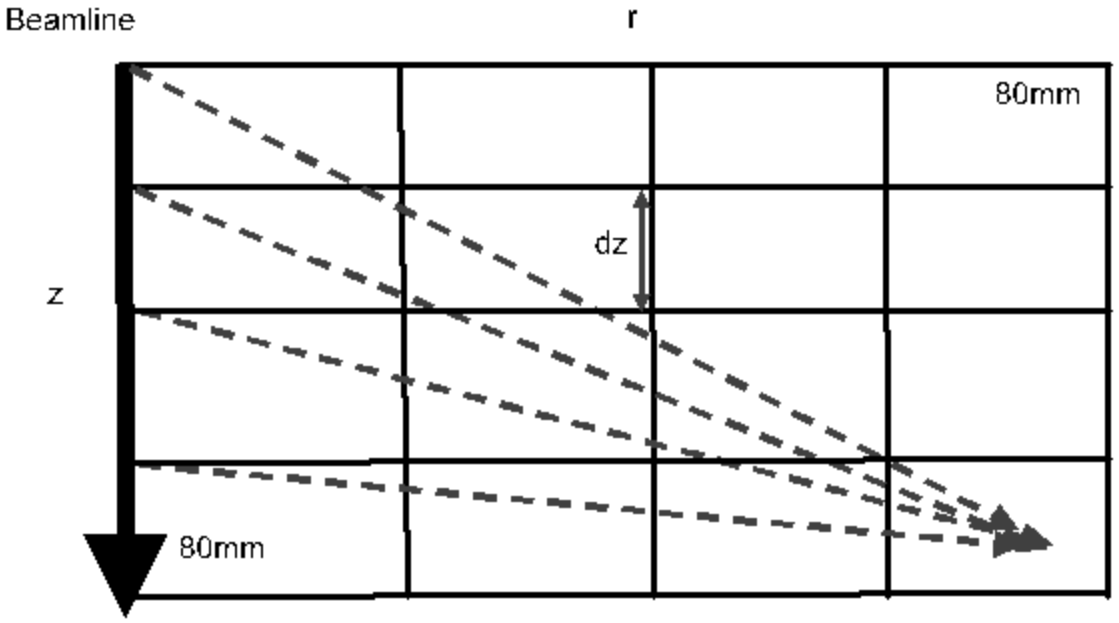

Figure 4.5. Secondary protons deposited energy along their trajectories. (dashed lines).

Each secondary proton trajectory in the lookup table deposits probability-weighted energy along its trajectory. The trajectory in terms of the angle θ is expressed in terms of the radius r and depth z with respect to the origin of the secondary proton trajectory, to give the path length L with element dz and dL.

$$dL = dz \sec\theta \qquad 4.4$$

Such that the probability-weighted energy deposited along a pathlength L is

$$dE = dL\left(\frac{\overline{\Delta}}{z}\right)P(\theta,\varepsilon)$$

At the r coordinate

$$r = z \tan \theta$$

The trajectories are binned by voxel in cylindrical coordinates, their energy is summed and then divided by the mass of the voxel to determine the dose. The cylindrical voxel mass is

$$V = \pi dz(r_2^2 - r_1^2)\rho$$

Where $\rho = 1\ g/cm^3$ for water. Secondary protons with a residual energy of less than 9 MeV are not advanced and have their energy deposited in the final voxel.

Lateral slices of the dose distribution are compared to relative dose profiles from FLUKA Monte Carlo in Figures 4.6 to 4.8. All profiles are in a water phantom with zero initial beam divergence at the phantom surface.

FLUKA Settings

FLUKA uses its own hadronic scattering models, benchmarked against in-house measurements and published cross sections.[37-39, 46, 47, 133] For figures 4.6 to 4.8, we disabled energy loss fluctuations using the IONFLUCT card, as well as transport of α-particles, photons, neutrons, deuterons and tritons. The production threshold for electrons was set to 10 KeV with the EMFCUT card. Dose (FLUKA code 228) was scored with the USRBIN card in cylindrical coordinates along the plotted region at the depth specified. A beam without angular or spatial divergence was set to impinge normal to the surface of a water phantom.

Figures 4.6 to 4.8 compare FLUKA lateral dose calculations with calculations from single inelastic nuclear scattering. We can see from figures 4.6 to 4.8 that the single scattering model predicts the same functional form as FLUKA, but differs from FLUKA

in terms of relative magnitude. It overpredicts the nuclear halo at shallow depths while underpredicting it at deeper depths.

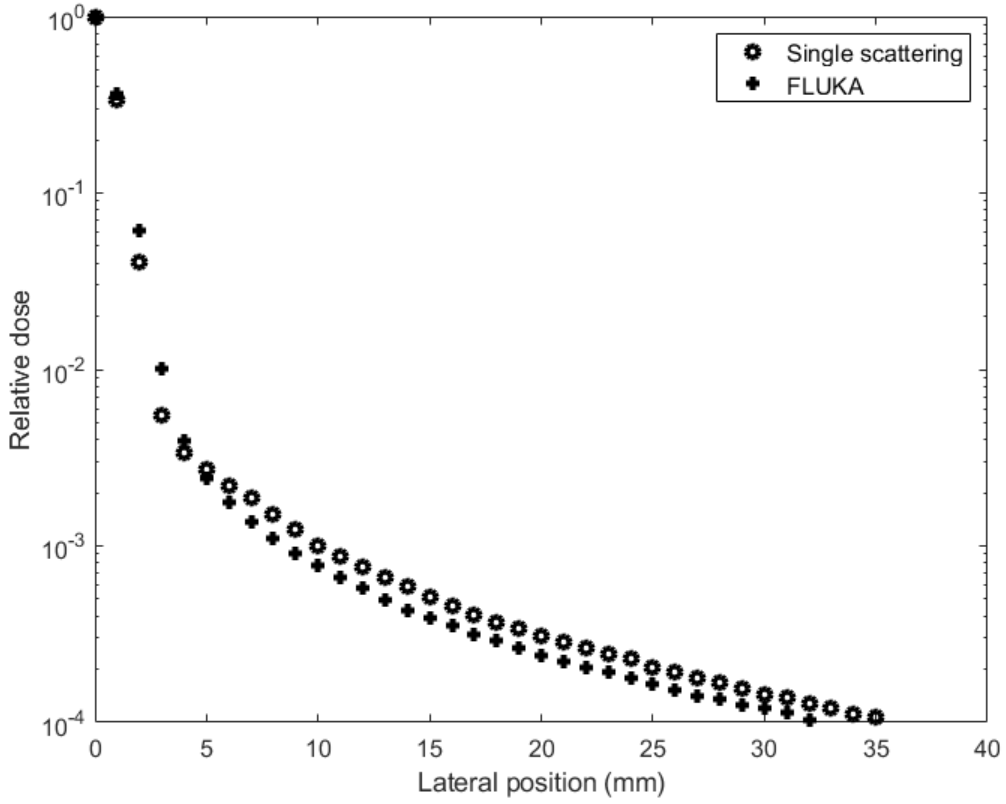

Figure 4.6a. Lateral dose for 228.8 MeV beam at 100mm depth. Normalized to the peak central axis dose (triangles).

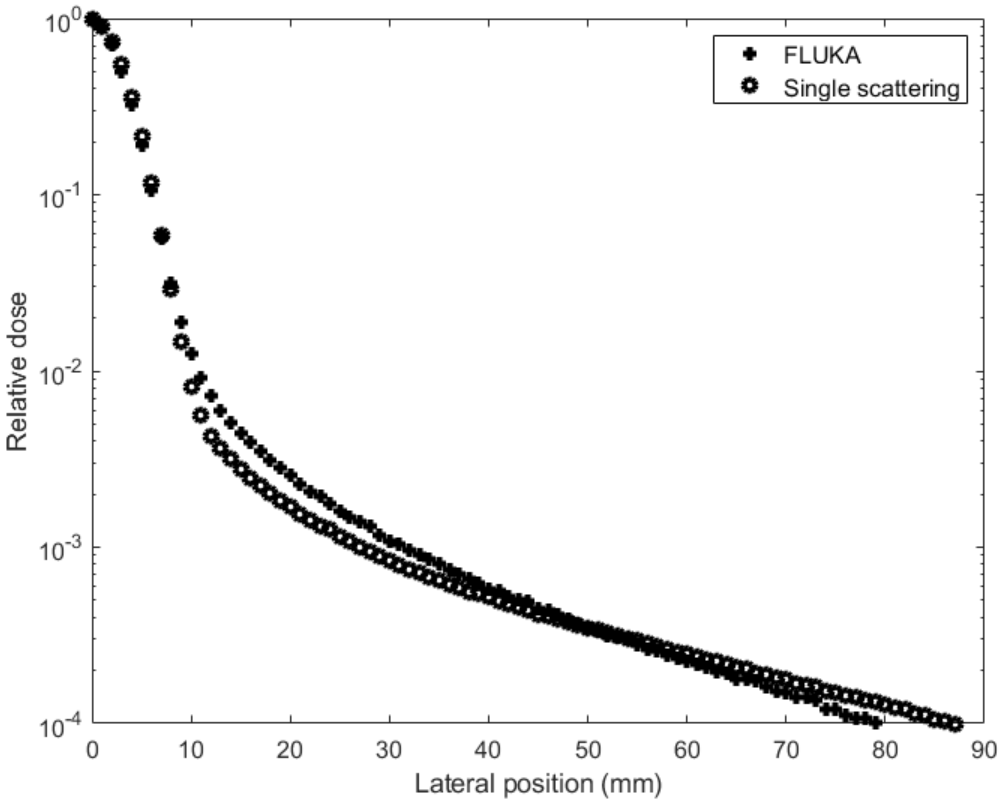

Figure 4.6b. Lateral dose for 228.8 MeV beam at 200mm depth. Normalized to the peak central axis dose.

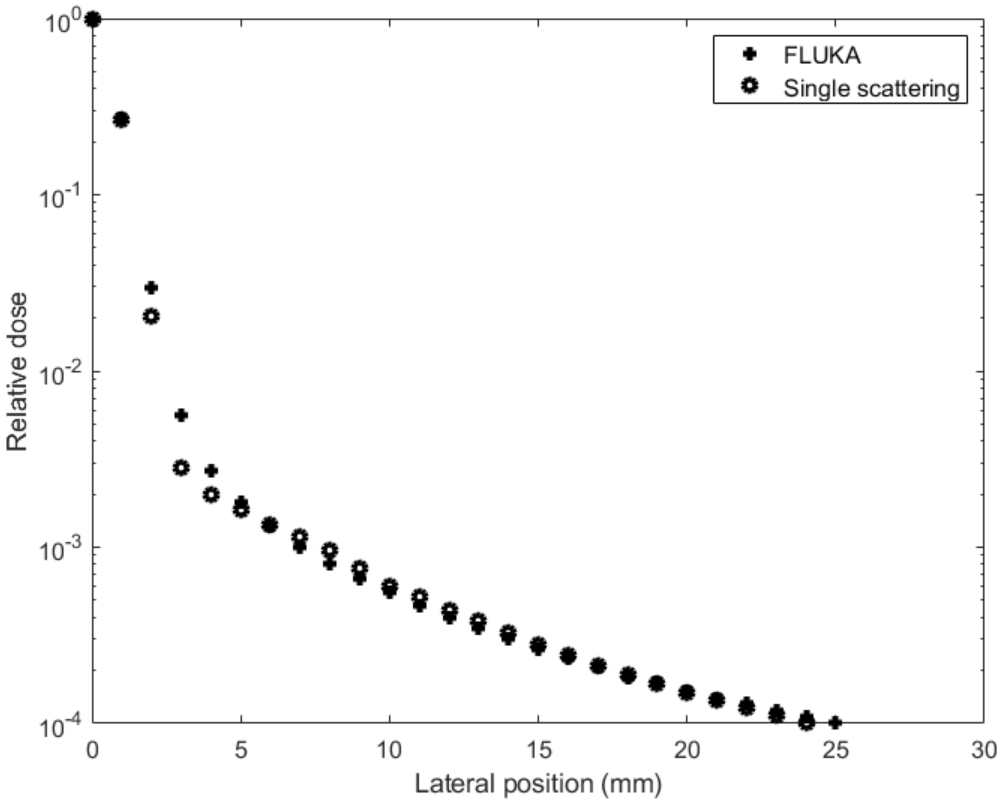

Figure 4.7a. Lateral dose for 189.0 MeV beam at 80mm depth. Normalized to the peak central axis dose.

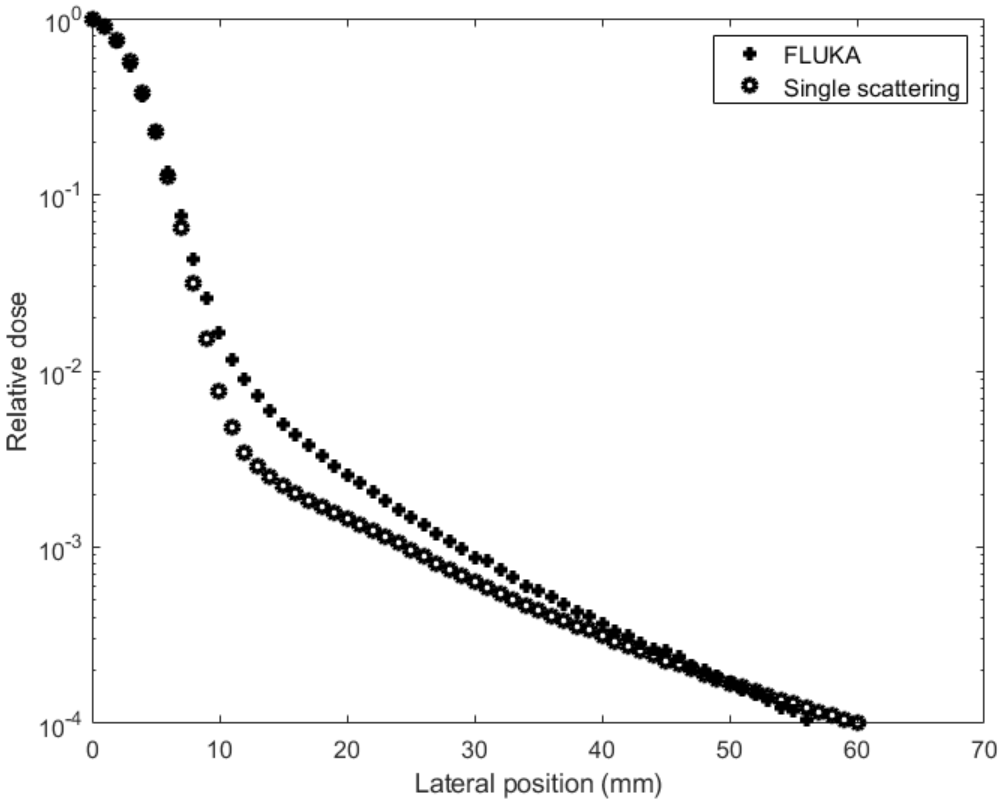

Figure 4.7b. Lateral dose for 189.0 MeV beam at 180mm depth. Normalized to the peak central axis dose.

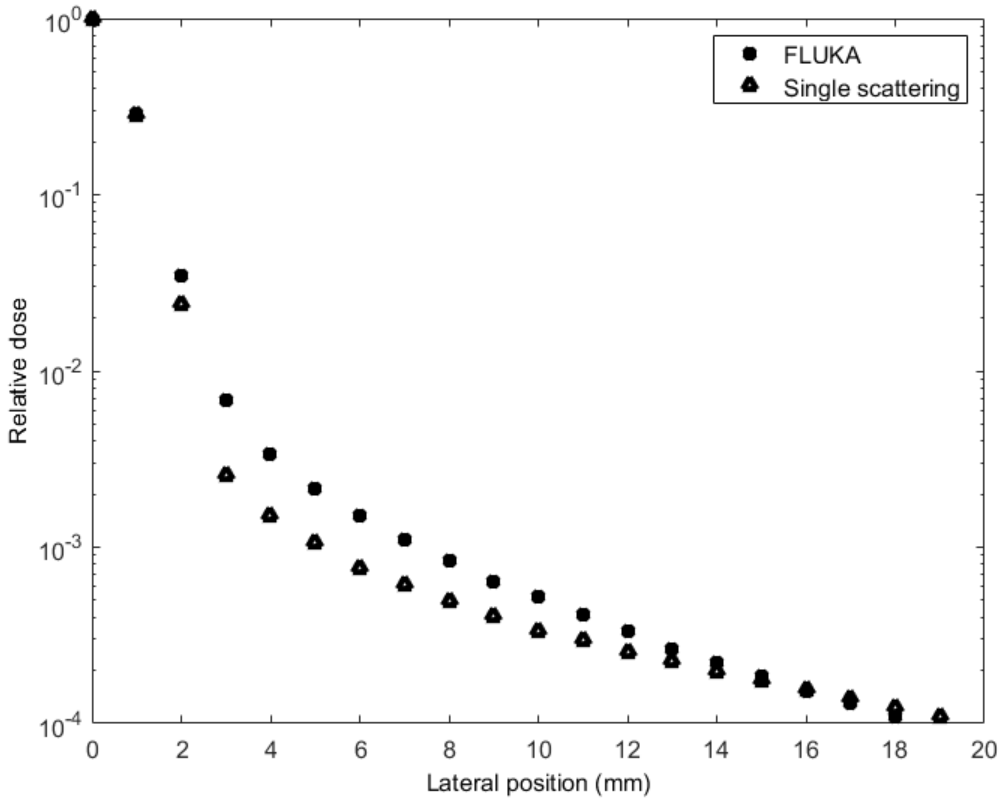

Figure 4.8. Lateral dose for 121.0 MeV beam at 60mm depth. Normalized to the peak central axis dose.

Conclusion

The functional form of the low-dose halo is described adequately by single inelastic nuclear scattering, although the relative magnitude is not consistent with FLUKA Monte Carlo. The magnitude of the lateral dose distributions is sensitive to the energy budget for secondary particle production and the cross sections must be normalized such that the total energy of the beam is conserved. Although energy lost to neutrons and gammas must be counted, dose due to neutrons and gammas make only a small contribution to the nuclear halo, and the description of the dose halo would likely not benefit from their inclusion.[110] For improved accuracy, nuclear elastic scattering

should be included. An accurate model can replace Monte Carlo fitting with calculations of specific trajectories that are relevant to the treatment plan. This would save calculation time and improve robustness for scaling to different field sizes.

CHAPTER 5

CONCLUDING REMARKS

Review

The elastic and inelastic transport equations describe the evolution of the phase space of a proton beam along a path length z in terms of the elastic single scattering cross section $\sigma(\chi)$ and the probability per unit length per unit energy $\omega(\epsilon)$. The probability angle distributions and the probability energy loss distributions in z can be determined from the "effective" number of scattering events per reciprocal multiple scattering angle η or reciprocal energy loss p. The probability distributions $f(\theta, z)$ and $f(\Delta, z)$ are the inverse transforms of the distributions in η or p. For large pathlengths with non-negligible energy loss, $\sigma(\chi)$ and $\omega(\epsilon)$ change with depth so that $f(\theta, z)$ and $f(\Delta, z)$ may be calculated by dividing the pathlength into depth intervals dz, and calculating $f(\theta, z)$ and $f(\Delta, z)$ as convolutions of the probability distributions at each dz.

By considering Molière's scattering law in terms of the transformation of the Legendre polynomials of Goudsmidt and Saunderson into Bessel functions and making the large angle substitutions of equations 2.55 to 2.59, the probability angle distribution follows the results of FLUKA Monte Carlo and converges on the complete single scattering differential cross section equation 2.11 as expected.

In the case of inelastic scattering, and where $\omega(\epsilon)$ varies appreciably across $f(\Delta, z)$, the probability energy loss distribution $f(\Delta, z)$ may be calculated from the number of inelastic scattering events corresponding to the energy loss Δ for a fixed z. Expressing the pathlength z in terms of the continuous slowing down approximation means that $f(\Delta, z)$ is dependent solely on the average energy loss $\overline{\Delta}$ rather than any

material specific parameter, with exception of the mean excitation energy I. The result follows FLUKA Monte Carlo to 80% of the total energy loss for an incident proton.

Cross sections for Molière theory

Although we have used Molière's implicit $\sigma(\chi)$ in terms of his screening parameter χ_a equation 2.18, any appropriate $\sigma(\chi)$ may be used. Depending on the material, there may be a more accurate potential than equation 2.3 in which the screening by atomic electrons is approximated by an exponential term. It is also possible that Molière's χ_a may not be the optimal value for materials with absolutely any atomic number. Nigam offers an alternative χ_a in terms of the second Born approximation, which we have not covered in this work.[69, 134]

An "Edgeworth Expansion" for Molière theory

The Edgeworth expansion equation 3.37 was used by Rotondi (1990) to describe the energy loss distributions in terms of the characteristic functions of the Fourier transform, which are the Hermite polynomials. Ferrari et, al (1997) has suggested that $f(\theta, z)$ may be calculated in terms of the projected angles, as in Snyder and Scott, using a method of cumulants, similar to their treatment of $f(\Delta, z)$ in "Moments Methods" in Chapter 3. It should also be possible to describe the Fourier transform of the projected angle distribution in terms of the Hermite polynomials in the form of the Edgeworth expansion. For the Molière scattering law in cylindrical coordinates, it can be seen from equation 2.31 that the moments are in terms of the Bessel functions $J_0(\eta\chi)$, $J_1(\eta\chi), J_2(\eta\chi)\ldots$which are the characteristic functions of the Bessel transform. These may compromise the moments of an "Edgeworth" expansion that describes the deviation of the angle distribution from a gaussian. Such a solution would offer speed

improvements over the exact solution to the Fourier or Bessel transform of the angular distribution. However, it would be limited to distributions that are not too narrow due to the finite number of moments.

Straggling for other particles

In principle, the inelastic scattering model equation 3.71 applies to any charged particle and a cross section of any ϵ dependence. Energy straggling of α particles should involve only different kinematics limits due to the different mass of the α particle from the proton. Electrons will have different ionization cross sections as well as a Bremsstrahlung cross section which may be convolved using Fourier transforms in the same manner as McLellan. The application of Fast Fourier Transform (FFT) algorithms to the problem of energy loss distributions is problematic due to the approximately nine order of magnitude difference between ϵ_{min} and ϵ_{max} that requires an impractically fine grid.[44] This is may be solved with non-uniform fast Fourier Transforms.

Nuclear improvements

Inelastic nuclear scattering should incorporate the Kalbach systematics directly, which are parameterized in terms of the coefficients of equation 4.2 in the ENDF[135] tables. Elastic scattering probabilities can be included in terms of Legendre coefficients in the same tables.[136] For implementation in a treatment planning system or clinical Monte Carlo code, only the clinically relevant trajectories should be tracked, with the remaining energy attributed to total patient dose.

Future treatment plans with direct Monte Carlo

While in the past hospitals have used approximation schemes and fitting of functions to Monte Carlo simulations to “commission” a treatment planning system,

continuous improvements in processing power allow for direct Monte Carlo calculation in the TPS. With the increased use of graphics processing units (GPUs) to do dose calculations in parallel, the future of treatment planning will involve custom Monte Carlo codes that are conditioned to the clinical energy regime. Within such a scheme, there remain possible improvements to Physics models that describe the proton trajectories and the associated dose distribution. Outside of clinical physics, such models may be applied to aerospace or microscopy.

REFERENCES

1. F. M. Khan, *The Physics of Radiation Therapy*, Third Edition ed. (Lippincott Williams & Wilkins, Philadelphia, PA., 2003).

2. G. M. Mackee, JAMA: The Journal of the American Medical Association **133** (2), 144-144 (1947).

3. D. E. Grider, A. Wright and P. K. Ausburn, Journal of Physics D: Applied Physics **19** (12), 2281 (1986).

4. R. Wideröe, Archiv für Elektrotechnik **21** (4), 387-406 (1928).

5. S. Webb, 478 (2005).

6. O. Klein and Y. Nishina, Zeitschrift für Physik **52** (11), 853-868 (1929).

7. O. Klein and Y. Nishina, Nature **122** (3072), 398-399 (1928).

8. J. R. C. H.E Johns, *The physics of radiology*, 4th ed. (Charles C. Thomas, Springfield, Ill., U.S.A, 1983).

9. G. Solaiappan, G. Singaravelu, A. Prakasarao, B. Rabbani and S. S. Supe, Reports of Practical Oncology & Radiotherapy **14** (1), 18-31 (2009).

10. M. J. Berger, Coursey, J.S., Zucker, M.A., Chang, J., (Gaithersburg, MD., 2005).

11. G. W. Grodstein, National Bureau of Standards Circular **583** (1957).

12. E. B. Saloman and J. H. Hubbell, 1986.

13. E. B. Saloman, J. H. Hubbell and J. H. Scofield, Atomic Data and Nuclear Data Tables **38** (1), 1-196 (1988).

14. N. D. Tapley, *Clinical applications of the electron beam*. (Krieger Publishing Company, 1982).

15. H. Bethe and W. Heitler, Proc. Roy. Soc. Lond. A **146**, 83-112 (1934).

16. J. D. Jackson, *Classical electrodynamics*. (Third edition. New York : Wiley, [1999] ©1999, 1999).

17. N. G. Huilgol, Journal of cancer research and therapeutics **5** (4).

18. E. Rutherford, The London, Edinburgh, and Dublin Philosophical Magazine and Journal of Science **37** (222), 581-587 (1919).

19. E. O. Lawrence, (Google Patents, 1934).

20. F. E. Close, Marten, M., Sutton, C., & Close, F. E., *The particle odyssey: A journey to the heart of the matter*. (Oxford University Press., 2002).

21. R. R. Wilson, Radiology **47** (5), 487-491 (1946).

22. M. E. Mcmillan, (Google Patents, 1952).

23. J. Gonzalez, Arizona State University, 2017.

24. in *History of Proton Beam Therapy* (UC Davis Cancer Center, 2006), Vol. 9.

25. E. A. Knapp, IEEE Transactions on Nuclear Science **16** (3), 329-337 (1969).

26. S. R. Grant, D. R. Grosshans, S. D. Bilton, J. A. Garcia, M. Amin, M. S. Chambers, S. L. McGovern, M. F. McAleer, W. H. Morrison, W. W. Huh, M. E. Kupferman and A. Mahajan, Radiotherapy and Oncology **116** (2), 309-315 (2015).

27. Q.-N. Nguyen, N. B. Ly, R. Komaki, L. B. Levy, D. R. Gomez, J. Y. Chang, P. K. Allen, R. J. Mehran, C. Lu, M. Gillin, Z. Liao and J. D. Cox, Radiotherapy and Oncology **115** (3), 367-372 (2015).

28. S. P. Register, X. Zhang, R. Mohan and J. Y. Chang, in *International journal of radiation oncology, biology, physics* (2011), Vol. 80, pp. 1015-1022.

29. I. R. Vogelius, D. C. Westerly, M. C. Aznar, G. M. Cannon, S. S. Korreman, T. R. Mackie, M. P. Mehta and S. M. Bentzen, Acta Oncologica **50** (6), 772-776 (2011).

30. E. Dinges, N. Felderman, S. McGuire, B. Gross, S. Bhatia, S. Mott, J. Buatti and D. Wang, Radiotherapy and Oncology **115** (3), 373-378 (2015).

31. R. Zhang, R. M. Howell, P. J. Taddei, A. Giebeler, A. Mahajan and W. D. Newhauser, Radiotherapy and Oncology **113** (1), 84-88 (2014).

32. B. C. Baumann, N. Mitra, J. G. Harton, Y. Xiao, A. P. Wojcieszynski, P. E. Gabriel, H. Zhong, H. Geng, A. Doucette, J. Wei, P. J. O'Dwyer, J. E. Bekelman and J. M. Metz, JAMA oncology **6** (2), 237-246 (2020).

33. N. H. Barth, International journal of radiation oncology, biology, physics **18**, 425-431 (1990).

34. D. Wang, Medical devices (Auckland, N.Z.) **8**, 439 (2015).

35. R. Zhang and W. D. Newhauser, Physics in medicine and biology **54** (6), 1383-1395 (2009).

36. M. Mahesh, Medical Physics **40** (7), 077301 (2013).

37. G. Battistoni, J. Bauer, T. T. Boehlen, F. Cerutti, M. P. W. Chin, R. Dos Santos Augusto, A. Ferrari, P. G. Ortega, W. Kozłowska, G. Magro, A. Mairani, K. Parodi, P. R. Sala, P. Schoofs, T. Tessonnier and V. Vlachoudis, Front Oncol **6**, 116-116 (2016).

38. T. T. Böhlen, F. Cerutti, M. P. W. Chin, A. Fassò, A. Ferrari, P. G. Ortega, A. Mairani, P. R. Sala, G. Smirnov and V. Vlachoudis, Nuclear Data Sheets **120**, 211-214 (2014).

39. G. Battistoni, F. Cerutti, A. Fassò, A. Ferrari, S. Muraro, J. Ranft, S. Roesler, P. R. Sala, M. Albrow and R. Raja, AIP Conference Proceedings **896** (1), 31-49 (2007).

40. Y. Li, R. X. Zhu, N. Sahoo, A. Anand and X. Zhang, in *Physics in Medicine and Biology* (2012), Vol. 57, pp. 983-997.

41. P. Rez, (Mayo Clinic, 2016).

42. B. Gottschalk, Med Phys **37** (1), 352-367 (2010).

43. M. Inokuti, Reviews of Modern Physics **43** (3), 297-347 (1971).

44. J. McLellan, S. Sawchuk, J. J. Battista, G. A. Sandison and L. S. Papiez, Medical Physics **21** (3), 367-378 (1994).

45. A. Fasso, A. Ferrari, J. Ranft and P. R. Sala, 1997.

46. A. Ferrari, P. Sala, A. Fasso and J. Ranft, CERN Yellow report **2005-10** (2005).

47. A. Ferrari, P. R. Sala, R. Guaraldi and F. Padoani, Nuclear Instruments and Methods in Physics Research Section B: Beam Interactions with Materials and Atoms **71** (4), 412-426 (1992).

48. R. D. Evans, *The atomic nucleus*. (McGraw-Hill, New York, 1955).

49. H. Øverås, *On small-angle multiple scattering in confined bodies*. (CERN, Geneva, 1960).

50. U. Schneider, J. Besserer and P. Pemler, Zeitschrift fur medizinische Physik **11 2**, 110-118 (2001).

51. B. Rossi and K. Greisen, Reviews of Modern Physics **13** (4), 240-309 (1941).

52. E. B. Podgorsak and W. R. Hendee, Medical Physics **33**, 249 (2006).

53. C. Kittel, *Introduction to Solid State Physics*, 8th ed. (John Wiley & Sons, Inc., 111 River St. Hoboken N.J., 2005).

54. H. A. Bethe, M. E. Rose and L. P. Smith, Proceedings of the American Philosophical Society **78** (4), 573-585 (1938).

55. H. S. Snyder and W. T. Scott, Physical Review **76** (2), 220-225 (1949).

56. L. Eyges, Physical Review **74** (10), 1534-1535 (1948).

57. K. R. Russell, E. Grusell and A. Montelius, Physics in Medicine and Biology **40** (6), 1031 (1995).

58. K. R. Hogstrom, M. D. Mills and P. R. Almond, Physics in Medicine and Biology **26** (3), 445 (1981).

59. H. A. Bethe, Physical Review **89** (6), 1256-1266 (1953).

60. E. J. Williams and J. Chadwick, Proceedings of the Royal Society of London. Series A. Mathematical and Physical Sciences **169** (939), 531-572 (1939).

61. G. S. Ibbott, Medical Physics **12** (6), 813-813 (1985).

62. S. Goudsmit and J. Saunderson, Physical Review **57**, 552-552 (1940).

63. K. Busch, C. M. Soukoulis and E. N. Economou, in *Physical Review B* (1994), Vol. 50, pp. 93-98.

64. P. Rez, T. Larsen and M. Elbaum, Journal of Structural Biology **196** (3), 466-478 (2016).

65. N. Zettili, *Quantum Mechanics: Concepts and Applications*. (Wiley, 2009).

66. N. F. Mott, Mathematical Proceedings of the Cambridge Philosophical Society **27** (4), 553-560 (2008).

67. M. Born, Zeitschrift für Physik **38** (11), 803-827 (1926).

68. J. J. Sakurai and J. Napolitano, *Modern Quantum Mechanics*, 2 ed. (Cambridge University Press, Cambridge, 2017).

69. J. Janni, 451 (1966).

70. H. Yukawa, Progress of Theoretical Physics Supplement **1**, 1-10 (1955).

71. N. W. Ashcroft, A. N. W, N. D. Mermin, N. D. Mermin and B. C. P. Company, *Solid State Physics*. (Holt, Rinehart and Winston, 1976).

72. G. Moliere, Zeitschrift für Naturforschung A **2** (3), 133-145 (1947).

73. G. Moliere, Zeitschrift für Naturforschung A **3** (2), 78-97 (1948).

74. L. A. Kulchitsky and G. D. Latyshev, Physical Review **61**, 254-265 (1942).

75. A. O. Hanson, L. H. Lanzl, E. M. Lyman and M. B. Scott, Physical Review **84** (4), 634-637 (1951).

76. H. W. Lewis, Physical Review **78** (5), 526-529 (1950).

77. V. L. Highland, Nuclear Instruments and Methods **129** (2), 497-499 (1975).

78. B. Gottschalk, a. M. Koehler, R. J. Schneider, J. M. Sisterson and M. S. Wagner, Nuclear Instruments and Methods in Physics Research Section B: Beam Interactions with Materials and Atoms **74**, 467-490 (1993).

79. N. Kanematsu, Nuclear Instruments and Methods in Physics Research Section B: Beam Interactions with Materials and Atoms **266** (23), 5056-5062 (2008).

80. B. Gottschalk, (2012).

81. W. Liu, (2014).

82. A. M. Kellerer, in *The Dosimetry of Ionizing Radiation*, edited by B. E. BjÄRngard and F. H. Attix (Academic Press, 1985), pp. 77-162.

83. H. H. Z. Rossi, M., *Microdosimetry and Its Applications*, 1 ed. (Springer-Verlag Berlin Heidelberg, 1996).

84. M. S. Livingston and H. A. Bethe, Reviews of Modern Physics **9** (3), 245-390 (1937).

85. H. A. Bethe, Reviews of Modern Physics **9** (2), 69-244 (1937).

86. L. Landau, J. Phys. USSR **8**, 201 (1944).

87. P. V. Vavilov, Sov. Phys. JETP **5**, 749-751 (1957).

88. W. Borsch-Supan, JOURNAL OF RESEARCH of the National Bureau of Standards-B. Mathematics and Mathematical Physics **65B** (4) (1961).

89. M. Inokuti and S. T. Manson, United States, 1982 (unpublished).

90. A. Rotondi and P. Montagna, Nuclear Instruments and Methods in Physics Research Section B: Beam Interactions with Materials and Atoms **47** (3), 215-223 (1990).

91. M. J. Berger, M. Inokuti, H. H. Anderson, H. Bichsel, J. A. Dennis, D. Powers, S. M. Seltzer and J. E. Turner, Reports of the International Commission on Radiation Units and Measurements **os-19** (2), 7-14 (1984).

92. R. M. Sternheimer, M. J. Berger and S. M. Seltzer, Atomic Data and Nuclear Data Tables **30** (2), 261-271 (1984).

93. M. Dingfelder, D. Hantke, M. Inokuti and H. G. Paretzke, Radiation Physics and Chemistry **53** (1), 1-18 (1998).

94. M. Dingfelder, M. Inokuti and H. G. Paretzke, Radiation Physics and Chemistry **59** (3), 255-275 (2000).

95. H. Bichsel and R. P. Saxon, Physical Review A **11** (4), 1286-1296 (1975).

96. H. Bichsel, Physical Review A **46** (9), 5761-5773 (1992).

97. P. Shulek, B. M. Golovin and L. A. Kulyukina, (2001).

98. H. Bichsel, Reviews of Modern Physics **60** (3), 663 (1988).

99. G. T. Huetter, R. Madey and S. M. Yushak, Physical Review A **6** (1), 250-255 (1972).

100. R. M. Sternheimer, Physical Review **88** (4), 851-859 (1952).

101. R. M. Sternheimer, Physical Review **103** (3), 511-515 (1956).

102. K. R. Symon, 1948.

103. C. Tschalär, Nuclear Instruments and Methods **61** (2), 141-156 (1968).

104. C. Tschalär and H. D. Maccabee, Physical Review B **1**, 2863-2869 (1970).

105. H. W. Lewis, Physical Review **85** (1), 20-24 (1952).

106. J. R. Herring and E. Merzbacher, **Vol: 3, No. 2** (1957).

107. E. J. Williams and E. Rutherford, Proceedings of the Royal Society of London. Series A, Containing Papers of a Mathematical and Physical Character **125** (798), 420-445 (1929).

108. S. R. Grant, D. R. Grosshans, S. D. Bilton and J. A. Garcia, Radiotherapy and oncology **116** (2), 309-315.

109. S. H. A.J. Koning, M.C. Duijvestijn, presented at the International Conference on Nuclear Data for Science and Technology - ND2007, Nice, France, April 22-27, 2007 (unpublished).

110. M. Fippel and M. Soukup, Medical Physics **31** (8), 2263 (2004).

111. M. Soukup, M. Fippel and M. Alber, Physics in medicine and biology **50**, 5089-5104 (2005).

112. Y. Dzierma, K. Mikulla, P. Richter, K. Bell, P. Melchior, F. Nuesken and C. Rübe, Radiation Oncology **13** (1), 168 (2018).

113. C. Kalbach, Physical Review C **37** (6), 2350-2370 (1988).

114. C. Kalbach, Physical Review C **25** (6), 3197-3200 (1982).

115. C. Kalbach and F. M. Mann, Physical Review C **23** (1), 112-123 (1981).

116. N. Sahoo, F. Poenisch, X. Zhang, Y. Li, M. Lii, H. Li, A. S. Gautam, R. Wu, M. Gillin and X. R. Zhu, Medical dosimetry : official journal of the American Association of Medical Dosimetrists **43** (2), 184-194 (2018).

117. Varian, (Varian Medical Systems, Palo

Alto, CA, 2015).

118. V. E. Bellinzona, M. Ciocca, A. Embriaco, A. Fontana, A. Mairani, M. Mori and K. Parodi, Physica medica : PM : an international journal devoted to the applications of physics to medicine and biology : official journal of the Italian Association of Biomedical Physics (AIFB) **31** (5), 484-492 (2015).

119. E. V. Bellinzona, M. Ciocca, A. Embriaco, A. Ferrari, A. Fontana, A. Mairani, K. Parodi, A. Rotondi, P. Sala and T. Tessonnier, Physics in Medicine and Biology **61** (4), N102-117 (2016).

120. F. Van den Heuvel, B. George, N. Schreuder and F. Fiorini, Medical physics **45** (5), 2278-2288 (2018).

121. Z. Zhao, C. Toramatsu, R. Slopsema and Z. Li, Medical Physics **38** (6Part16), 3571-3571 (2011).

122. J. Shen, J. M. Lentz, Y. Hu, W. Liu, D. H. Morales, J. B. Stoker and M. Bues, Radiat Oncol **12** (1), 52-52 (2017).

123. F. C. T.T. Böhlen, M.P.W. Chin, A. Fassò, A. Ferrari, P.G. Ortega, A. Mairani, P.R. Sala, G. Smirnov and V. Vlachoudis, Nuclear Data Sheets **120**, 211-214 (2014).
124. J. Cugnon and P. Henrotte, The European Physical Journal A **16** (3), 393-407 (2003).

125. D. H. Wright and M. H. Kelsey, Nuclear Instruments and Methods in Physics Research Section A: Accelerators, Spectrometers, Detectors and Associated Equipment **804**, 175-188 (2015).

126. M. P. Chin and N. M. Spyrou, Appl Radiat Isot **67** (3), 406-414 (2009).

127. M. B. Chadwick, P. G. Young, S. Chiba, S. C. Frankle, G. M. Hale, H. G. Hughes, A. J. Koning, R. C. Little, R. E. MacFarlane, R. E. Prael and L. S. Waters, Nuclear Science and Engineering **131** (3), 293-328 (1999).

128. B. Gottschalk, E. W. Cascio, J. Daartz and M. S. Wagner, Phys Med Biol **60** (14), 5627-5654 (2015).

129. E. Pedroni, S. Scheib, T. Böhringer, A. Coray, M. Grossmann, S. Lin and A. Lomax, Physics in Medicine and Biology **50**, 541-561 (2005).

130. D. C. Hall, A. Makarova, H. Paganetti and B. Gottschalk, Physics in Medicine and Biology **61** (1), N1-N10 (2015).

131. A. J. Koning, Akkermans, J.M., *Pre-equilibrium nuclear reactions: An introduction to classical and quantum-mechanical*

models. (World Scientific, Singapore, 1999).

132. K. Shibata, O. Iwamoto, T. Nakagawa, N. Iwamoto, A. Ichihara, S. Kunieda, S. Chiba, K. Furutaka, N. Otuka, T. Ohsawa, T. Murata, H. Matsunobu, A. Zukeran, S. Kamada and J.-i. Katakura, Journal of Nuclear Science and Technology **48** (1), 1-30 (2011).

133. C. Robert, G. Dedes, G. Battistoni, T. T. Bohlen, I. Buvat, F. Cerutti, M. P. Chin, A. Ferrari, P. Gueth, C. Kurz, L. Lestand, A. Mairani, G. Montarou, R. Nicolini, P. G. Ortega, K. Parodi, Y. Prezado, P. R. Sala, D. Sarrut and E. Testa, Phys Med Biol **58** (9), 2879-2899 (2013).

134. B. P. Nigam, M. K. Sundaresan and T.-Y. Wu, Physical Review **115** (3), 491-502 (1959).

135. D. A. Brown, M. B. Chadwick, R. Capote, A. C. Kahler, A. Trkov, M. W. Herman, A. A. Sonzogni, Y. Danon, A. D. Carlson, M. Dunn, D. L. Smith, G. M. Hale, G. Arbanas, R. Arcilla, C. R. Bates, B. Beck, B. Becker, F. Brown, R. J. Casperson, J. Conlin, D. E. Cullen, M. A. Descalle, R. Firestone, T. Gaines, K. H. Guber, A. I. Hawari, J. Holmes, T. D. Johnson, T. Kawano, B. C. Kiedrowski, A. J. Koning, S. Kopecky, L. Leal, J. P. Lestone, C. Lubitz, J. I. Márquez Damián, C. M. Mattoon, E. A. McCutchan, S. Mughabghab, P. Navratil, D. Neudecker, G. P. A. Nobre, G. Noguere, M. Paris, M. T. Pigni, A. J. Plompen, B. Pritychenko, V. G. Pronyaev, D. Roubtsov, D. Rochman, P. Romano, P. Schillebeeckx, S. Simakov, M. Sin, I. Sirakov, B. Sleaford, V. Sobes, E. S. Soukhovitskii, I. Stetcu, P. Talou, I. Thompson, S. van der Marck, L. Welser-Sherrill, D. Wiarda, M. White, J. L. Wormald, R. Q. Wright, M. Zerkle, G. Žerovnik and Y. Zhu, Nuclear Data Sheets **148**, 1-142 (2018).

136. M. Herman, (United States, 2009).